

A highly efficient reduced order model considering aging effects for lithium ion polymer
batteries

by

Yinyin Zhao

A dissertation submitted to the Graduate Faculty of
Auburn University
in partial fulfillment of the
requirements for the Degree of
Doctor of Philosophy

Auburn, Alabama
December 10, 2016

Keywords: Lithium ion polymer battery, reduced order model, aging effects, side reactions,
SEI

Copyright 2016 by Yinyin Zhao

Approved by

Song-Yul Choe, Chair, Professor of Mechanical Engineering
Jeffrey Fergus, Professor of Materials Engineering
Roy Knight, Professor of Mechanical Engineering
Junshan Lin, Assistant Professor of Mathematics

Abstract

Mechanisms for ion transport, diffusion, and intercalation/de-intercalation processes in batteries during charging and discharging are described by governing equations that consist of partial differential equations and nonlinear functions in an electrochemical model. Solving these equations numerically is computationally intensive, particularly when the number of cells connected in series and parallel for high power or energy increases, whereas tolerance of errors should be kept under specified limits. Reduction of the computational time is required not only for enabling simulation of the behavior of packs but also for the development of a model capable of running in real time environments, so that new advanced estimation methods for state of charge (SOC) and state of health (SOH) can be developed. In order to represent the physical behaviors of a battery and optimize the computational time, advanced model order reduction techniques have been applied to reduce the model complexity for individual variables. Padé approximation, Residue Grouping and Proper Orthogonal Decomposition (POD) are introduced to simplify the calculation of ion concentration in electrode particles, ion concentration in electrolyte and potentials in electrode and electrolyte, respectively. Meanwhile, the Butler-Volmer equation is linearized and the equilibrium potential curves are fitted to different order polynomials.

Additionally, the aging effects are considered in the model for prediction of the battery end of life. Our investigation on aging mechanisms of the lithium ion batteries has revealed that side reaction is the main cause among others for capacity and power fade of the battery. The production of the side reaction forms thin unsolvable layers that adhere to the surface of the graphite particles and grow as cycled, which is called solid electrolyte interphase (SEI). The

growth of the SEI leads to loss of the lithium ions, loss of the electrolytes and loss of the active volume fraction. These effects are described using the Butler-Volmer kinetics and aging parameters. Particularly, electrolyte solvent diffusion described by Fick's law is integrated into the aging model, which results in quantifying the electrolyte solvent concentration in SEI. The exchange current density of the side reaction is formulated as a function of electrolyte solvent and lithium ion concentration, which justifies the reaction rate in the aspect of reactants. In addition, the temperature dependency of the model parameters is also considered by adopting the energy equations. Finally, the aging model is incorporated into the ROM.

Performances of the ROM are compared with the experimental data collected from a high power pouch type lithium ion polymer battery with $\text{Li}(\text{MnNiCo})\text{O}_2/\text{Graphite}$ chemistry.

Acknowledgements

I would like to express my gratitude to my advisor, Dr. Song-yul Choe, for generously offering me this research opportunity. His guidance, support, and encouragement assisted me to the fulfillment of my study. I would also like to acknowledge my committee members, Dr. Jeffrey Fergus, Dr. Roy Knight and Dr. Junshan Lin, for providing interdisciplinary insight.

Special thanks to my lab colleagues for their assistance in my research work, especially Rujian Fu, Xueyan Li and Meng Xiao.

Finally, I would like to convey my deep appreciation to my parents, Gang Zhang and Jiyu Zhao, for their unselfish support of my academic endeavor. Special thanks to my dear husband, Siwei Wang, for his love, support, and encouragement throughout my graduate school experience.

Table of Contents

Abstract	ii
Acknowledgements	iv
List of Tables	ix
List of Figures	x
List of Symbols	xiv
List of Abbreviations	xviii
Chapter 1 Introduction.....	1
1.1 Background.....	1
1.2 Working principle and battery chemistry	2
1.3 Motivation and objectives.....	6
1.4 Dissertation structure	7
Chapter 2 Reduced order model	9
2.1 Review of model order reduction techniques	9
2.2 Setup of the full order electrochemical model [13]	14
2.2.1 Ion transport and charge conservation	15
2.2.2 Butler-Volmer equation and equilibrium potentials	17

2.2.3	Energy equation	19
2.3	Development of a reduced order model.....	20
2.3.1	Ion concentration in electrode particles	20
2.3.2	Ion concentration in electrolyte	23
2.3.3	Potentials in electrodes and electrolyte.....	25
2.3.4	Electrochemical kinetics	27
2.4	Analysis of the ROM performances	28
2.4.1	Order reduction of ion concentration in electrode particles.....	28
2.4.2	Order reduction of ion concentration in electrolyte	33
2.4.3	Order reduction of potentials in electrode and electrolyte.....	34
2.4.4	ROM for a single cell.....	37
2.4.5	Effects of sampling time	38
2.5	Experimental validation of the ROM.....	39
2.5.1	Discharging and charging	40
2.5.2	Multiple cycles and EV driving cycles	45
2.5.3	Comparison with the previous ROM	47
2.6	Summary of the ROM.....	49
Chapter 3	Experimental investigation and parameter identification	51

3.1	Experimental setup.....	51
3.2	Analysis of aging cycling data.....	53
3.3	Analysis of EIS data.....	58
3.4	Determination of temperature dependent parameters.....	64
Chapter 4	Aging model.....	69
4.1	Literature review.....	69
4.1.1	Review of aging mechanism.....	69
4.1.2	Review of aging modeling.....	73
4.2	Development of aging model.....	75
4.2.1	Modeling of the main reaction and the side reaction.....	76
4.2.2	Modeling of solvent diffusion.....	78
4.2.3	Modeling of side reaction effects.....	83
4.3	Simulation analysis at 25°C.....	87
4.3.1	Analysis of side reaction rate.....	87
4.3.2	Analysis of aging parameters.....	88
4.4	Experimental validation at different temperatures.....	90
4.4.1	Validation of SEI resistance.....	91
4.4.2	Validation of discharge characteristics.....	92

4.4.3	Validation of capacity	94
4.5	Summary of aging model.....	97
Chapter 5	Conclusion	99
Appendix	103
References	106

List of Tables

Table 1: Comparison of computational time (seconds) between FOM and previous ROM.	12
Table 2: Low orders Padé approximation of $C_{s,surf}$	21
Table 3: Comparison of computational time (second) among FOM, previous ROM, and the new approach.	48
Table 4: Test matrix.	51
Table 5: Summary of degradation mechanisms.....	69
Table 6: Summary of side reaction effects	72
Table 7: Effects of the side reaction.	86
Table 8: Parameters of the ROM [45].....	103
Table 9: Parameters of the degradation model.	104

List of Figures

Figure 1: Schematic diagram of a microcell and a single cell.	3
Figure 2: Schematic diagram of current flow under discharging.	4
Figure 3: Schematic diagram of SOC and ion concentration in electrodes.	5
Figure 4: SEM images of LiCoO_2 electrode in different scales: (a) particles (b) surface morphology of a particle [2].	6
Figure 5: Time and error analysis of four order reduction methods for ion concentration in solid.	14
Figure 6: Sandwich structure of the micro cell in a pouch type single cell.	15
Figure 7: Open circuit voltage and equilibrium potentials of both electrodes.....	18
Figure 8: Block diagram of the POD algorithm.....	27
Figure 9: Frequency responses of the surface concentration of a particle on the anode side: analytical exact solution, parabolic and quartic polynomial and the different order of Padé approximation.	30
Figure 10: Time responses of surface concentration of a particle on anode: FDM, quartic polynomial, and 2 nd and 6 th order of the Padé approximation.	31
Figure 11: Stoichiometry number of the anode during full discharge: 0.5C, 1C and 2C rate.	32
Figure 12: Ion concentration in the electrolyte at various times during 1C discharge.	33
Figure 13: Eigenvalue spectrum of the potential data set obtained from the model with FDM during discharge at 1C rate.	34
Figure 14: Electrolyte potential in the center of the cell during discharging with 1C rate.....	36
Figure 15: Electrode potential at the interface between the separator and composite cathode during discharge with 1C rate.	37
Figure 16: Schematic diagram for the ROM for a single cell.....	38

Figure 17: Computational time and error with respect to different sample rate.	39
Figure 18: Comparison of terminal voltage between simulations and experiments during 0.5C, 1C, 2C and 3C discharge.	41
Figure 19: Comparison of terminal voltage between simulations and experiments during 0.5C, 1C, 2C and 3C charge.	42
Figure 20: Percentage errors of the terminal voltage at discharge and charge.	42
Figure 21: Comparison of SOC between simulation and experiments during 0.5C, 1C, 2C and 3C discharge.	43
Figure 22: Comparison of SOC from simulation and experiments during 0.5C, 1C, 2C and 3C charge.	44
Figure 23: Comparison of surface temperature between simulation and experiments during 0.5C, 1C, 2C and 3C discharge.	44
Figure 24: Comparison of surface temperature between simulation and experiments during 0.5C, 1C, 2C and 3C charge.	45
Figure 25: Comparison of terminal voltage between simulation and experiments at multiple charging and discharging cycles.	46
Figure 26: Comparison of terminal voltage between simulation and experiments at a current profile measured at an EV driving cycle.	47
Figure 27: Comparison of computational time and error vs. sample time between the previous ROM [24] and the new proposing ROM.	48
Figure 28: Schematic diagram of a test station.	52
Figure 29: Cycle data with 4C current rate at 25°C.	53
Figure 30: 0.2C discharge curves for Qmax measurement at 60°C.	54
Figure 31: 0.2C discharge curves for Qmax measurement at 40°C.	55
Figure 32: 0.2C discharge curves for Qmax measurement at 25°C- high SOC range.	55
Figure 33: 0.2C discharge curves for Qmax measurement at 25°C- low SOC range.	56
Figure 34: 0.2C discharge curves for Qmax measurement at 0°C.	57

Figure 35: Capacity measurement for every 30 cycles at different temperatures.....	58
Figure 36: EIS measurement vs. model fitted data at 60°C.....	59
Figure 37: EIS measurement vs. model fitted data at 40°C.....	60
Figure 38: EIS measurement vs. model fitted data at 25°C - high SOC.....	60
Figure 39: EIS measurement vs. model fitted data at 25°C - low SOC.....	61
Figure 40: EIS measurement vs. model fitted data at 0°C.....	61
Figure 41: EIS equivalent circuit model.....	62
Figure 42: Model fitted parameter - R_0	63
Figure 43: Model fitted parameter - R_{SEI}	64
Figure 44: 1C discharge curves at various temperatures.....	65
Figure 45: Curve fitting of the diffusion coefficient and film resistance at various temperatures.	66
Figure 46: Self-discharge data and fitted EC diffusivity over time.....	68
Figure 47: Schematic diagram of the main and side reaction on graphite particles.....	70
Figure 48: Concentration of EC molecule in the SEI layer.....	82
Figure 49: EC concentration at the anode graphite particle surface.....	83
Figure 50: Schematic diagram of the SEI formation in a microcell.....	84
Figure 51: Accumulated side reaction rate along the anode thickness direction.....	88
Figure 52: Change of electrode volume fraction and SEI resistance along the anode thickness direction.....	89

Figure 53: Change of electrolyte volume fraction and deposit layer resistance with increasing cycle number.	90
Figure 54: Change of SEI resistance with increasing cycle number.	92
Figure 55: Discharge characteristics of the degraded cell at different number of cycles at 25°C.	93
Figure 56: Discharge characteristics of the degraded cell at different number of cycles at 40°C and 0°C.	94
Figure 57: Relative capacity at different temperatures.	96
Figure 58: Error of the relative capacity estimation at different temperatures.	97

List of Symbols

A	sandwich area of the cell (cm^2)
a_s	specific surface area of electrode (cm^{-1})
c	ion concentration (mol L^{-1})
D	diffusion coefficient ($\text{cm}^2 \text{s}^{-1}$)
E_a	activation energy
F	Faraday constant ($96,487 \text{ C mol}^{-1}$)
h	heat transfer coefficient
I	current of the cell (A)
i_o	exchange current density of intercalation (Acm^{-2})
j^{Li}	reaction rate (Acm^{-3})
k_{iso}	isolation coefficient due to SEI
L	thickness of the micro cell (cm)
Q	capacity of the cell (Ah)
q	amount of ion loss caused by the side reaction (Ah)
R	resistance ($\Omega \text{ cm}^2$) or universal gas constant ($8.3143 \text{ J mol}^{-1} \text{ K}^{-1}$)
R_s	radius of spherical electrode particle (cm)

r	coordinate along the radius of electrode particle (cm)
T	cell temperature (K)
t	time (s)
t_+^0	initial transference number
U	potential (V)
V	voltage (V) or volume of the composite electrode (cm ³)
\tilde{V}	molar volume (cm ³ mol ⁻¹)
x	stoichiometric number of the anode
y	stoichiometric number of the cathode

Greek symbols

α	transfer coefficient for an electrode reaction
δ	thickness (cm)
ε	volume fraction of a porous medium
ϕ	Finite difference method (FDM) solution of potentials
η	surface overpotential of electrode reaction(V)
κ	ionic conductivity of electrolyte (S cm ⁻¹)

σ	conductivity (S cm ⁻¹)
----------	------------------------------------

Subscripts and Superscripts

<i>a</i>	anodic
<i>ave</i>	average value
<i>c</i>	cathodic
<i>D</i>	diffusion
<i>EC</i>	ethylene carbonate
<i>e</i>	electrolyte phase
<i>eff</i>	effective
<i>equi</i>	equilibrium
Li	Lithium ion
main	main reaction
max	maximum
<i>r</i>	radial direction in electrode particle
<i>s</i>	solid phase
<i>sep</i>	separator

<i>side</i>	side reaction
<i>surf</i>	electrode particle surface
<i>T</i>	terminal
0%	0% SOC
100%	100% SOC
+	positive electrode (cathode)
-	negative electrode (anode)

List of Abbreviations

<i>BMS</i>	Battery Management System
<i>BOL</i>	Beginning of Life
<i>BV</i>	Butler-Volmer
<i>DL</i>	Deposit Layer
<i>ECM</i>	Electric Circuit Model
<i>EIS</i>	Electrochemical Impedance Spectroscopy
<i>EOL</i>	End of Life
<i>ETM</i>	Electrochemical Thermal Model
<i>FDM</i>	Finite Difference Method
<i>FOM</i>	Full Order Model
<i>LiPB</i>	Lithium ion Polymer Battery
<i>OCV</i>	Open Circuit Voltage
<i>PDE</i>	Partial Differential Equation
<i>POD</i>	Proper Orthogonal Decomposition
<i>RG</i>	Residue Grouping
<i>ROM</i>	Reduced Order Model

<i>SEI</i>	Solid Electrolyte Interphase
<i>SEM</i>	Scanning Electron Microscopy
<i>SOC</i>	State of Charge
<i>SOH</i>	State of Health
<i>SPM</i>	Single Particle Model
<i>SVD</i>	Singular Value Decomposition

Chapter 1 Introduction

1.1 Background

Advanced energy storage techniques that were used to capture and retrieve dissipated energy improved the energy efficiency in grids or in transportations substantially. Batteries are the desirable choices due to their high coulombic efficiency, high energy, and power density. The most common rechargeable batteries are aqueous electrolyte based batteries, which include lead acid, nickel cadmium, nickel metal hydride, and lithium ion batteries [1]. Among the various battery types, lithium ion batteries are mostly preferred because of their highest power and energy density as well as the reduced manufacturing cost triggered by the rapidly growing electronic market. The cells can be manufactured into different types dependent upon the way of packaging, which include cylindrical, coin, prismatic, and pouch type. Compared to the other three types of cell packaging, the pouch cells employ large sizes of active areas by means of folding electrodes, electrolytes, and separators together, which facilitates the new applications such as electric and hybrid vehicles that require increased power and energy density. On the other hand, these high power cells can be quickly degraded followed by fast performance drop and instability. This is due to the high heat generation associated with high ion transport and gradient of ion concentrations in conjunction with the varying environmental operating conditions.

The working mechanism of a cell is very complex and hard to understand in details, which presents one of the technical barriers from optimal design and states monitoring. Model-based battery management is an elegant approach that enables monitoring of battery states such as

state-of-charge (SOC) or state-of-health (SOH), which are required to ensure safe operation of the battery. Traditionally, empirical or electric circuit models are preferably used for batteries because of simplicity to approximate the terminal behaviors. Nevertheless, these approaches ignore detailed physical effects and operating conditions. By contrast, models based on electrochemical principles can better represent internal physical quantities that include ion distributions and potential gradients, but the structure is sophisticated and the parameters are difficult to characterize.

1.2 Working principle and battery chemistry

A pouch type lithium ion polymer single cell is made of stacked microcells that are connected in parallel by current collectors. The microcell has a sandwich structure in the thickness direction that comprises of composite electrodes mixed with electrolyte and a separator in between. The composite electrodes are made of active materials, electrolytes and binders, where the particles dispersed on electrodes are modeled as uniformly distributed spheres. A schematic diagram of this cell is shown in Figure 1, where the active material for the anode is graphite and that on the cathode is metal oxides.

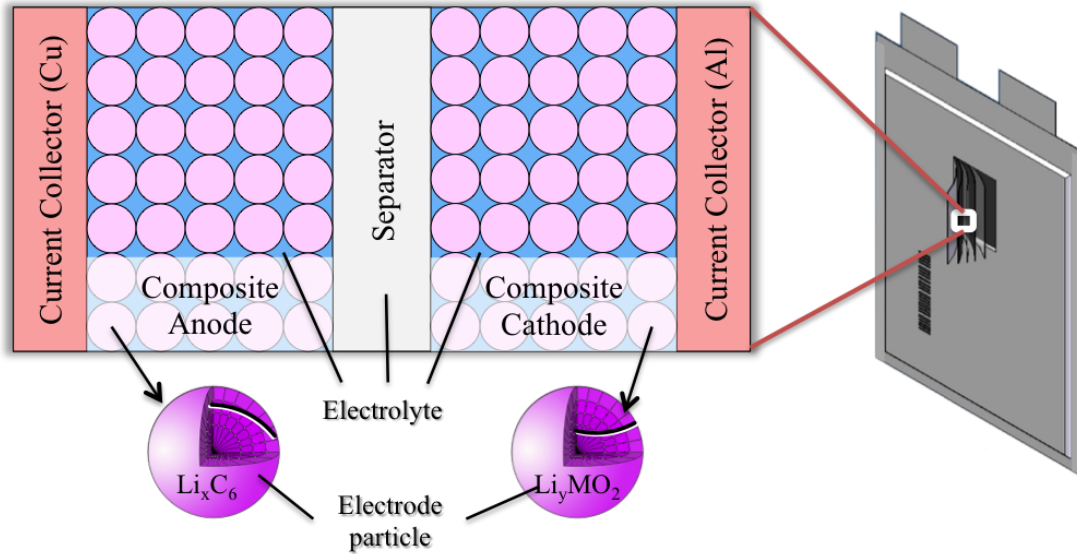


Figure 1: Schematic diagram of a microcell and a single cell.

While cells are discharging or charging, ions transport through the electrolyte and chemically react at active materials, then diffuse in the solid particles, and finally rest after intercalation in a lattice structure. Meanwhile, electrons flow through an external circuit and complete the redox process. Thus, there are two coexisting current flows during this process, ionic current and electron current. The current flowing through the battery is the ionic current, which flows in the electrolyte, and the current flowing in the external circuit is electron current. A schematic diagram of the current flows under discharging is shown in Figure 2. When the cell is discharged, the lithium ions and electrons are separated at the anode. The lithium ions transport to the cathode through electrolyte while the electrons transport to the cathode through an external circuit. Both the lithium ions and the electrons finally combine at the cathode and complete the battery reaction. The current flow of lithium ions and electrons are reversed during the charging process.

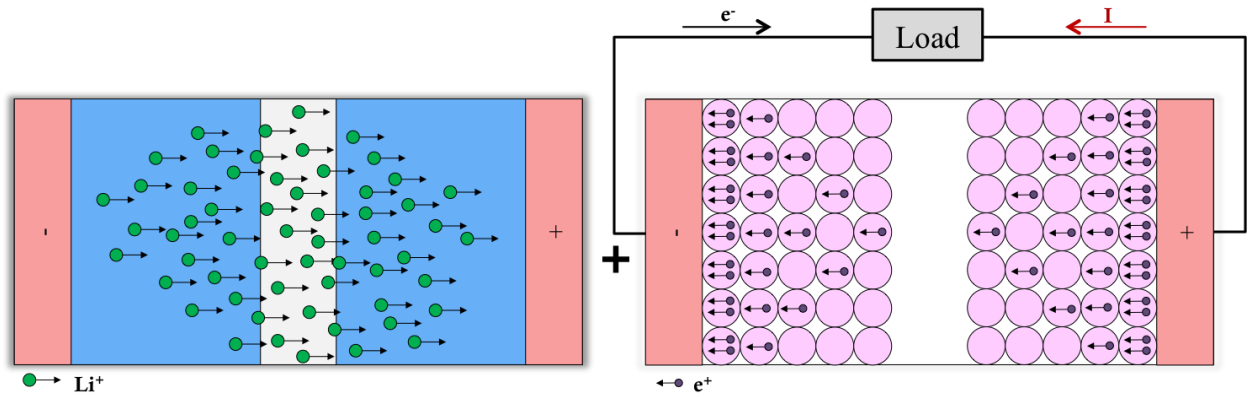


Figure 2: Schematic diagram of current flow under discharging.

The electrode material has an intrinsic equilibrium potential against electrolyte that is a function of the stoichiometric number that presents a ratio between the current and the maximum lithium ion concentration in the electrode. At the equilibrium state under no macroscopic current across the surface, the potential difference between the electrode and electrolyte is the same as that at the equilibrium state. The difference between the equilibrium potentials of cathode and anode is the same as that at the terminal, which is call the open circuit voltage (OCV).

The state of charge (SOC) of a battery is defined as the percentage ratio of the releasable charge to the maximum charge at a particular time. At 100% SOC, the anode has the highest lithium ion concentration while the cathode has the lowest one. At 0% SOC, the ion concentration is reversed as shown in Figure 3. Changing of SOC implies shuttling the lithium ions between the anode and cathode.

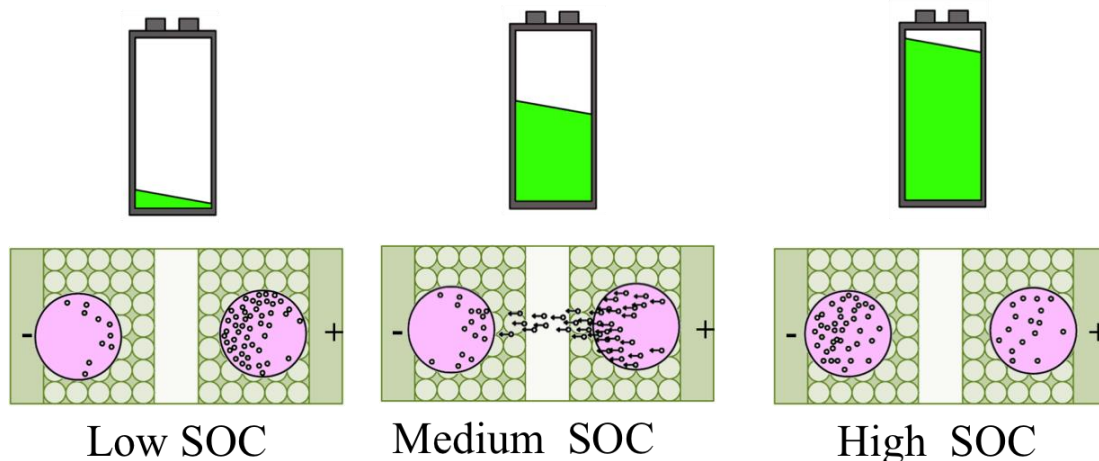


Figure 3: Schematic diagram of SOC and ion concentration in electrodes.

The morphology of the electrode particles is an important factor on the performance of lithium ion battery. The porous structure expands the surface of the active area so that power loss is reduced by lower overpotential at certain current density, which benefits the chemical reaction that takes place at the interface between the electrode particles and electrolyte. However, the side reaction that also takes place at this interface can corrode active material and eventually lead to capacity loss. A porous structure of a LiCoO_2 electrode imaged by the scanning electron microscopy (SEM) is shown in Figure 4. Multiple interspaces can be detected among the granular crystalline grains. When the LiCoO_2 electrode material is used in lithium ion batteries, the liquid electrolyte can be soaked into the interspaces, so that it can directly contact with the crystalline grains. Thus, the lithium ion in the liquid electrolyte can easily diffuse throughout the LiCoO_2 electrode, which is beneficial for a good electrochemical performance of the material at high current density.

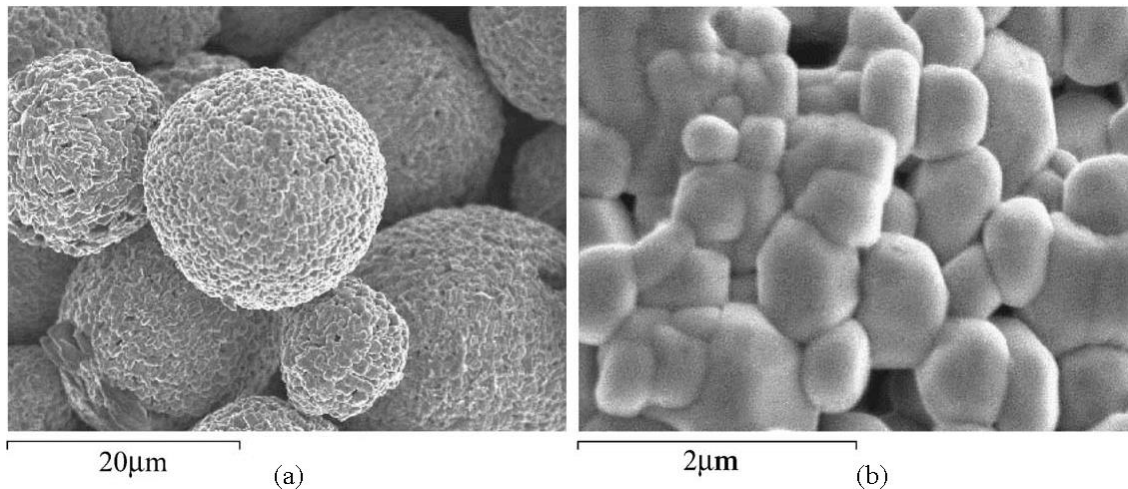


Figure 4: SEM images of LiCoO₂ electrode in different scales: (a) particles (b) surface morphology of a particle [2].

In recent years, the most commonly used anode materials are carbon, Sn and Si-based alloys, metal oxides and Li₄Ti₅O₁₂ spinel, while commonly used cathode materials are Li-S, Li-air, Li₂MnO₄ (LMO), Li₂MnO₃·Li[MnNiCo]O₂ (NMC), LiFePO₄ (LFP) and LiMn_{1.5}Ni_{0.5}O₄ [3]. The separator materials are usually composed of polymers, such as polyethylene oxide (PEO). The most common lithium salt for electrolyte is LiPF₆ and the solutions are usually ethylene carbonates (EC) and propylene carbonate (PC) [4].

1.3 Motivation and objectives

The reliable and safe operation of batteries can be ensured by a battery management system (BMS) that monitors and controls operating conditions based on knowledge of battery states. Generally, a computational model is embedded in the BMS and used to estimate the battery states in real time and predict the battery life. Models based on the electrochemical principles are a preferable choice because of representation of internal variables during operation. However,

solving the partial differential equations of the full order model (FOM) is highly computationally intensive, so the FOM is inappropriate for real time applications. Therefore, it is indispensable to develop a reduced order model (ROM) that is capable of monitoring the battery performances and running in real time while the accuracy can be maintained. A proposing ROM is developed by integrating different model reduction techniques targeting reduction of the computational time needed for the FOM. The total computational time can be reduced to less than one-tenth of the FOM, while the static and dynamic accuracy can be maintained.

In addition, prediction of battery life is of great significance in BMS. A physics-based model is developed that describes the aging process and facilitates diagnosis and prognosis of the battery states, so battery state of health (SOH) can be estimated. Several improvements for aging mechanisms have been made that include effects of the solvent diffusion on the side reaction and effects of the solvent concentration on exchange current density. Then, the temperature dependency of the model parameters is incorporated using the energy equations. Finally, the ROM with the aging model is validated against experimental data, which enables prediction of the battery life.

1.4 Dissertation structure

The basic structure of the dissertation is shown as follows:

1. Introduction

This section involves the research background, battery working principles, motivation, and objectives.

2. Reduced order model

Firstly, the model order reduction techniques are reviewed, followed by an introduction of the electrochemical full order model initially developed by other researchers [13]. Then, the mathematical formulations for the individual part in the ROM are explained in detail and the performances are shown in simulation analysis. The experimental validation is conducted with respect to the terminal voltage during constant charging and discharge and driving cycles.

3. Experimental investigation

Since the development of aging model requires abundant experimental data analysis, especially parameter identification part, the experimental investigation needs preparation of test stations, analysis of cycling data and EIS data, temperature dependent parameter determination, which is described below.

4. Aging model

This section describes the development of aging model. The aging mechanism and existing modeling techniques are reviewed initially, followed by the detailed modeling steps. Then, the change of model parameters with respect to prolonged cycle numbers are analyzed at 25°C. The aging model is validated against experimental data that includes discharge characteristics and capacity changes at different temperatures.

5. Conclusion

Chapter 2 Reduced order model

2.1 Review of model order reduction techniques

Lithium ion batteries have been widely adopted as energy storage for different power systems due to their high power and energy density and reduced manufacturing costs triggered by the growing market for electronic devices. However, improper operating conditions such as continuous overcharge or undercharge can accelerate degradation processes and lead to early failures. Model based battery management is an elegant approach that enables monitoring of battery performances such as state of charge (SOC) or state of health (SOH), which are crucial for the safe operation of batteries.

The models can be classified into two categories, equivalent circuit models (ECM) [5] and electrochemical thermal models (ETM) [12]. The ECM is easy to construct and fast in simulation, but cannot represent battery behavior completely. Conversely, the ETM based on electrochemical kinetics, mass balance, charge conservation and thermal principles is capable of representing the battery behavior accurately and providing internal variables like ion concentrations. However, it is inappropriate for implementation into microcontrollers that work in real time due to the large amount of calculations caused by numerically solving discretized partial differential equations as well as nonlinear equations. The first electrochemical model proposed by Doyle et al. [5] assumed that a cell is made of several thin-film layers and the working mechanism is described with electrochemical principles. Fuller et al. [6] then extended the model by considering other cathode materials, such as LiCoO_2 and LiMn_2O_4 , to investigate the effects of material property parameters on the performance of a cell. Further improvement of

the model has considered the inclusion of a transference number [7], an activity coefficient for the electrolyte [8], a diffusion coefficient for LiPF_6 electrolyte [9], and multiple particle size distributions [10]. ETM describes the charge transport phenomenon in composite electrodes and electrolyte by a set of coupled partial differential equations (PDEs). The PDEs are discretized and numerically solved in radial and through-the-plane direction using the finite difference method (FDM). The resulting Full Order Model (FOM) provides high accuracy although the calculation of large amount states variables is quite time consuming. In particular, the electrodes are modeled with spherical particles, and the evaluation of ion concentrations in the particles should be carried out in the sphere radial direction that requires an extra discretization, which multiplies the number of state variables as well as the computational time.

Models for real-time control purpose should be able to represent key physical phenomena within a reasonable time given by the implementation. Therefore, the ETM should be simplified while considering the accuracy and computational time. Several model order reduction techniques have been proposed in the literature to reduce computational expense. Review of the literature has shown that those methods can be sorted into two groups: one is based on numerical calculations and the other one is based on analytical expressions.

The numerical methods require discretization of the PDEs and reducing the matrix size by assorting eigenvalues of the system. A representative method is the residue grouping (RG) method that lumps states with similar eigenvalues, which reduces the order of the matrices [14]. Proper Orthogonal Decomposition (POD) technique approximates FOM behavior by a low order sub-model derived from the most significant eigenvalues of matrices [15]. Single particle model (SPM) is also widely adopted in the literatures, which ignores the variation in the thickness direction and considers only one single particle in each electrode [16].

The analytical methods are replacements of the PDE for the Fick's second law that describes the ion diffusion process that takes place in electrode particles. One of the analytical approaches employed a parabolic profile based on volume average equation [17]. Accuracy is further improved using a quartic profile instead [18]. Another analytical approach eliminated the independent spatial variables in the diffusion equation by applying the pseudo steady state (PSS) method, which is originated from finite integral transform techniques [19]. In addition, the Galerkin method has also been adopted to reduce the computational complexity of the ion concentration [20][22]. Furthermore, Padé approximation is applied to the transfer function between current density and ion concentrations [23], which is derived for the study of the diffusion impedance in spheres [22].

The two groups of approaches aforementioned have their own superiorities and limitations. The numerical methods are generally applicable to each part of the ETM and allow for systematic reduction of a model to a certain level that meets requirements for accuracy. Numerical methods have better frequency responses compared to the analytical expressions. However, the inevitable discretization increases the complexity of the algorithms. The analytical expressions describe the model dynamics as a function of time and space in a more straightforward way and avoid discretization of the PDEs. Nevertheless, those approximations usually provide less accuracy in the high frequency range and the determination of the coefficients is quite time consuming, especially in the PSS method. In spite of the fact that the Padé approximation is based on the analytical transfer function of the ion diffusion impedance, it has excellent performance in a wide frequency range because the transfer functions are exact solutions of the PDE. The features of high accuracy and efficiency enable it to be a promising replacement of the diffusion equation in electrode particles.

In our previous research work for the development of ROM, order reductions and simplifications were performed, including polynomial approximation for ion concentration in electrode particles, residue grouping (RG) for ion concentrations in the electrolyte, and linearization of the Butler-Volmer equation [24]. Time analysis was carried out using the MATLAB profiler, as shown in Table 1, where the time measured in seconds indicates the calculation duration for 1C discharge from 100% SOC to 0% SOC with a sample rate of 1s. The calculation time for the major variables in the model are listed individually, where C_s , C_e and Φ denote the ion concentration in electrode particles, in electrolytes, and potential in electrodes and electrolytes, respectively. ROM can reduce computational time to approximately one-fifth of FOM, whereby C_s and Φ remain the most time consuming parts of the calculation.

Table 1: Comparison of computational time (seconds) between FOM and previous ROM.

	FOM	Previous ROM [24]
Total	50.74	10.09
C_s	19.25	6.05
C_e	1.93	0.05
Φ	7.01	3.36
Others	22.55	0.63

To reduce the calculation time for ion concentrations and potentials, different techniques were investigated to simplify the model. Four potential candidates for ion concentration in

electrode particles governed by the Fick's law are polynomial approximation (Poly), Padé approximation (Pade), POD and Galerkin Reformulation (GR), whose performances are compared and analyzed [24]. Computational time and error of the four methods are plotted in Figure 5, where the time denotes the simulation duration of $C_{s,surf}$ when a pulse current is applied for 1 hour while the error is the accumulated difference given by comparing them with a FDM solution.

The results of the analysis showed that the performance of the Padé approximation was superior to the other options since the calculation time remained within a reasonable tolerance and the error quickly converged to zero when the order number increased. Moreover, the approximation allowed for a systematic reduction of orders dependent upon the level of accuracy required.

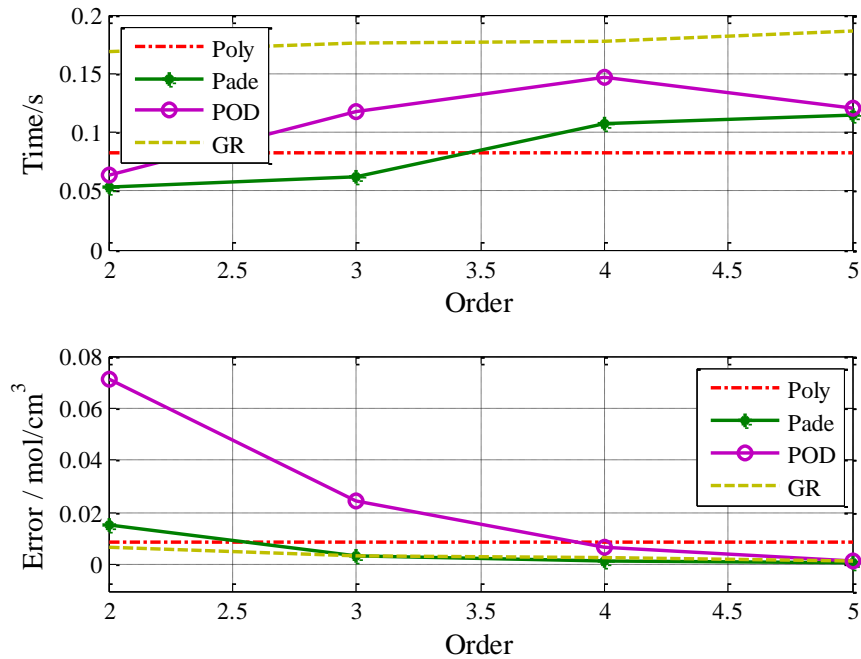


Figure 5: Time and error analysis of four order reduction methods for ion concentration in solid.

On the other hand, RG is retained for ion concentration in the electrolyte. The POD method as applied for reduction of large-scale ODE systems is used to reduce the matrix size for potentials in electrode and electrolyte.

2.2 Setup of the full order electrochemical model [13]

A FOM for a pouch type lithium ion polymer single cell is a quasi-three dimensional model developed based on electrochemical thermal principles. The FOM of the single is assumed to be made of stacked microcells that are connected in parallel by current collectors. Due to the high conductivity of the current collectors, the lateral current flow from one microcell to another can be neglected and the potentials on current collectors for each microcell are assumed to be identical. Thus, the entire single cell can be regarded as a microcell with only a pair of current collectors. A schematic diagram for modeling of a single cell is depicted in Figure 6.

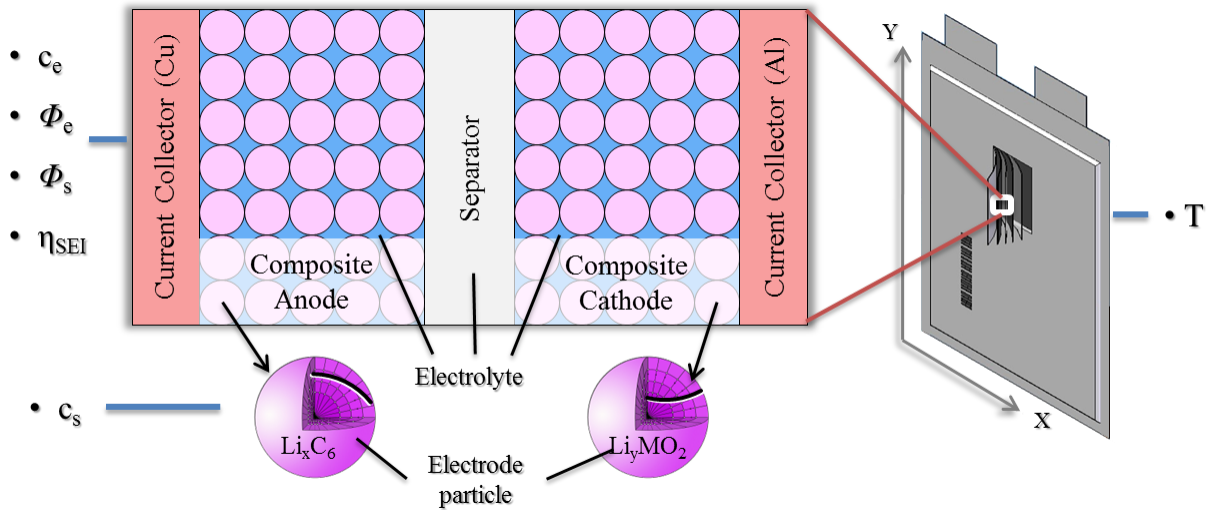


Figure 6: Sandwich structure of the micro cell in a pouch type single cell.

The input variables and initial operating conditions are current, voltage and ambient temperature as a function of time. The output variables are dynamic responses of the loads, including terminal voltage, current, SOC, temperature distributions, lithium concentrations, potentials, and current densities.

2.2.1 Ion transport and charge conservation

Chemical reactions take place at the surface of electrode particles, followed by ion diffusion in electrodes until full intercalation. The electrode particles are modeled as porous spheres where ions diffuse only in the radial direction driven by the gradient of ion concentration. The ion concentration in electrode particles can be described by the Fick's second law if diffusion:

$$\frac{\partial c_s}{\partial t} = \frac{D_s}{r^2} \frac{\partial}{\partial r} \left(r^2 \frac{\partial c_s}{\partial r} \right) \quad (1)$$

with boundary conditions:

$$\frac{1}{r} \frac{\partial c_s}{\partial r} \Big|_{r=0} = 0 \quad \text{and} \quad D_s \frac{\partial c_s}{\partial r} \Big|_{r=R_s} = \frac{-j^{Li}}{a_s F} \quad (2)$$

where r is the radial coordinate of an electrode particle, R_s is the radius of electrode particles, D_s is the solid phase diffusion coefficient, F is the Faraday's constant, j^{Li} is the current density, a_s is the interfacial surface area calculated from $3 \varepsilon_s / R_s$ and ε_s is the active material volume fraction.

Distribution of ion concentration in electrolyte and its boundary conditions are shown as follows:

$$\frac{\partial(\varepsilon_e c_e)}{\partial t} = \frac{\partial}{\partial x} \left(D_e^{\text{eff}} \frac{\partial c_e}{\partial x} \right) + \frac{1-t_+^0}{F} j^{\text{Li}} \quad (3)$$

$$\frac{\partial c_e}{\partial x} \Big|_{x=0} = \frac{\partial c_e}{\partial x} \Big|_{x=L} = 0$$

where ε_e is the electrolyte phase volume fraction, t_+^0 is the transference number, D_e^{eff} is the effective diffusion coefficient accounting for tortuosity by correcting diffusion coefficient with electrolyte phase volume fraction ε_e and Bruggeman's exponent as shown in the following equation:

$$D_e^{\text{eff}} = D_e \times \varepsilon_e^p \quad (4)$$

The charge transport in solid electrode is governed by the Ohm's law:

$$\frac{\partial}{\partial x} (\sigma^{\text{eff}} \times \frac{\partial j_s}{\partial x}) = j^{\text{Li}} \quad (5)$$

with boundary conditions:

$$-\sigma^{\text{eff}} \frac{\partial j_s}{\partial x} \Big|_{x=0} = -\sigma^{\text{eff}} \frac{\partial j_s}{\partial x} \Big|_{x=L} = \frac{I}{A} \quad (6)$$

$$\frac{\partial j_s}{\partial x} \Big|_{x=L_-} = \frac{\partial j_s}{\partial x} \Big|_{x=L_- + L_{\text{sep}}} = 0$$

where L is the thickness of the cell, L- is the thickness of the negative electrode, Lsep is the thickness of the separator, A is the plate area of electrode, and σ^{eff} is the effective solid phase conductivity that is obtained from the conductivity σ multiplied with active material fraction ε_s , as shown in the following equation:

$$\sigma^{\text{eff}} = \sigma \cdot \varepsilon_s \quad (7)$$

The amount of charges produced in oxidation process should be equal to those consumed in the reduction process. The charge conservation in electrolyte is governed by the Ohm's law:

$$\frac{\partial}{\partial x} \left(k^{\text{eff}} \frac{\partial j_e}{\partial x} \right) + \frac{\partial}{\partial x} \left(k_D^{\text{eff}} \frac{\partial \ln c_e}{\partial x} \right) + j^{\text{Li}} = 0 \quad (8)$$

$$\frac{\partial j_e}{\partial x} \Big|_{x=0} = \frac{\partial j_e}{\partial x} \Big|_{x=L} = 0$$

The ionic conductivity, κ^{eff} , is obtained from electrolyte phase volume fraction ε_e and Bruggeman's exponent p , as shown in the following equation:

$$k^{\text{eff}} = k \times \varepsilon_e^p \quad (9)$$

2.2.2 Butler-Volmer equation and equilibrium potentials

The current produced by chemical reactions at the interface between electrode and electrolyte is obtained from the Butler-Volmer electrochemical kinetic equation:

$$j^{\text{Li}} = a_s i_0 \left\{ \exp \left[\frac{\alpha_a F}{RT} (h - h_{\text{SEI}}) \right] - \exp \left[- \frac{\alpha_c F}{RT} (h - h_{\text{SEI}}) \right] \right\} \quad (10)$$

where i_0 is the exchange current density, α_a and α_c are the anodic and cathodic charge transfer coefficient, R is the universal gas constant, T is the temperature, and η is the overpotential defined as the potential difference between the solid, electrolyte and the equilibrium. The SEI on anode side is approximated with a resistor, R_{SEI} , that causes an additional overpotential η_{SEI} , as shown below:

$$h = f_s - f_e - U \quad (11)$$

$$h_{\text{SEI}} = \frac{j^{\text{Li}} R_{\text{SEI}}}{a_s}$$

The OCV-SOC curve is obtained by pulse discharge, where terminal voltage and the SOC are measured after the battery is discharged with a small C rate for a short time and completely

relaxed. The measured OCV is the difference between the equilibrium potentials for the positive and negative electrode, where the potential for the negative electrode, U_- , is approximated with an empirical equation, as provided in equation(12). The equilibrium potentials versus stoichiometric numbers are plotted in Figure 7.

$$U_-(x) = 8.00229 + 5.0647x - 12.578x^{1/2} - 8.6322 \cdot 10^{-4}x^{-1} + 2.1765 \cdot 10^{-5}x^{3/2} - 0.46016 \cdot \exp(15(0.06 - x)) - 0.55364 \cdot \exp(-2.4326(x - 0.92)) \quad (12)$$

$$x = c_{s,surf}^- / c_{s,max}^-$$

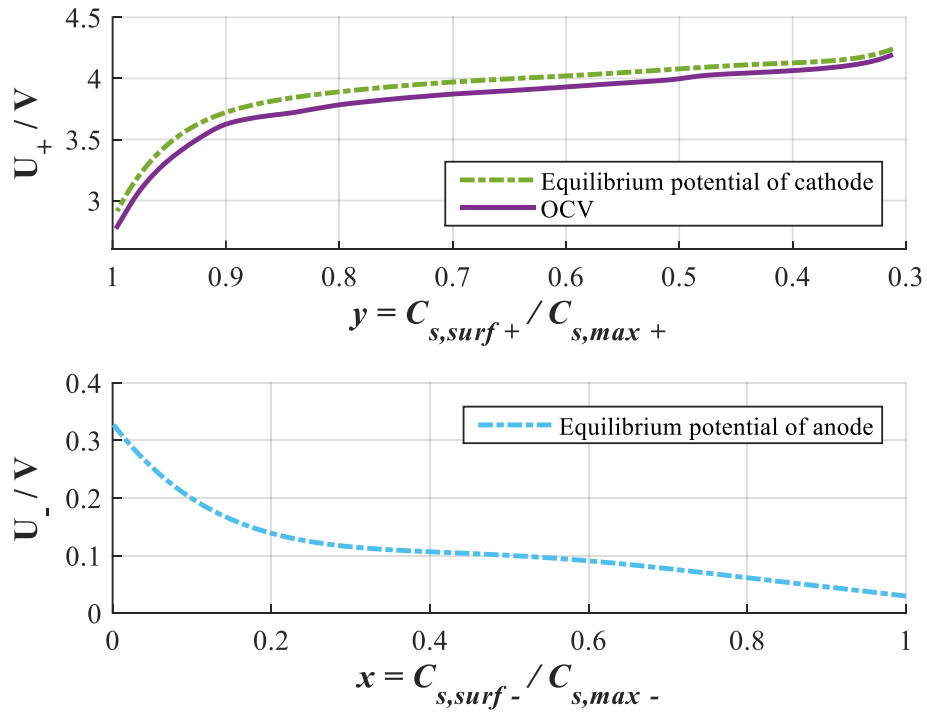


Figure 7: Open circuit voltage and equilibrium potentials of both electrodes.

2.2.3 Energy equation

The temperature of the cell is described using the energy equation under isothermal condition.

$$\rho C_p \frac{\partial T}{\partial t} = Q_{gen} - q \quad (13)$$

where ρ and C_p are the density and heat capacity, Q_{gen} is the heat generation rate per unit volume in a cell during charging/discharging and q is the heat transfer rate per unit volume between the cell and its surroundings expressed as:

$$q = h(T - T_{amb}) \quad (14)$$

where h and T_{amb} are the heat transfer coefficient and ambient temperature, respectively. For the thermal chambers used in the experimental work, the heat transfer coefficient takes the value between 50-80 W/Km².

In general, the heat generation is expressed as a sum of irreversible and reversible heat generation term. The irreversible heat source term at a given current is determined by the difference between the terminal voltage and OCV, while the reversible heat source term is the change of entropy at a given temperature that is the same as the change of OCV over temperature.

$$Q_{gen} = I \left(U_{OCV} - V_T - T \cdot \frac{\partial U_{OCV}}{\partial T} \right) \quad (15)$$

where U_{OCV} is the open circuit voltage, V_T is the terminal voltage, and $\frac{\partial U_{OCV}}{\partial T}$ is the entropy coefficient.

The equation above becomes zero when the terminal current goes to zero. In fact, heat is continuously generated even though the terminal current is zero during relaxation after charging or discharging. This extra heat source term is generated by ionic current in electrodes caused by the gradient of ion concentrations and is called the heat of mixing that is derived from the relationship between the power input and chemical energy increase and added as an additional heat generation source as shown below [13]:

$$Q_{gen} = \frac{1}{L} \int_L \left(DU_{equ}^+ \cdot i(r, l) - DU_{equ}^- \cdot i(r, l) \right) dl + I \left(U_{OCV} - V_T - T \cdot \frac{\partial U_{OCV}}{\partial T} \right) \quad (16)$$

where U_{equ} and i denote the equilibrium potential and the local current density, respectively.

2.3 Development of a reduced order model

Coupled governing equations consist of nonlinear equations and PDEs that are numerically solved by the FDM in FOM. The reductions and simplifications of the equations for each part of the model are described below.

2.3.1 Ion concentration in electrode particles

Ion diffusion in a particle is described by the second order Fick's law, whose solution provides gradients of ion concentration, C_s , along the radial direction in electrode particles. For control oriented models, the ion concentration on the particle surface, $C_{s,surf}$, and the volume average concentration, $C_{s,ave}$, are critical variables because of their direct relationship to the reactions that affect intercalation in active materials and SOC. Analytical solutions of the Fick's law provide two transfer functions where the current density, j^{Li} , and two ion concentrations,

$C_{s,surf}$, $C_{s,ave}$, are regarded as an input variable and output variables, respectively, as shown as follows [21]:

$$\frac{C_{s,surf}(s)}{j^{Li}(s)} = \frac{1}{a_s F} \left(\frac{R_s}{D_s} \right) \left[\frac{\tanh(b)}{\tanh(b) - b} \right] \quad (17)$$

where $b = R_s \sqrt{s/D_s}$.

$$\frac{C_{s,ave}(s)}{j^{Li}(s)} = -\frac{3}{R_s a_s F s} \quad (18)$$

The Q^{th} order Padé approximation for $C_{s,surf}$ in equation (17) results in the form of:

$$\frac{C_{s,surf}(s)}{j^{Li}(s)} = \frac{a_0 + a_1 s + a_2 s^2 + \dots + a_{Q-1} s^{Q-1}}{s(1 + b_2 s + b_3 s^2 + \dots + b_Q s^{Q-1})} \quad (19)$$

The coefficients a_0, a_1, \dots, a_{Q-1} and b_2, b_3, \dots, b_Q are determined by comparing the derivatives of equation (17) with equation (19) at $s=0$. The resulting low order Padé approximations are listed in Table 2, where $m = \frac{1}{a_s F D_s}$.

Table 2: Low orders Padé approximation of $C_{s,surf}$.

Order	Padé approximation
2nd	$\frac{\frac{3D_s m}{R_s} - \frac{2mR_s s}{7}}{s + \frac{R_s^2 s^2}{35D_s}}$

3rd	$\frac{\frac{3D_s m}{R_s} - \frac{4mR_s s}{11} - \frac{mR_s^3 s^2}{165D_s}}{s + \frac{3R_s^2 s^2}{55D_s} + \frac{R_s^4 s^3}{3465D_s^2}}$
4th	$\frac{\frac{3D_s m}{R_s} - \frac{2mR_s s}{5} - \frac{2mR_s^3 s^2}{195D_s} - \frac{4mR_s^5 s^3}{75075D_s^2}}{s + \frac{R_s^2 s^2}{15D_s} + \frac{2R_s^4 s^3}{2275D_s^2} + \frac{R_s^6 s^4}{675675D_s^3}}$
5th	$\frac{\frac{3D_s m}{R_s} - \frac{8mR_s s}{19} - \frac{21mR_s^3 s^2}{1615D_s} - \frac{4mR_s^5 s^3}{33915D_s^2} - \frac{mR_s^7 s^4}{3968055D_s^3}}{s + \frac{7R_s^2 s^2}{95D_s} + \frac{3R_s^4 s^3}{2261D_s^2} + \frac{2R_s^6 s^4}{305235D_s^3} + \frac{R_s^8 s^5}{218263025D_s^3}}$

A state space representation in controllable canonical form of the transfer function in equation (18) and (19) is shown as:

$$\begin{aligned} \dot{\vec{x}} &= A_1 \vec{x} + B_1 j^{Li} \\ \vec{y} &= C_1 \vec{x} \end{aligned} \tag{20}$$

where

$$\begin{aligned}
A_1 &= \begin{bmatrix} 0 & 1 & 0 & 0 & \dots & 0 \\ 0 & 0 & 1 & 0 & \dots & 0 \\ 0 & 0 & 0 & 1 & \dots & 0 \\ \vdots & \vdots & \vdots & \vdots & \ddots & \vdots \\ 0 & 0 & 0 & 0 & \dots & 1 \\ 0 & -\frac{1}{b_Q} & -\frac{b_2}{b_Q} & -\frac{b_3}{b_Q} & \dots & -\frac{b_{Q-1}}{b_Q} \end{bmatrix}, & B_1 &= \begin{bmatrix} 0 \\ 0 \\ 0 \\ \vdots \\ 0 \\ 1 \end{bmatrix}, & \bar{x} &= \begin{bmatrix} x_1 \\ x_2 \\ x_3 \\ \vdots \\ x_{Q-1} \\ x_Q \end{bmatrix} \\
C_1 &= \begin{bmatrix} \frac{a_0}{b_Q} & \frac{a_1}{b_Q} & \frac{a_2}{b_Q} & \frac{a_3}{b_Q} & \dots & \frac{a_{Q-1}}{b_Q} \\ \frac{a_0}{b_Q} & \frac{a_0 b_2}{b_Q} & \frac{a_0 b_3}{b_Q} & \frac{a_0 b_4}{b_Q} & \dots & a_0 \end{bmatrix}, & \bar{y} &= \begin{bmatrix} C_{s,surf} \\ C_{s,ave} \end{bmatrix}
\end{aligned} \tag{21}$$

Initial conditions for solving the equations above are steady state, $\dot{x} = 0$, zero input $j^{Li} = 0$ and uniform concentration, $C_{s,surf} = C_{s,ave}$. The first two conditions result in a linear equation, $A\bar{x} = 0$, that yields a solution with one degree of freedom, $\bar{x}_0 = [x_0 \ 0 \ 0 \ \dots \ 0 \ 0]^T$. The third condition gives an initial value of the concentration, $C_{s,surf} = C_{s,ave} = C_{s,0}$. As a result, the initial state is presented as follows:

$$\bar{x}_0 = \begin{bmatrix} C_{s,0} \frac{b_Q}{a_0} & 0 & 0 & \dots & 0 & 0 \end{bmatrix}^T \tag{22}$$

2.3.2 Ion concentration in electrolyte

The RG method is used to reduce the PDE that describes ion transport in electrolytes, where current density across each electrode is assumed to be uniform, as shown in equation (23):

$$\begin{aligned}
j_-^{Li} &= \frac{I}{AL_-} \quad (\text{Negative electrode}) \\
j_{sep}^{Li} &= 0 \quad (\text{separator}) \\
j_+^{Li} &= \frac{I}{AL_+} \quad (\text{Positive electrode})
\end{aligned} \tag{23}$$

The PDE is discretized by the FDM and the resulting equations are converted into the state space representation:

$$\begin{aligned}
\dot{\vec{x}} &= A_2 \vec{x} + B_2 I \\
y &= C_2 \vec{x} + D_2 I
\end{aligned} \tag{24}$$

The equation above is a single input M output linear system with matrices A_2, B_2, C_2 and D_2 that have dimensions of $M \times M, M \times 1, M \times M, M \times 1$, where M denotes the number of discrete node points along the microcell thickness direction. The input variable is the applied current I and the output is a $M \times 1$ vector that indicates ion concentration, C_e , at each node point.

The state equation is transformed to a modal canonical form with:

$$\begin{aligned}
\hat{A}_2 &= \text{diag}[\lambda_1 \quad \lambda_2 \quad \cdots \quad \lambda_M] \\
\hat{B}_2 &= [1 \quad 1 \quad \cdots \quad 1]^T \\
\hat{C}_2 &= [\bar{r}_1 \lambda_1 \quad \bar{r}_2 \lambda_2 \quad \cdots \quad \bar{r}_M \lambda_M] \\
\hat{D}_2 &= \left[Z + \sum_{k=1}^M \bar{r}_k \right]
\end{aligned} \tag{25}$$

where λ_k is the eigenvalues of the system matrix, A_2 , Z is the steady state vector evaluated by

$Z = -C_2 A_2^{-1} B_2 + D_2$ and \bar{r}_k is the residue vector obtained by:

$$\vec{r}_k = \frac{C_2 \vec{q}_k \vec{p}_k B_2}{\lambda_k} \quad (26)$$

\vec{q}_k and \vec{p}_k denote the right and left eigenvectors of the system matrix A_2 and $A_2 \vec{q}_k = \lambda_k \vec{q}_k$, $\vec{p}_k A_2 = \lambda_k \vec{p}_k$.

The M th order system is reduced to the N th order by grouping the residues according to the similarity of the eigenvalues [13]. The grouped residue vectors and the grouped eigenvalues are defined as:

$$\vec{r}_f = \sum_{k=k_{f-1}+1}^{k_f} \vec{r}_k, \quad \lambda_f = \frac{\sum_{k=k_{f-1}+1}^{k_f} \lambda_k \vec{r}_k}{\vec{r}_f} \quad (27)$$

The N th order state equation is constructed with the reduced matrices $A_2^*, B_2^*, C_2^*, D_2^*$ that have a dimension of $N \times N, N \times 1, M \times N, M \times 1$:

$$\begin{aligned} A_2^* &= \text{diag}[\lambda_1 \quad \lambda_2 \quad \cdots \quad \lambda_N] \\ B_2^* &= [1 \quad 1 \quad \cdots \quad 1]^T \\ C_2^* &= [\vec{r}_1 \lambda_1 \quad \vec{r}_2 \lambda_2 \quad \cdots \quad \vec{r}_N \lambda_N] \\ D_2^* &= \left[Z + \sum_{f=1}^N \vec{r}_f \right] \end{aligned} \quad (28)$$

2.3.3 Potentials in electrodes and electrolyte

POD is a mathematical procedure that is used to find a basis for a modal decomposition of a data set. The data applied here is the rigorous solution of the potentials in electrode and electrolyte obtained by FDM. The governing equations for charge conservation in electrode and

electrolyte are discretized and the resulting equations are expressed in the matrix form as follows:

$$A_3 \vec{\phi} = b \quad (29)$$

where $\vec{\phi}$ is the FDM solution vector of the potentials at each grid points, A_3 and b denote the coefficients matrix and constant vector.

$\vec{\phi}$ can be approximated by a linear combination of the first N proper orthogonal modes (POMs) as shown in equation (30), where $\vec{\phi}_{appr}$ is the approximation solution, Φ is the POMs and a is the reduction variables.

$$\vec{\phi}_{appr} = \Phi \cdot \vec{a} \quad (30)$$

The POMs are the eigenvectors obtained by singular value decomposition of the discrete kernel given by $\vec{\kappa} = \vec{\phi}^T \cdot \vec{\phi}$ and sorted in a manner that the corresponding eigenvalues are in a non-increasing order, as shown in equation (31). Σ is the diagonal matrix of eigenvalues and N denotes the model order that we applied in POD.

$$\begin{aligned} [U \quad \Sigma \quad V] &= \text{svd}(\vec{\phi}_{full}^T \cdot \vec{\phi}_{full}) \\ \Phi &= U(:, 1:N) \end{aligned} \quad (31)$$

The reduction variables, \vec{a} , are solved by substituting equation (30) into equation (29), which yields equation (32):

$$\begin{aligned} A_3(\Phi \cdot \vec{a}) &= b \\ \vec{a} &= \Phi^T A_3^{-1} b \end{aligned} \quad (32)$$

The selected POMs form a basis that facilitates to capture the dominant characteristics of the system dynamics and enables representation of the most significant information of the variables under various circumstances. In this work, the potential data set $\vec{\phi}$ used to build the kernel $\bar{\kappa}$ is evaluated under 1C discharge condition.

A schematic block diagram that described the general procedure of the POD algorithm is shown in Figure 8.

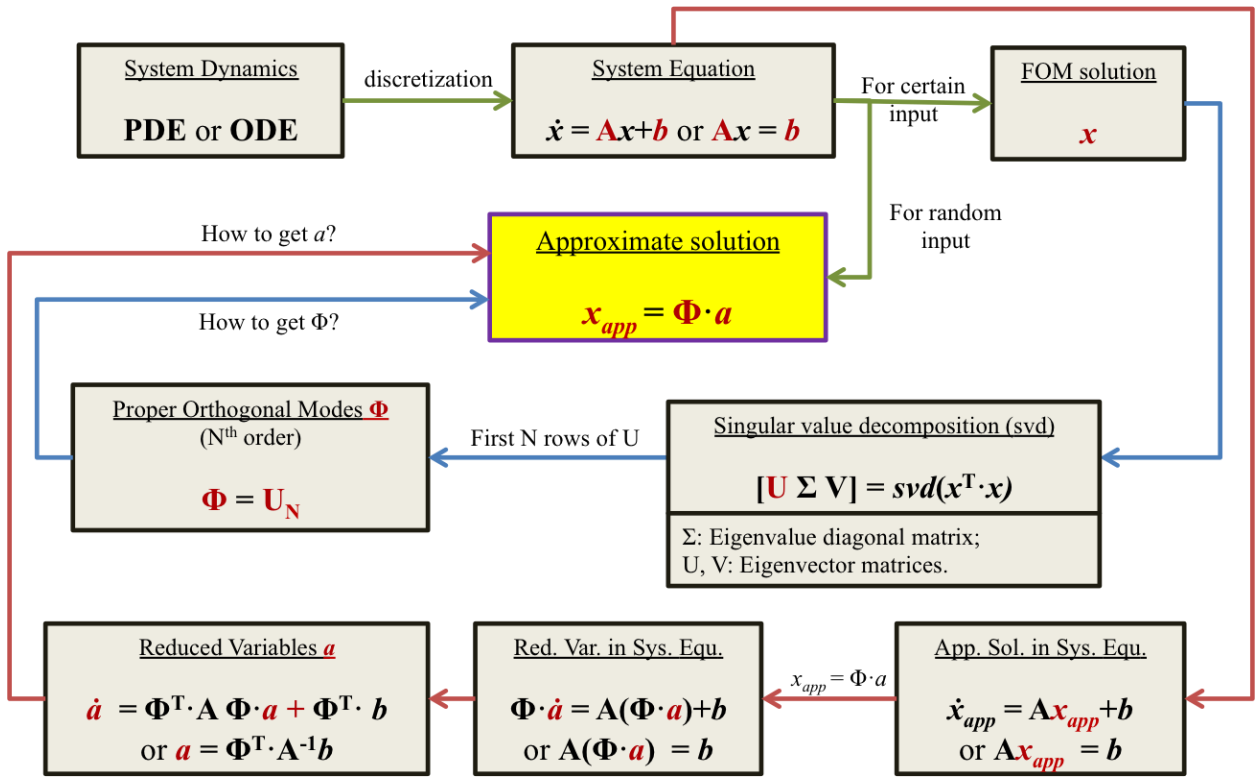


Figure 8: Block diagram of the POD algorithm.

2.3.4 Electrochemical kinetics

Electrochemical reactions that take place at the interface between electrodes and electrolytes are described by the Butler-Volmer equation. The nonlinear functions are linearized based on the fact that the overpotentials vary within a linear range under normal operating conditions [13].

$$j^{Li} = a_s i_0 \frac{(\alpha_a + \alpha_c) F}{RT} \eta \quad (33)$$

2.4 Analysis of the ROM performances

Performances of the sub-models are analyzed by comparing the models before and after reduction. The model before the reduction is numerically solved using the finite difference method (FDM), where the number of grids in the radial direction of particles and thickness direction of the cell are 25 and 15, respectively. The three variables, $C_{s,surf}$, C_e and ϕ are used to evaluate performances of the sub-models.

2.4.1 Order reduction of ion concentration in electrode particles

Since the average concentration in electrode particles, $C_{s,ave}$, is easily obtained by the volume average equation, only the surface concentration, $C_{s,surf}$, is the crucial variable to be considered for the evaluation of performances with respect to frequency, time and static response. The response of $C_{s,surf}$ at a current density, j^{Li} , can be formulated by different methods including parabolic, quartic polynomial, and the Padé approximation. The transfer functions reformulated from a parabolic and a quartic profile are shown in equation (34) [19].

$$\begin{aligned} \frac{C_{s,surf}(s)}{j^{Li}(s)} &= -\frac{15mD_s + R_s^2ms}{5R_s s} \quad \text{parabolic} \\ \frac{C_{s,surf}(s)}{j^{Li}(s)} &= -\frac{3150D_s^2m + 315D_s mR_s^2s + mR_s^4s^2}{35R_s s(R_s^2s + 30D_s)} \quad \text{quartic} \end{aligned} \quad (34)$$

where $m = \frac{1}{a_s F D_s}$

Frequency responses of the analytical exact solution given in equation (17), the two different polynomial approaches and the Padé approximation from the 2nd to 10th order with a step of a two-order for the surface concentration of particles on the anode side are plotted in Figure 9. Comparison between the analytical solution and the two approximation methods shows that the Padé approximation approaches the analytical exact solution up to a certain frequency that depending upon the order. The higher the order is, the smaller the difference of the responses in magnitude and phase. In addition, the range of the response of the 4th order Padé approximation is comparable to that of the quartic polynomial. Conversely, the parabolic polynomial only works over the range of very low frequencies, which means that the dynamic performance is of less satisfactory. The quartic profile with an extra state better represents its response over a high frequency range, but it is hard to extend the order of polynomial systematically to meet the accuracy requirements.

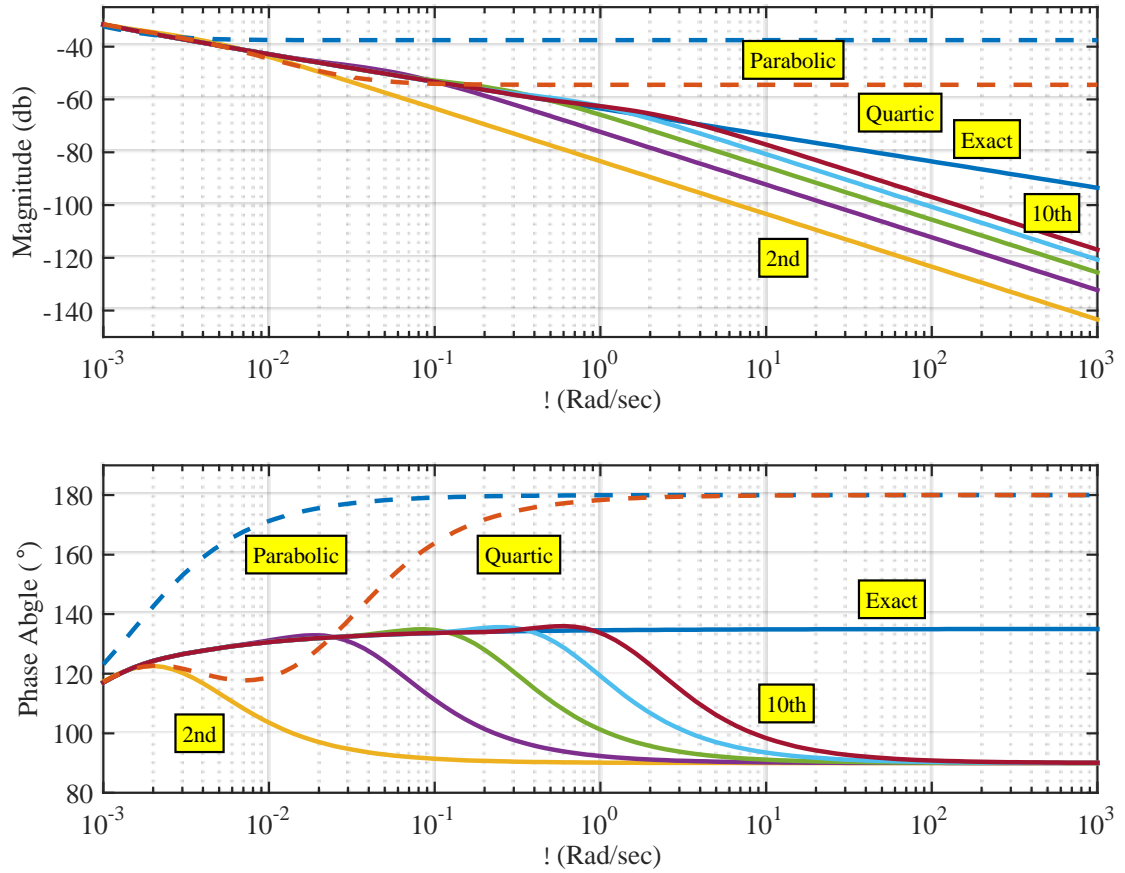


Figure 9: Frequency responses of the surface concentration of a particle on the anode side: analytical exact solution, parabolic and quartic polynomial and the different order of Padé approximation.

Time responses of $C_{s,surf}$ by applying different methods at AC currents are compared in Figure 10. Relative errors are calculated in percentage, which is shown in equation (35), where \hat{y}_i is the simulation data of the different methods, and y_i is the FDM solution with 25 grid points on the radial direction (or experimental data). The parabolic method is not considered because of its large error.

$$\text{Relative error} = \left(\frac{\hat{y}_i - y_i}{y_i} \right) \times 100\% \quad (35)$$

The 2nd order of the Padé approximation (yellow dot-dashed line) shows the largest discrepancy in magnitude and phase compared to the FDM solution. The quartic profile (purple dashed line) shows improved tracking behavior, while the 6th order of the Padé approximation (green line) has the closest match to the FDM solution. The time responses shown in Figure 10 verify the results of the frequency responses as shown in Figure 9 where the Padé approximation can best represent the FDM solution over a wide frequency range if an appropriate order is determined.

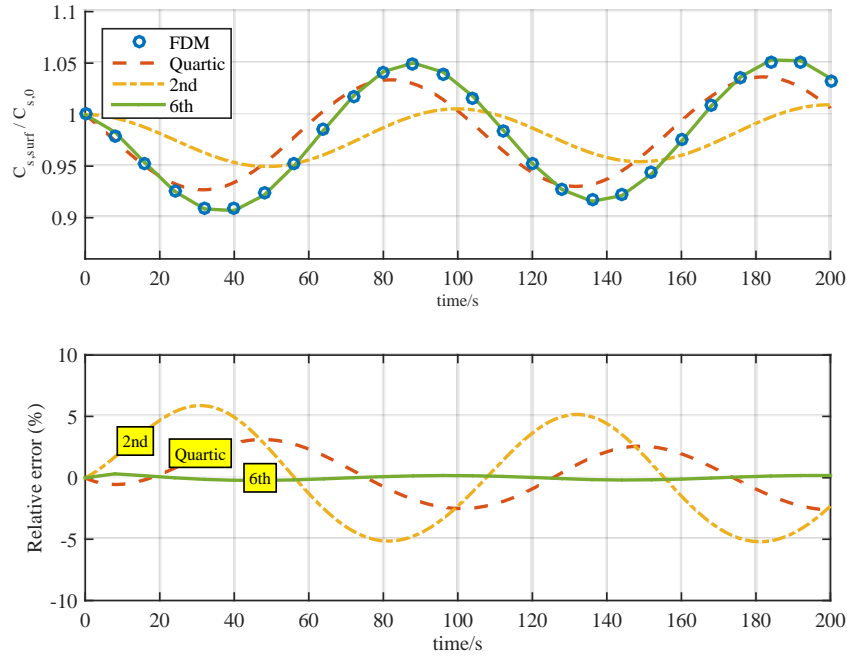


Figure 10: Time responses of surface concentration of a particle on anode: FDM, quartic polynomial, and 2nd and 6th order of the Padé approximation.

One other criterion for assessments is the accuracy of the surface concentration at steady state. According to the analysis in Figure 9, the 3rd order Padé approximation should be enough to represent the steady state or low frequency behavior of variables. Simulation results of the stoichiometry number in the anode side during the discharging process at different C rates are depicted in Figure 11, where the stoichiometry number is a function of surface concentration that is defined as $x = C_{s,surf} / C_{s,max}$ and is used to determine the equilibrium potential in the anode. The results obtained by the 3rd order Padé approximation are compared to those given by FDM (circles), which shows that the 3rd order Padé approximation is accurate enough to replace the FDM method in the steady state. The model order should be determined by balancing the accuracy and the computational time [24].

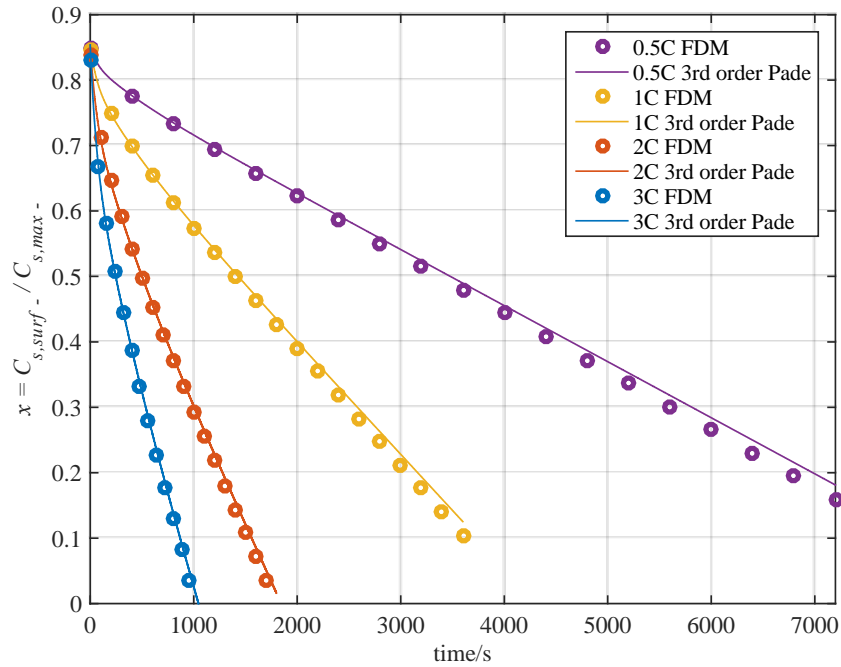


Figure 11: Stoichiometry number of the anode during full discharge: 0.5C, 1C and 2C rate.

2.4.2 Order reduction of ion concentration in electrolyte

The 3rd order of residue grouping (RG) method is employed to replace the FDM method for calculation of ion concentrations in the electrolyte. Distributions of ion concentrations using RG and FDM at various time instants are plotted in Figure 12, where the initial SOC was 90% and the battery is discharged with 1C rate. The x and y coordinates represent dimensionless thickness and ion concentration, respectively. The nominated $C_e/C_{e,0}$ with circles are the concentrations calculated by FDM at each grid point across the cell and those with solid lines are calculated by the 3rd order RG sub-model. With uniform current density applied, the results show that the RG method can follow the response of FDM with a decent accuracy, which can be further improved by appropriately adjusting the upper and lower limits of each eigenvalue group.

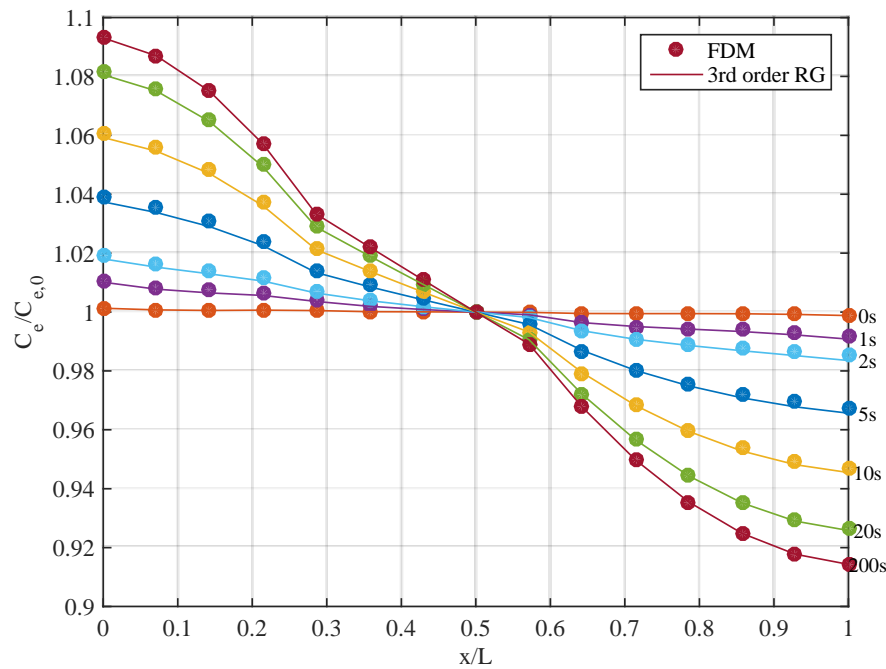


Figure 12: Ion concentration in the electrolyte at various times during 1C discharge.

2.4.3 Order reduction of potentials in electrode and electrolyte

POD is employed to reduce the order for potentials. To determine the order for POD, eigenvalue spectrum of the discrete kernel, $\vec{\kappa} = \vec{\phi}_{full}^T \cdot \vec{\phi}_{full}$, is calculated and plotted in Figure 13, where the eigenvalues, λ_i are the diagonal elements of the matrix Σ in equation (31). The results show that the magnitude rapidly decreases for the first four eigenvalues and then remains a small constant value. Since the importance of the POMs is denoted by the corresponding eigenvalues, the first 4 POMs can represent the most significant dynamic characteristics of the system. As a result, the basis of the POD can be determined by considering the eigenvalue spectrum, and a linear combination of the selected POMs is used to construct a reduced model for potentials in electrode and electrolyte. In this case, a 3rd order sub-model is employed.

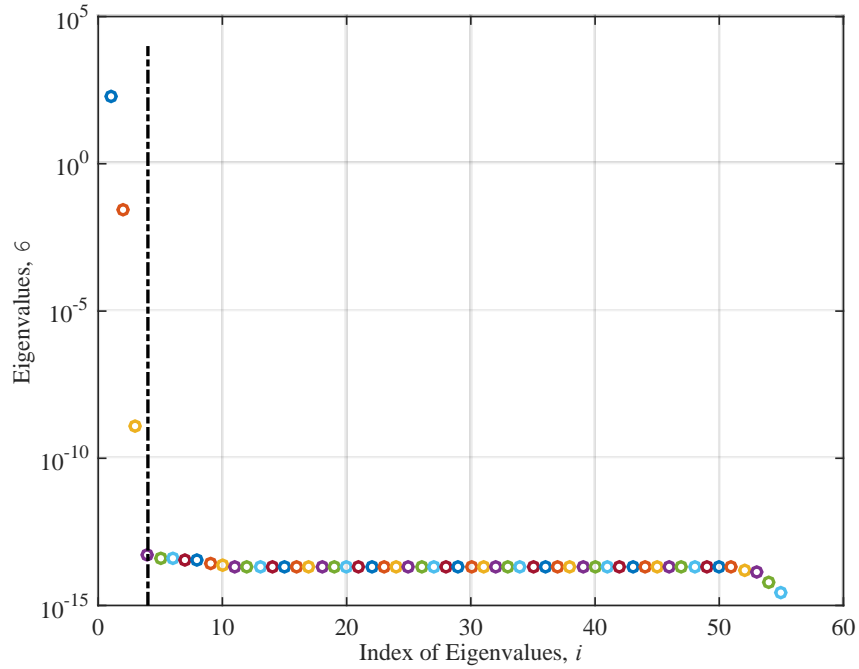


Figure 13: Eigenvalue spectrum of the potential data set obtained from the model with FDM during discharge at 1C rate.

To assess the performance of the 3rd order POD sub-model, potentials in electrode and electrolyte calculated by reduced order sub-models are compared to those of FDM in Figure 14 and Figure 15, where the battery is discharged with 0.5C, 1C, and 2C rate from 100% down to 0% SOC.

Since the data produced by the reduced sub-model and FDM results are hard to compare using a 3D surface plot, only two variables at representative grid points are selected to assess the accuracy of the calculations. Variation of the electrolyte potential in the middle of the cell is shown in Figure 14, where the negative value of potential is caused by the zero potential reference that is set at the anode boundary near the current collector. The electrode potential at the cathode-separator interface point is also given in Figure 15.

The comparison shows that the responses of the 3rd order of POD sub-model (solid curves) are comparable to those of the FDM (circles) that has 15 grid points along the thickness direction including three grid points on the separator. The proposed method allows for substantial reduction of the matrix size of the potential from 27×27 to 3×3 , so that the computational time can be significantly reduced while maintaining the accuracy.

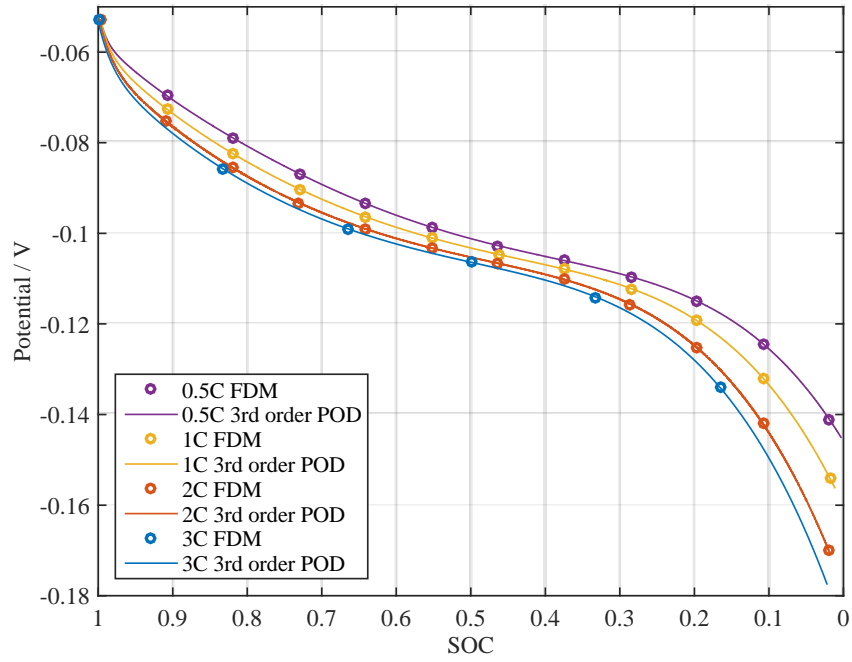


Figure 14: Electrolyte potential in the center of the cell during discharging with 1C rate.

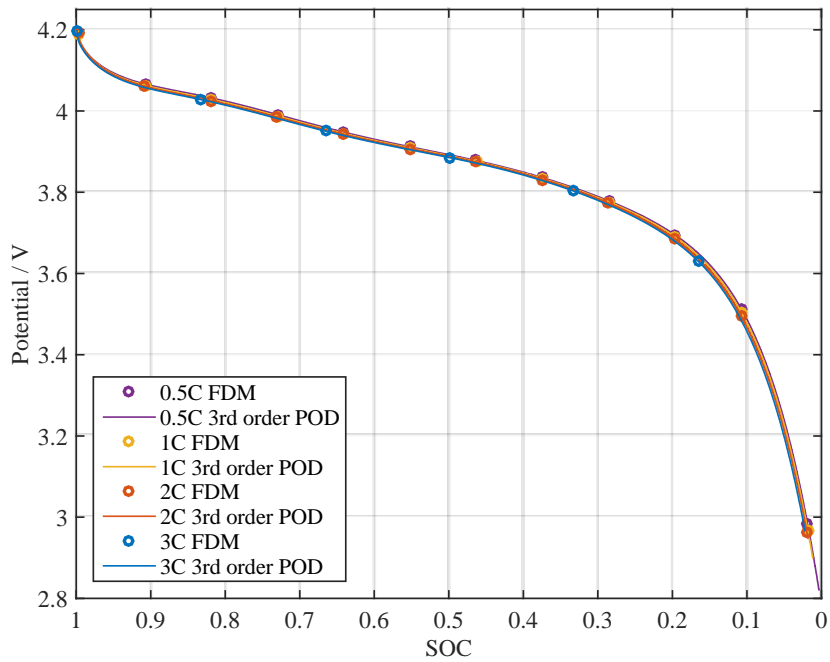


Figure 15: Electrode potential at the interface between the separator and composite cathode during discharge with 1C rate.

2.4.4 ROM for a single cell

ROM for a single cell is constructed by the sub-models. A schematic diagram for the integrated ROM is shown in Figure 16, where input variables are load profiles along with ambient temperature that can be constant current (CC) or constant voltage (CV) charging and discharging. The data set for potential ϕ is calculated offline using FDM and then stored for POD. Parameters used for these specific cells are listed in the appendix. Order for sub-models is defined as an extra input parameter that can be determined upon required accuracy. System matrices for each sub-model are determined based on parameters, initial and boundary conditions, and stored prior to the main loop.

The main loop consists of three sub-models. Ion concentrations are firstly solved with uniform current density, the resulting state variables $C_{s,surf}$, $C_{s,ave}$, and C_e are used to determine the equilibrium potential, SOC and diffusion term in charge conservation equations correspondingly. Then the potentials are calculated based on the ion concentrations at the instants.

The output variables are terminal voltage or current, ion concentrations, SOC and other internal variables.

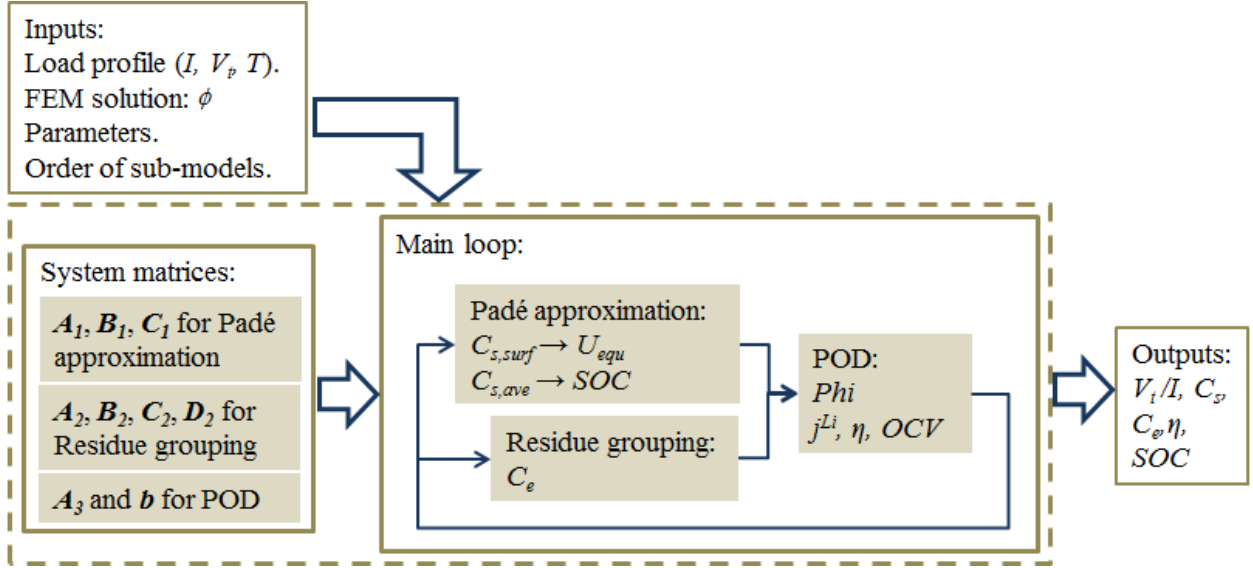


Figure 16: Schematic diagram for the ROM for a single cell.

2.4.5 Effects of sampling time

Sampling time is one of the crucial factors for the determination of hardware. A short sampling time can overload hardware and increase its overall costs, particularly when a large number of cells are connected in series and parallel. Therefore, computational time and error of terminal voltage are calculated as a function of sampling times and plotted in Figure 17, where the initial SOC of the battery was 100% and the battery was discharged at 1C rate. The model is coded with MATLAB and runs on PC with 3.4 GHz processor, whereas execution time is measured. The errors are normalized as below, where \hat{y}_i and y_i are the data obtained from simulations and experiments and n is the number of sampling points.

$$\text{Normalized error} = \sqrt{\frac{\sum (\hat{y}_i - y_i)^2}{n}} \quad (36)$$

The blue line with triangles and green line with circles denote the computational time and errors, respectively. As expected, the errors are reciprocally proportional to the computational time. An optimal sampling time can be determined by considering time and accuracy. We chose about 1 second as the optimal sampling time, where the curves cross.

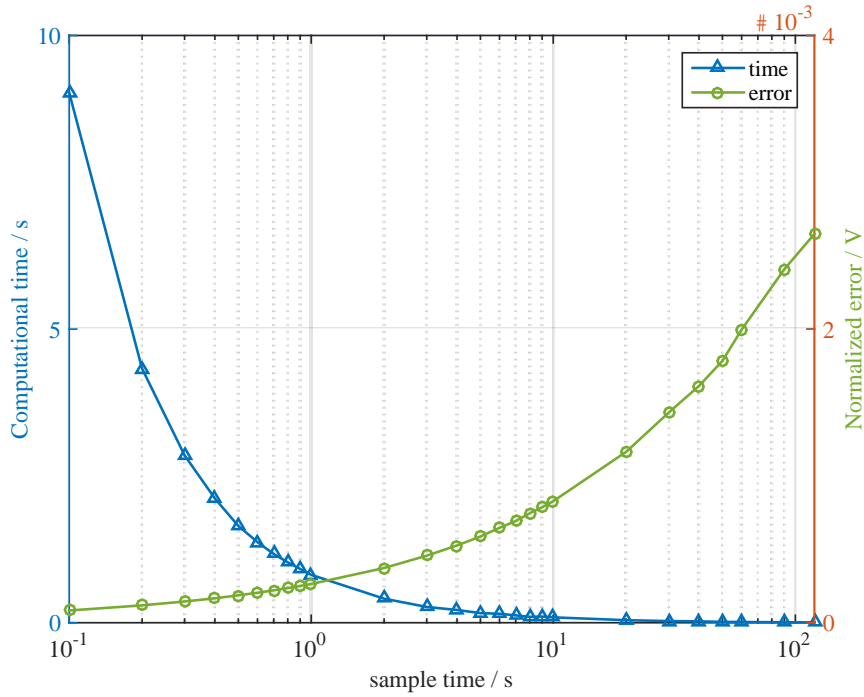


Figure 17: Computational time and error with respect to different sample rate.

2.5 Experimental validation of the ROM

The constructed ROM is validated against experimental data collected from a test station that was constructed with a programmable power supply and an electronics load that is controlled by

LabVIEW. The cells used for this validation are pouch type lithium polymer batteries, whose specifications are listed below.

Chemistry: Cathode, LiMn_2O_4 (spinel); Anode, surface modified graphite; Electrolyte, Gel polymer ($\text{LiPF}_6+\text{EC}/\text{DEC}/\text{EMC}$); Separator, Ceramic coated separator.

Dimension: $14.7\text{mm}\times 280\text{mm}\times 185\text{mm}$.

Nominal capacity: 50 Ah.

Operation range of the terminal voltage: 2.7V - 4.2V.

The experimental data are acquired under constant temperature at 25°C by using an extra thermal chamber and with different current loads that include full charge and full discharge with constant current at 0.5, 1, 2C rate, continuously charging and discharging multiple cycles and a current profile obtained from a driving cycles of an electric vehicle.

2.5.1 Discharging and charging

The terminal voltage V_t between simulation results of ROM (solid line) and experimental data (circles) are plotted in Figure 18 and Figure 19, where the simulation results of ROM have a fairly good match with the experimental data at different current rates.

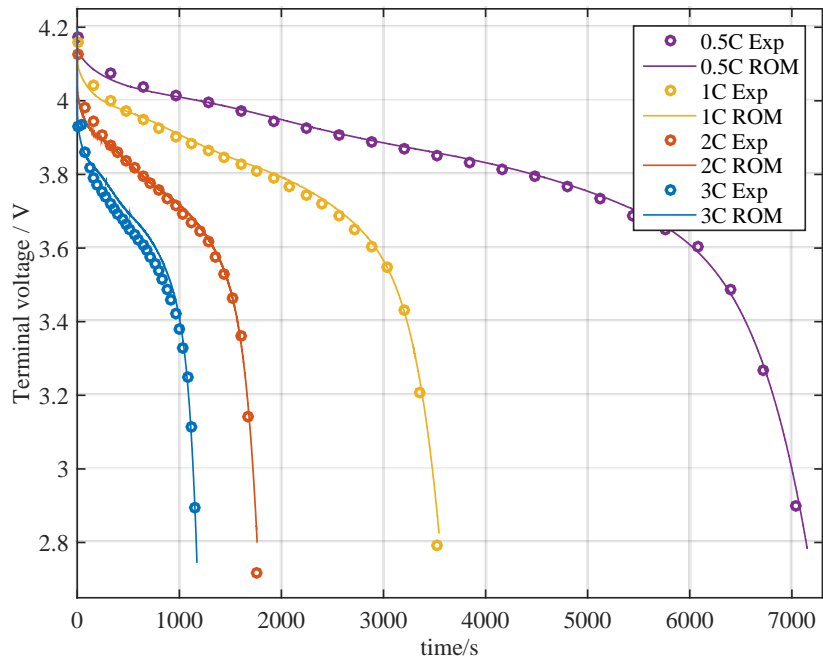


Figure 18: Comparison of terminal voltage between simulations and experiments during 0.5C, 1C, 2C and 3C discharge.

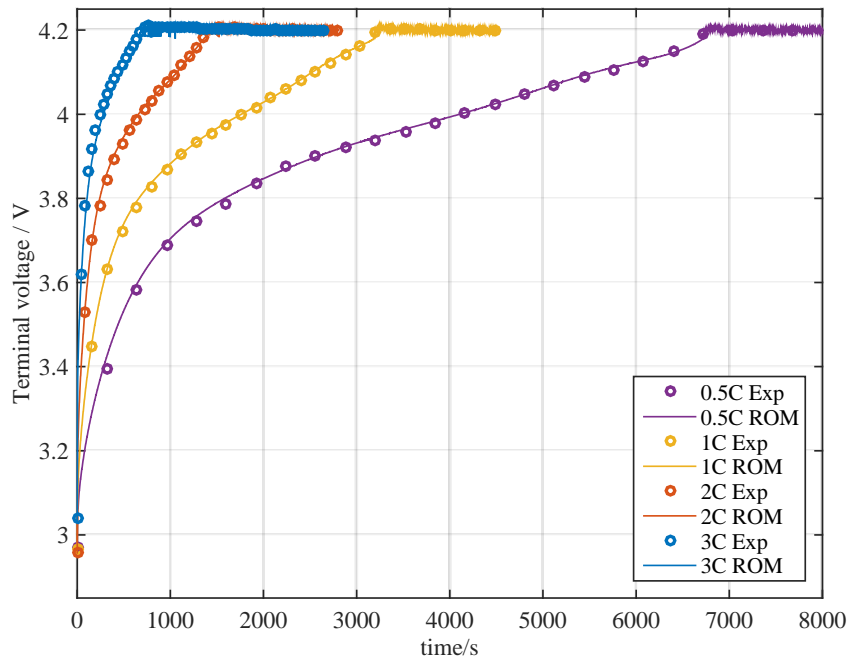


Figure 19: Comparison of terminal voltage between simulations and experiments during 0.5C, 1C, 2C and 3C charge.

The percentage of relative errors defined in equation (35) during discharging and charging are plotted in Figure 20. Overall errors are less than 2% except at the end of charging and the beginning of discharging where the SOC is relatively low. The error is caused by the simplified equation for the overpotential since the terminal voltage is the difference between the OCV and the overpotential that becomes large at low SOC range.

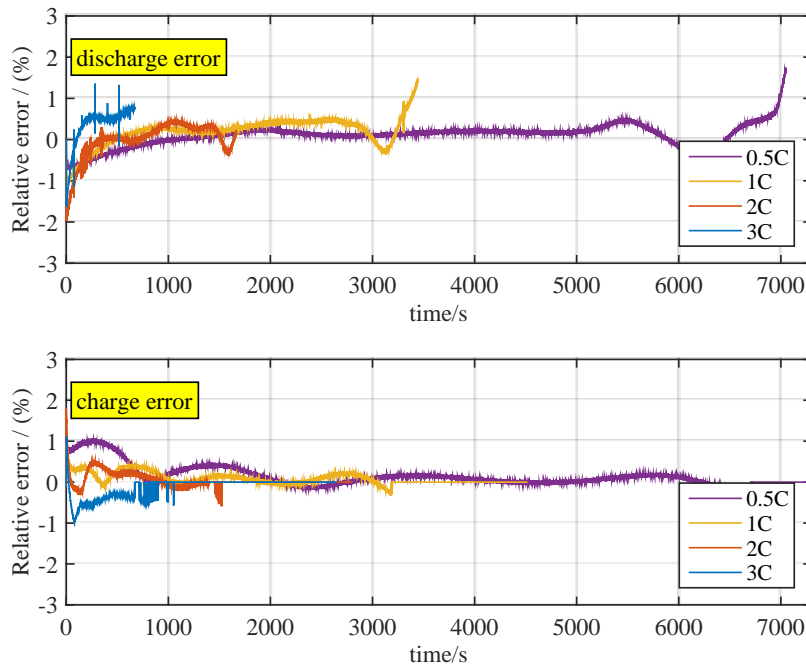


Figure 20: Percentage errors of the terminal voltage at discharge and charge.

SOC between simulation results of ROM (solid line) and experimental data (circles) are plotted in Figure 21 and Figure 22, where the simulation results of ROM have a fairly good match with the experimental data at different current rates.

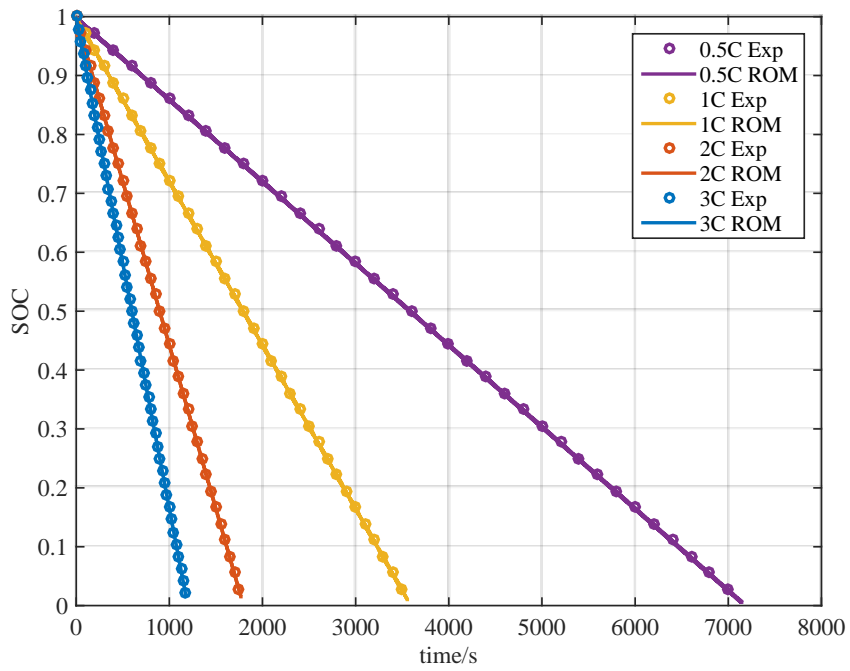


Figure 21: Comparison of SOC between simulation and experiments during 0.5C, 1C, 2C and 3C discharge.

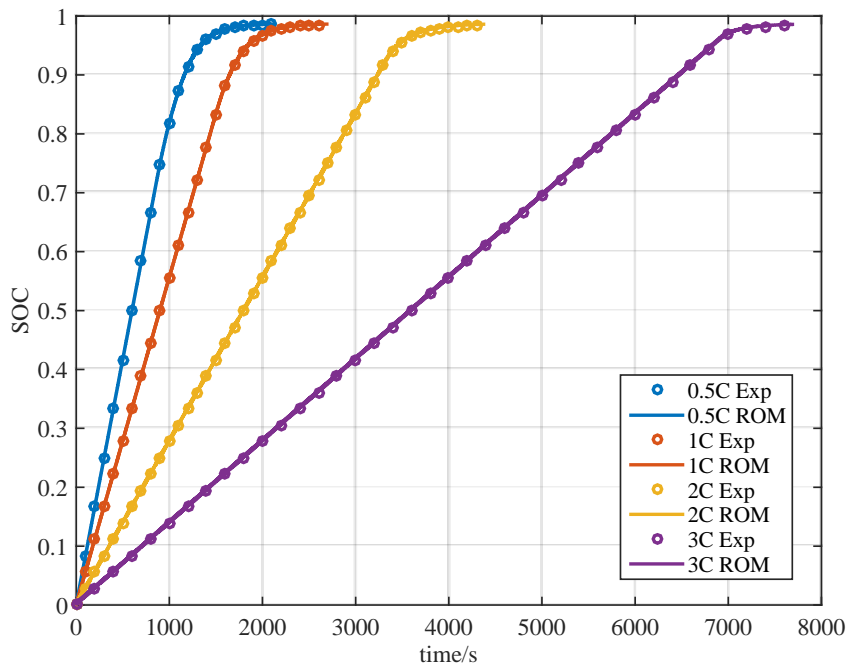


Figure 22: Comparison of SOC from simulation and experiments during 0.5C, 1C, 2C and 3C charge.

Lumped surface temperature between simulation results of ROM (solid line) and experimental data (dots) are plotted in Figure 23 and Figure 24, where the simulation results of ROM match the experimental data with some discrepancy. The error is mainly caused by an inaccurate estimation of heat sources.

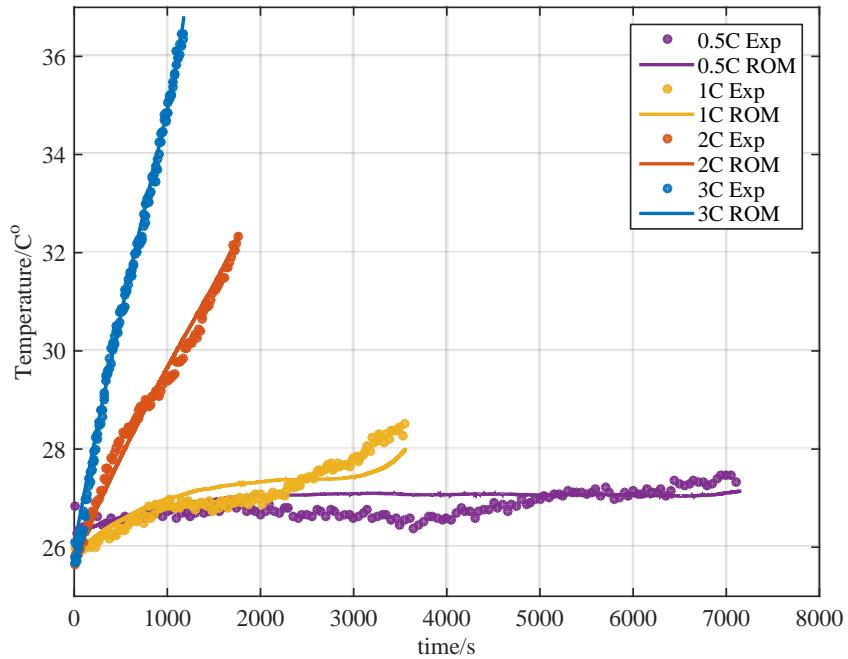


Figure 23: Comparison of surface temperature between simulation and experiments during 0.5C, 1C, 2C and 3C discharge.

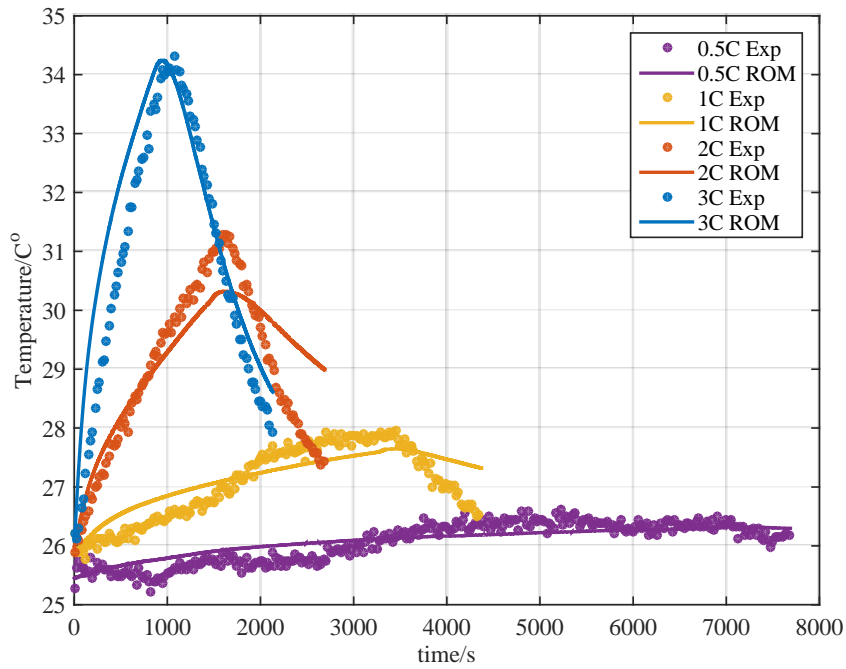


Figure 24: Comparison of surface temperature between simulation and experiments during 0.5C, 1C, 2C and 3C charge.

2.5.2 Multiple cycles and EV driving cycles

Long-term stability of the ROM is assessed by the response of terminal voltage at multiple cycles and an EV driving cycle. The multiple cycles consist of a combination of CC/CV charging and CC discharging with various current amplitudes. Simulation results of the ROM are compared to the experimental data in Figure 25 and Figure 26. There are some transient errors appeared at the instant when an abrupt current change occurs, which is caused by inaccurate determination of equilibrium potential that is a function of surface concentration as shown in equation (12). In fact, the surface concentration in electrode particle is estimated by 3rd order Padé approximation, which is accurate enough to represent the static responses as shown in

Figure 11, but is inadequate to capture the high frequency dynamics presented in driving cycles. Since the order of the Padé approximation is systematically adjustable unlike the polynomial approach, the accuracy of ROM can be further improved by increasing the order of the approximation, which leads to high computational expense.

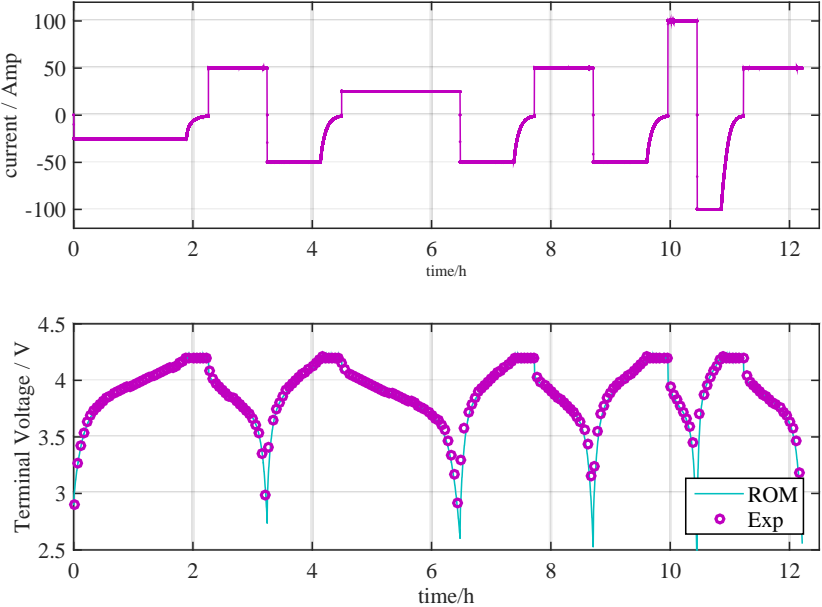


Figure 25: Comparison of terminal voltage between simulation and experiments at multiple charging and discharging cycles.

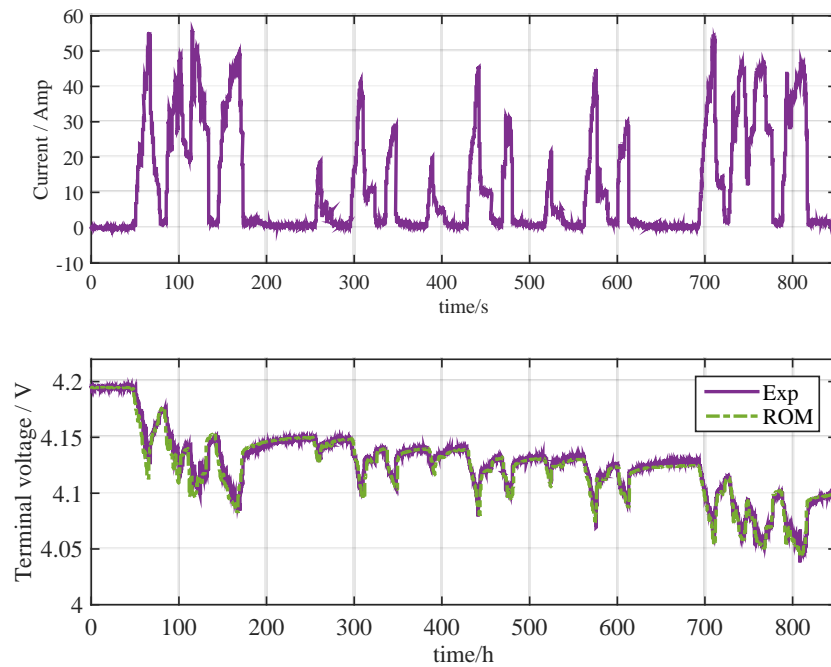


Figure 26: Comparison of terminal voltage between simulation and experiments at a current profile measured at an EV driving cycle.

2.5.3 Comparison with the previous ROM

Two major features of the newly developed ROM are compared with those of the previously developed ROM, which include computational time and normalized voltage errors as a function of the sampling time, as plotted in Figure 27. The computational time is significantly reduced for the sampling time that is less than 1 sec while the errors of terminal voltage are almost the same until 70sec, but are less after 70sec.

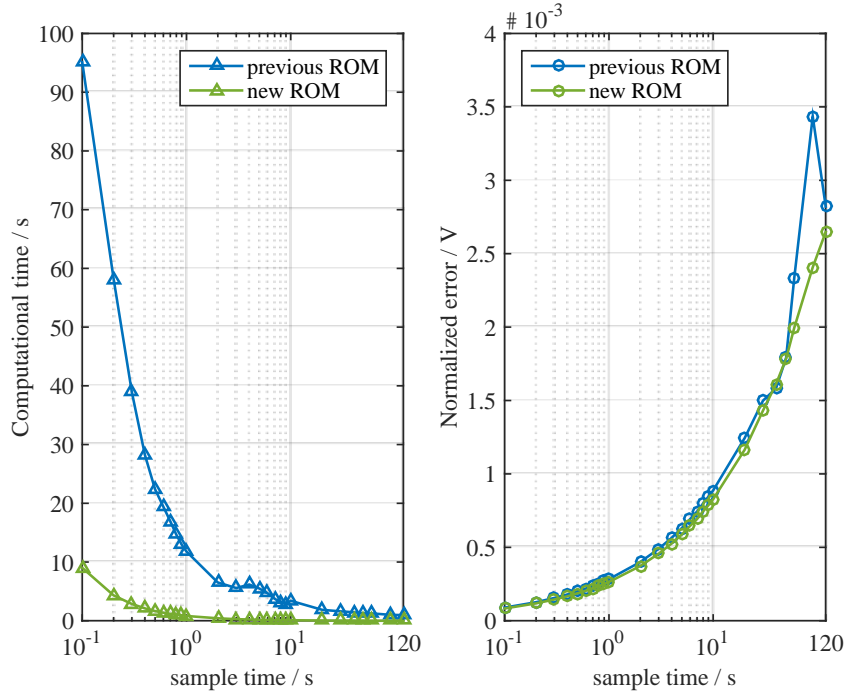


Figure 27: Comparison of computational time and error vs. sample time between the previous ROM [24] and the new proposing ROM.

Finally, the execution time of three models including the time required for calculation of sub-models is listed in Table 3. The ROM proposed in this paper needs the shortest time and reduces the computation time to one tenth of the previous ROM.

Table 3: Comparison of computational time (second) among FOM, previous ROM, and the new approach.

	FOM	Previous ROM [24]	New ROM
Total	50.74	10.09	1.05
C_s	19.25	6.05	0.08
C_e	1.93	0.05	0.03

<i>Phi</i>	7.01	3.36	0.34
Others	22.55	0.63	0.6

2.6 Summary of the ROM

Electric equivalent circuit models have been widely used for algorithms that embedded in BMS, but have limitations because of the absence of the physical phenomena that take place in batteries. Particularly, temperature dependence and degradation mechanisms are not captured in the models, which play a key role in designing the algorithms. ROM based on electrochemical principles can provide a potential solution that allows for monitoring internal physical variables. As a result, advanced control algorithms can be designed based on these variables. In fact, hundreds of cells are needed for high power systems, where the computational time of the model is one of the impeding factors for implementations on microcontrollers.

This paper addresses the optimization of a ROM that is constructed by integration of sub-models derived using different order reduction techniques. The diffusion in solid is simplified by Padé approximation, while the concentration in the electrolyte is reduced by applying the residue grouping method. In addition, POD is adopted to shrink the matrix size for potentials. The integrated ROM is then validated against experimental data at various operating conditions. Main accomplishments and findings are summarized as follows:

- Comparative analysis of the performances of the individual reduced sub-models in time and frequency domain,
- Selection of sampling time based on errors,

- Performance of the developed ROM
 - Reduction of computational time to one-tenth of the previous ROM while the accuracy remains the same or better than the previous ROM regardless of the sampling time.
 - The order is adjustable dependent upon input profiles or accuracy requirements.

Chapter 3 Experimental investigation and parameter identification

3.1 Experimental setup

The pouch type single cell being investigated for this study has a chemistry of LMO/Carbon for the electrodes. The single cell has a dimension of 280mm×185mm×14.9mm with a 50Ah capacity. The tests were conducted at four ambient temperatures: 60°C, 40°C, 25°C and 0°C. At each temperature, cells were charged and discharged with 4C (2C for 0°C) rate in order to accelerate degradation process and the number of cycles was up to 600. In each cycle, the cell was charged with a constant current (CC) up to 4.2V followed by a constant voltage (CV) charge until the SOC reaches to 95% or 75% and then discharged with a constant current until the SOC became 25% or 5%. After every 30 cycles, a 0.2C charge-discharge profile was applied to the cell to measure its capacity. For every 30 or 60 cycles, the battery was discharged to 50% SOC for EIS measurement at 25°C. After all the aging cycling, the batteries will be sent to the material lab to conduct the material analysis. The test matrix for the aging cycling is shown in Table 4.

Table 4: Test matrix.

Temperature	SOC range	Cycle C-rate	Q_{max}	EIS	End of cycle	Material Analysis
60°C	25% - 95%	4C - 200A	Every 30 cycles 0.2C – 10A	30×(1,2,3,4,5,6)th cycles;	600 cycles or 20% capacity fade.	XRD, SEM, EDS.
40°C	25% - 95%			60×(4,5,6)th cycles;		
25°C	25% - 95%			120×(4,5)th cycles;		
	5% - 75%			@50%SOC;		
0°C	25% - 95%	2C – 100A	@25°C.			

A test station to conduct experiments was designed, constructed and calibrated. A schematic diagram of the test station is shown in Figure 28, where a programmable power supply and a programmable electronic load were used to generate a charging and discharging profile that was controlled by LabVIEW. Current is measured by a high resolution current transducer. Terminal voltage is measured directly from the cell tabs. Temperatures of the cell are measured by three thermal couples that attached on the surface of the cell that near the anode tab, cathode tab and in the middle of the cell. The ambient temperature is measured by another thermal couple that placed in the thermal chamber. All the measurement data are collected by LabVIEW and used for aging analysis and model validation. Tests were conducted in a thermal chamber where the ambient temperature was controlled from 0°C to 60°C.

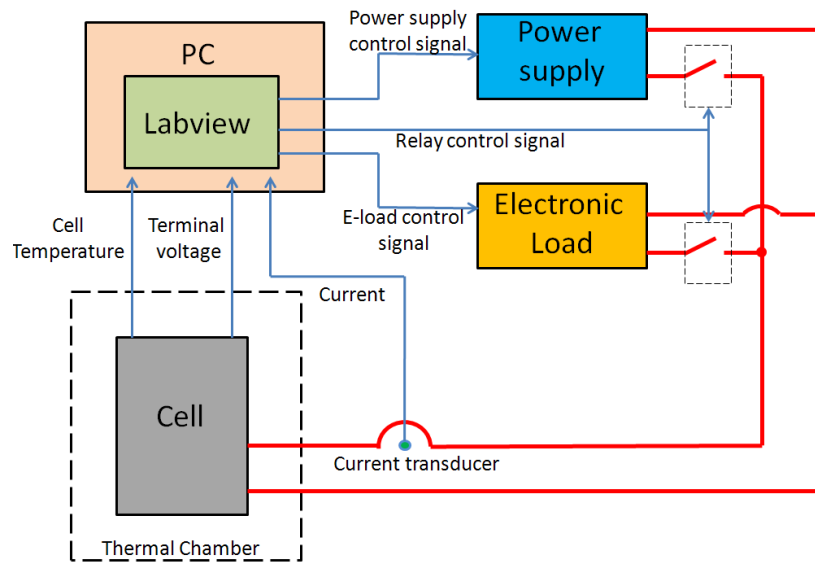


Figure 28: Schematic diagram of a test station.

3.2 Analysis of aging cycling data

A snapshot of aging cycling profile that includes current, voltage and temperatures are plotted in Figure 29. It is shown that the cell is cycled between 4.2V (95% SOC) and 3.45V (25% SOC) with a constant current of 200A. The cell temperature is varying at different stage of the cycling and the ambient temperature is controlled at 25°C.

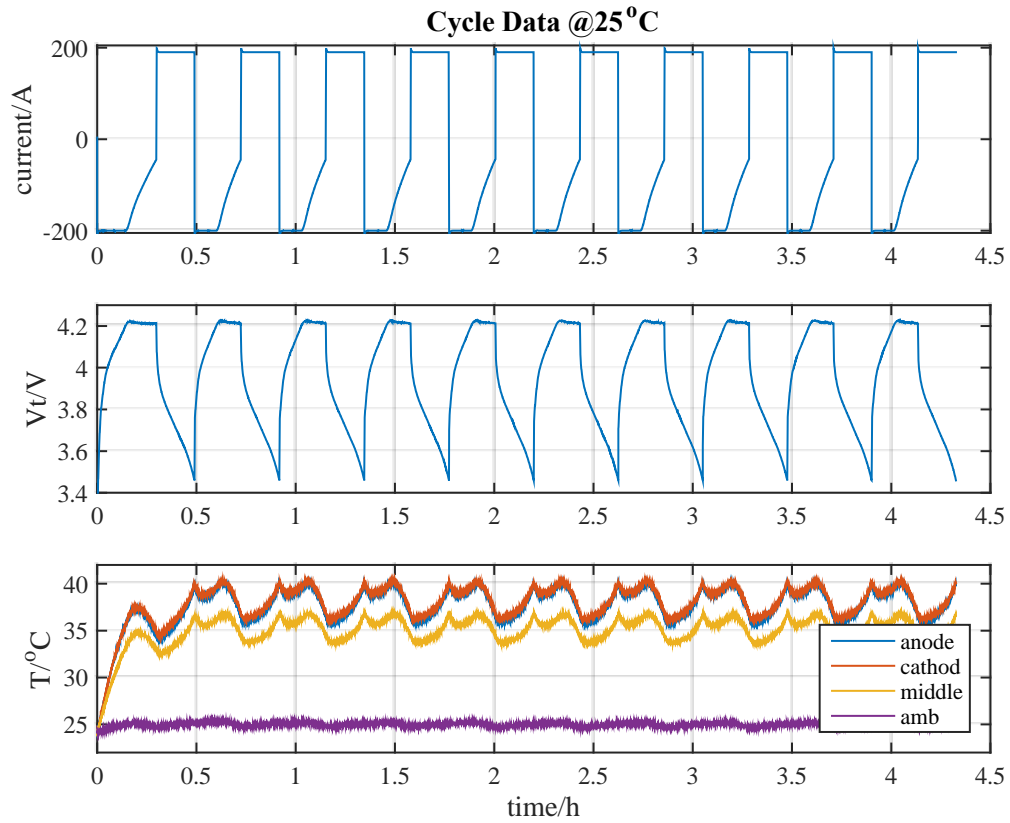


Figure 29: Cycle data with 4C current rate at 25°C.

The discharge curves for capacity measurement at different temperatures are shown from Figure 30 to Figure 34. The discharge curves for the fresh cells are shown in dark blue at the right side of the plots. With cycle number increased, the cells are degraded in different degree, which is indicated by the decreasing of deliverable voltage and capacity. This phenomenon is

reflected by the discharge curve switching from the right blue ones to the left yellow ones. By comparing Figure 30, Figure 31 and Figure 32, it is shown that the elevated temperature has a great impact on accelerating the degradation. As one of the reactants of side reaction, the electrolyte solvent molecule is inadequate due to lower permeability of SEI layer. At higher temperature range, the diffusivity of electrolyte solvent molecules increases, which results in larger side reaction rate in the cell. Therefore, accumulation of side reaction products, along with consumption of lithium ions and electrolytes, is more aggressively, which leads to severe degradation.

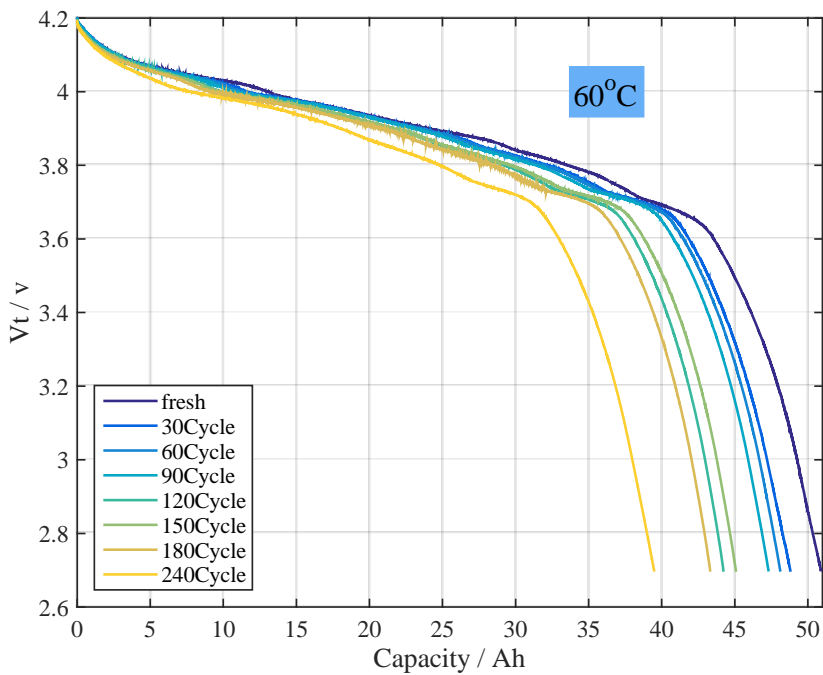


Figure 30: 0.2C discharge curves for Qmax measurement at 60°C.

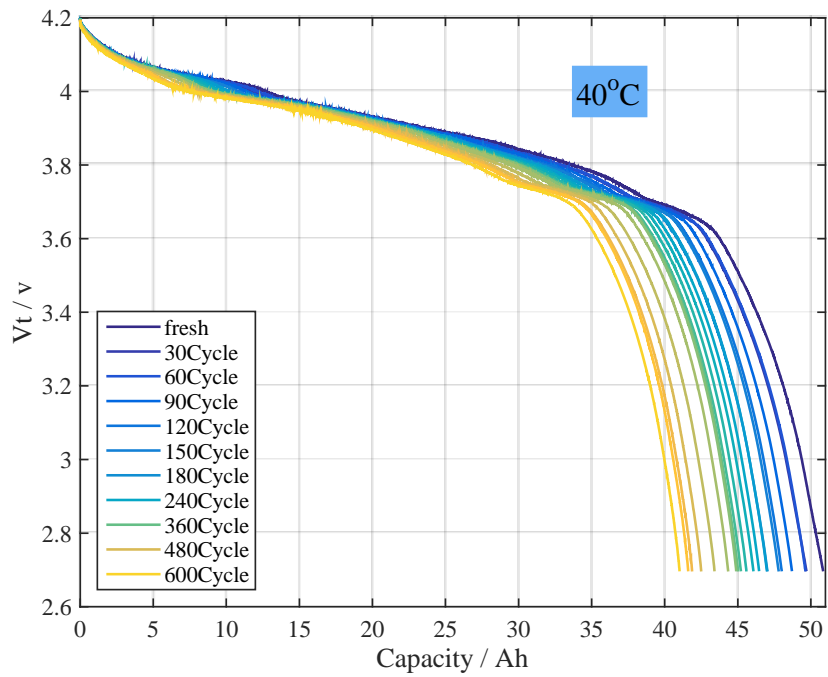


Figure 31: 0.2C discharge curves for Qmax measurement at 40°C.

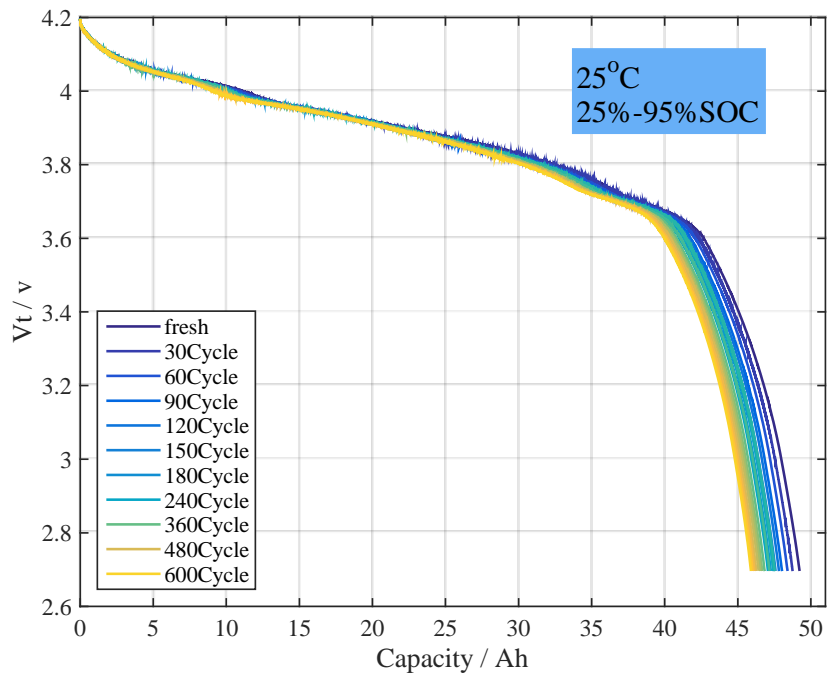


Figure 32: 0.2C discharge curves for Qmax measurement at 25°C- high SOC range.

By comparing Figure 32 and Figure 33, it is shown that the cell cycled at higher SOC range has slightly more degradation than the one cycled at lower SOC range, which means the cycling SOC has a small impact on battery degradation. At higher SOC, the lithium ion concentration at anode is higher than that at lower SOC, which provides more reactants to the main reaction as well as the side reaction. However, the lithium ion is abundant compared to the electrolyte solvent molecule that is another reactant of the side reaction, which explains the minor impact of cycling SOC on cell degradation.

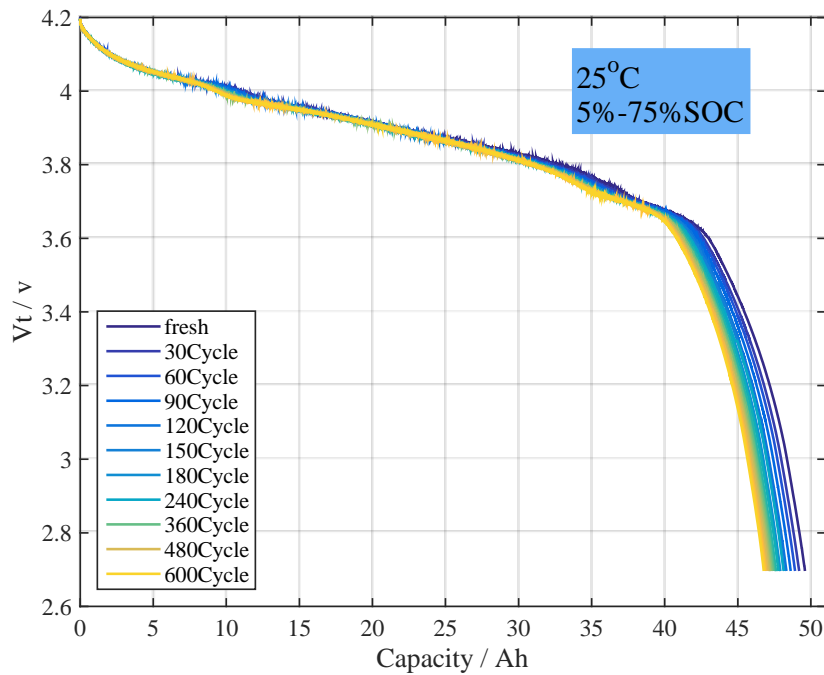


Figure 33: 0.2C discharge curves for Qmax measurement at 25°C- low SOC range.

By comparing Figure 32 and Figure 34, it is shown that the deliverable voltage and capacity are lower at low temperature range compared to that at room temperature. In addition, there is more degradation detected at lower temperature range. Due to the larger internal resistance at a lower temperature range, the ohmic overpotential, as well as the heat dissipation inside of the

battery, is higher than that at room temperature range. Accordingly, the cell performance is decreased and the degradation is worsened.

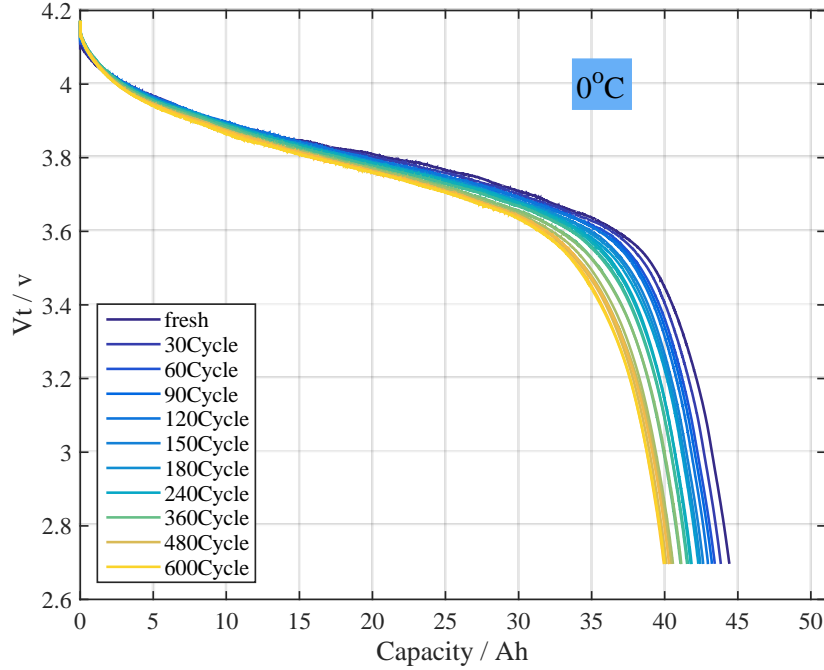


Figure 34: 0.2C discharge curves for Qmax measurement at 0°C.

To compare capacity fade at different temperatures, a dimensionless relative capacity is introduced and defined as the capacity percentage of the aged cell over that of the fresh cell:

$$Q_{rel} = \frac{Q_{aged}}{Q_{fresh}} \cdot 100\% \quad (37)$$

The dimensionless relative capacity with respect to prolonged cycles at different temperatures is plotted in Figure 35. As discussed before, the cells cycled at extreme operating conditions, such as high temperature, low temperature, and high SOC range, show more degradation. However, the cycling temperature has greater effects on cell degradation compared to the effects of SOC range. Moreover, elevated temperature causes larger capacity fade than

lower temperature, which reveals that the amount of electrolyte solvent molecules participated in the side reaction has the major effect on cell degradation.

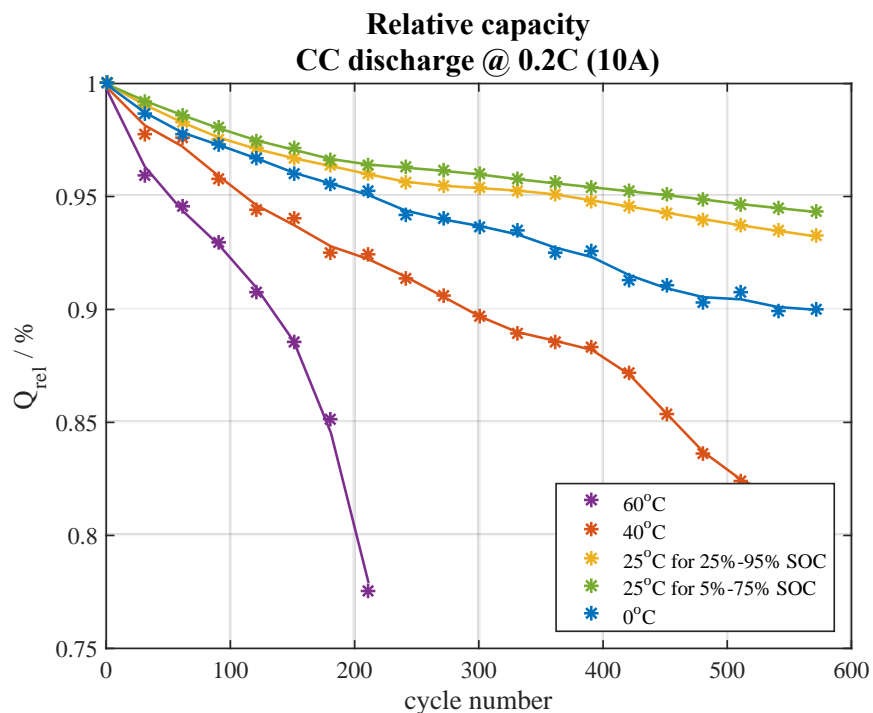


Figure 35: Capacity measurement for every 30 cycles at different temperatures.

3.3 Analysis of EIS data

The impedance characteristics of cycled cells measured by EIS at different temperatures are plotted as dots from Figure 36 to Figure 40. The EIS is composed of a complete semicircle followed by a less obvious semicircle and a line with increasing slope at low frequency end. With the cycle number increased, the EIS shift from left to the right side with an increased radius of the first semicircle. However, the change of impedance with respect to cycling number and temperature is not explicit, which triggered the requirement of applying a model that can extract

the electrochemical information by fitting the EIS data to it. The model parameters can be used for impedance analysis explicitly.

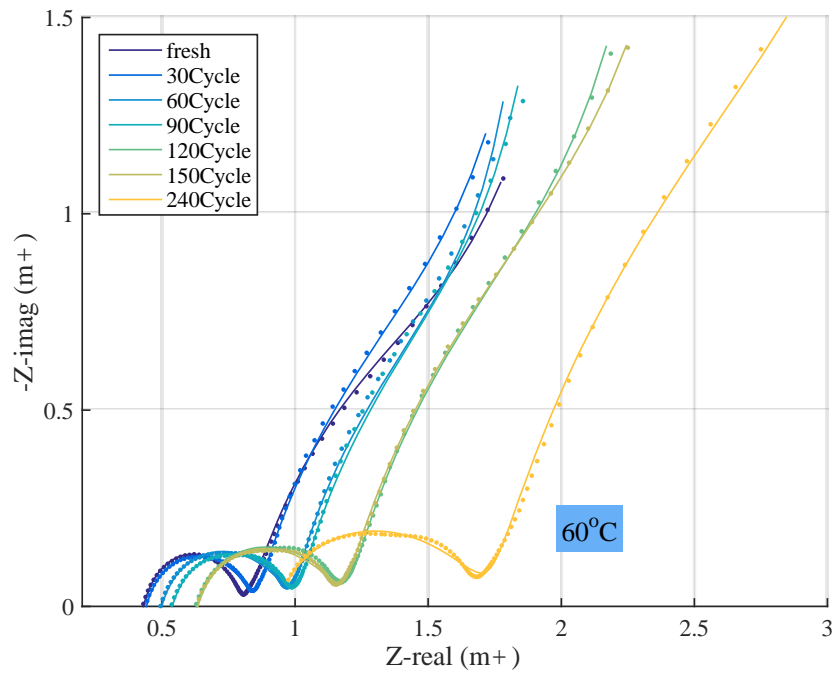


Figure 36: EIS measurement vs. model fitted data at 60°C.

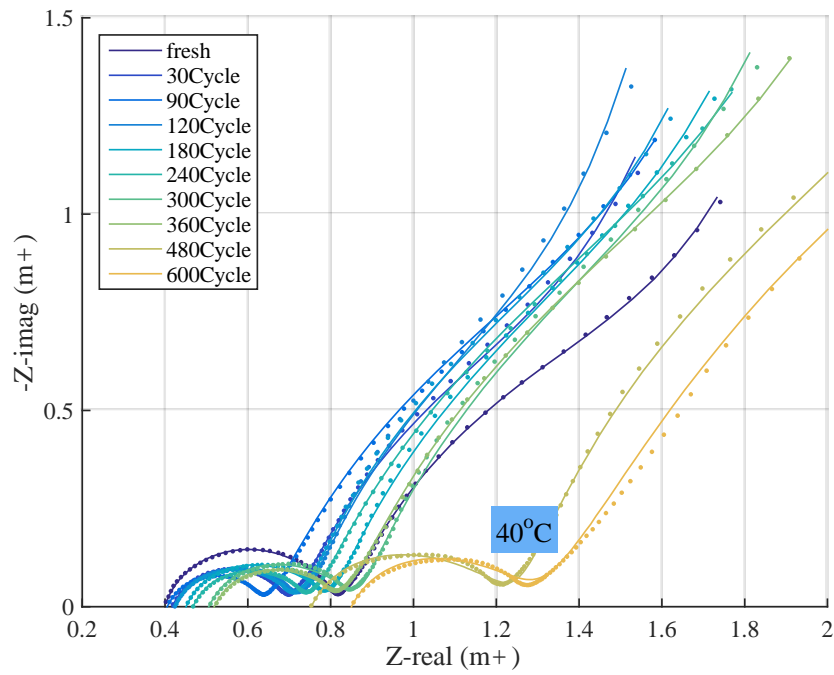


Figure 37: EIS measurement vs. model fitted data at 40°C.

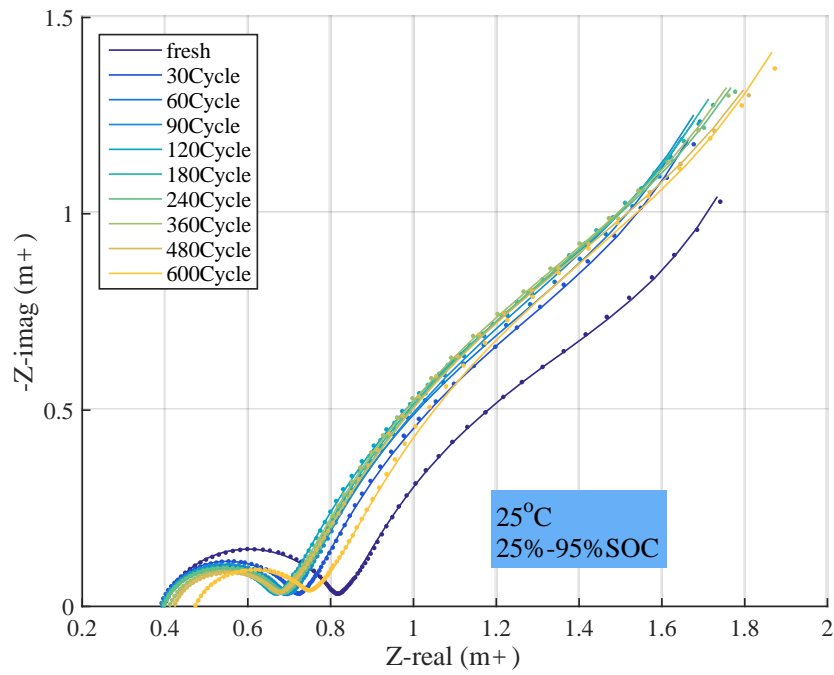


Figure 38: EIS measurement vs. model fitted data at 25°C - high SOC.

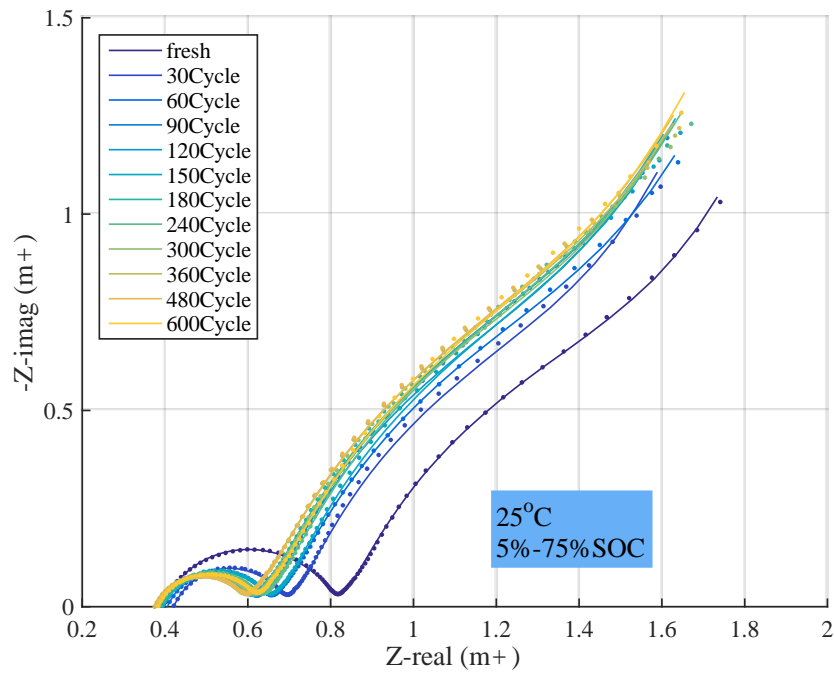


Figure 39: EIS measurement vs. model fitted data at 25°C - low SOC.

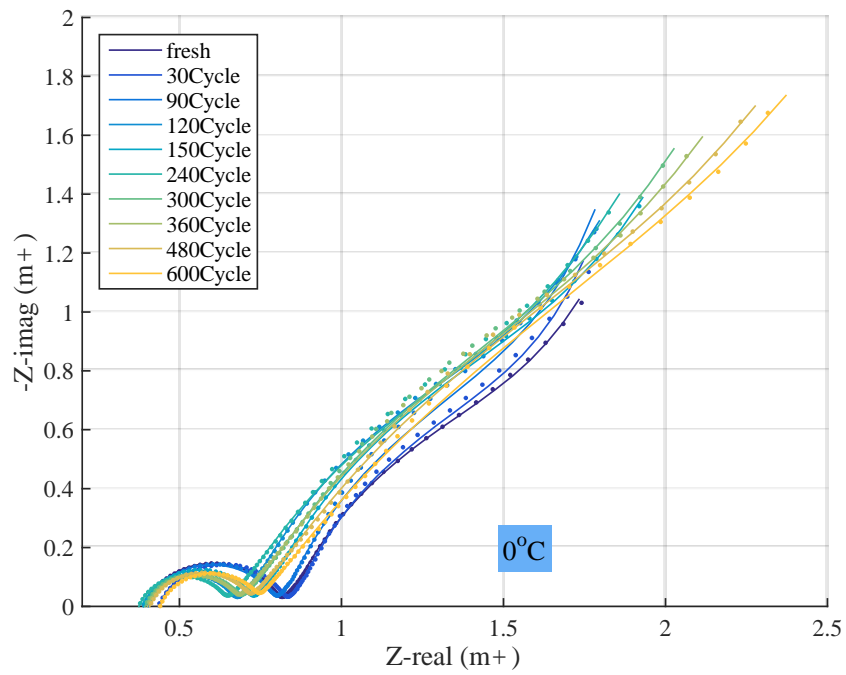


Figure 40: EIS measurement vs. model fitted data at 0°C.

The EIS can be fitted by an equivalent circuit model (ECM) and its configuration is shown in Figure 41, which is similar to the models reported in the literatures [25][26][27][27]. The mutual inductance of external wires in high frequency domain ($>1\text{kHz}$) is represented as L in the model [25][26]. R_0 is the bulk ohmic resistance of the cell, which reflects a combined resistance of the electrolyte, separator, and electrodes. It equals to the left intercept of EIS curve on the x-axis at high frequency ($\approx 1\text{kHz}$) [26][27][27]. R_{SEI} and C_{SEI} indicate resistance and capacitance of the SEI at the anode, which corresponds to the first semicircle at high frequencies from 1kHz to several Hz [25][26][27][27]. R_{ct} and C_{ct} are charge transfer resistance and its relative double layer capacitance, which correspond to the second semicircle at medium frequencies from several Hz to several MHz [26][27]. W is the Warburg impedance related to the diffusion of lithium ions on the electrode-electrolyte interfaces, which corresponds to the sloping line at low frequency end. The combination of charge transfer impedance and Warburg impedance is called Faradic impedance, which reflects kinetics of the cell reactions [29]. C_{int} is the intercalation capacitance that represents the process of ion intercalation. To extract the model parameters, the ECM is fitted to the impedance spectrum measured by EIS using nonlinear curve fitting algorithm. The simulation results are shown as solid lines in Figure 36-Figure 40. The fitting results show a fairly good match to the experimental measurements.

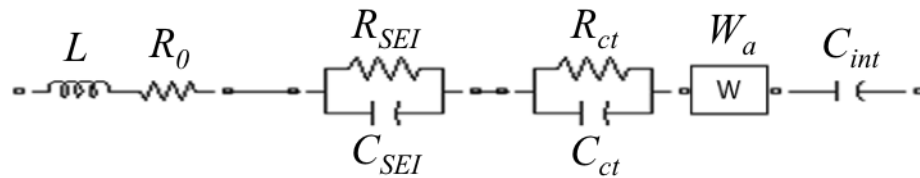


Figure 41: EIS equivalent circuit model.

Two parameters that reflect the cell degradation are the bulk ohmic resistance R_0 and SEI resistance R_{SEI} . They are extracted from the ECM and plotted with respect to cycle number and temperature in Figure 42 and Figure 43. The solid markers are the mean value and the bars are the standard deviation.

The bulk ohmic resistance R_0 increases with prolonged cycles, especially at high temperatures and high SOC range. The change of R_0 verifies the capacity fade observation in the previous section.

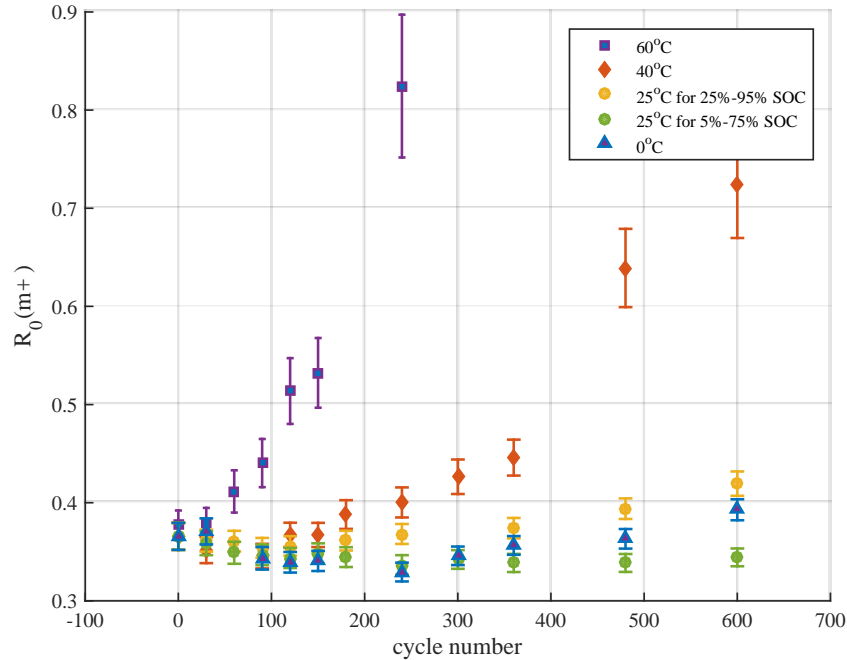


Figure 42: Model fitted parameter - R_0 .

The SEI resistance R_{SEI} has the similar trend as the Ohmic resistance R_0 . At 60°C and 40°C, the SEI resistance increases to three times and twice larger than that of the fresh cell. At 25°C and 0°C, the change of SEI resistance is relatively small.

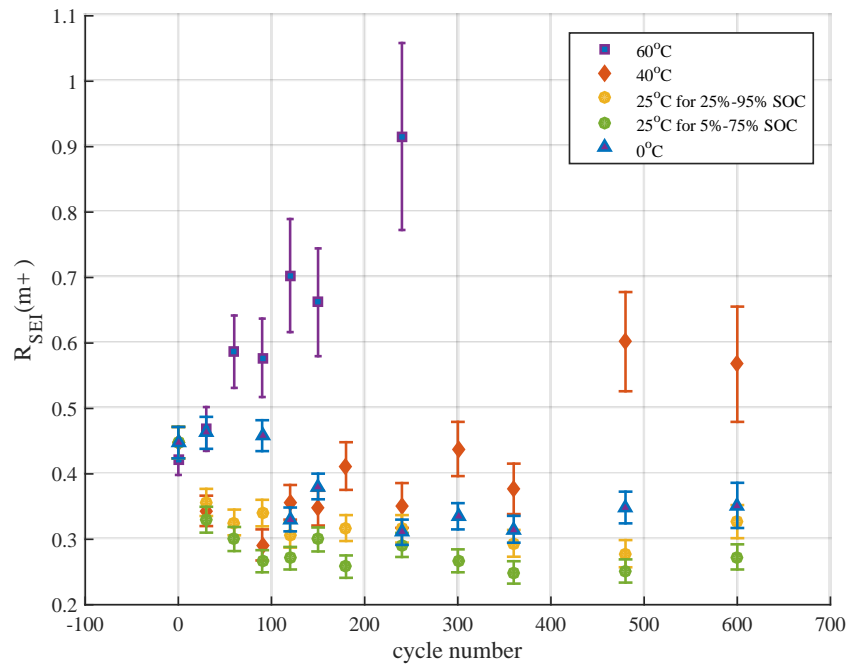


Figure 43: Model fitted parameter - R_{SEI} .

3.4 Determination of temperature dependent parameters

There are two parameters that are temperature dependent in ROM, ion diffusivity in solid electrode particles and the film resistance. The film resistance indicates the contact ohmic resistance between the current collectors and the electrodes. The experimental data and simulated results at 1C discharge from 0°C to 60°C for the beginning of life of a cell are plotted in Figure 44. The solid thin lines are the experimental data while the thick lines with markers are the simulation results obtained from the developed ROM. Both curves show a fairly good match, accomplished by finding appropriate values for the two parameters at different temperatures.

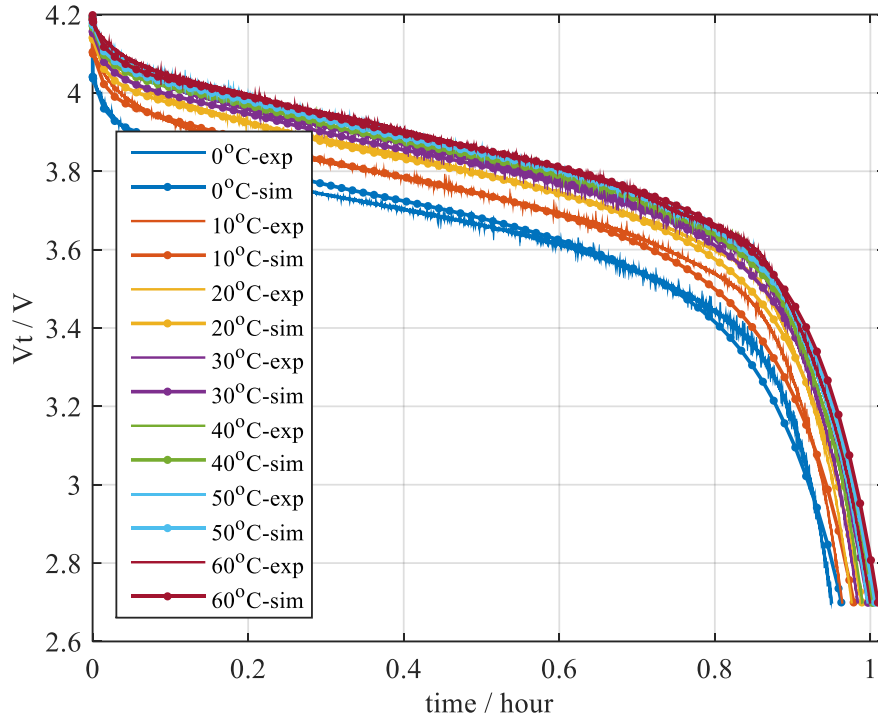


Figure 44: 1C discharge curves at various temperatures.

The diffusion coefficient is expressed using the Arrhenius equation shown in (38), while the correlation of the film resistance and temperature is derived by an exponential empirical equation.

$$D_s = A_s \cdot \exp\left(-\frac{E_{a,s}}{RT}\right) \quad (38)$$

where A_s , $E_{a,s}$, R and T are the pre-factor, the activation energy, the universal gas constant and temperature, respectively.

The dependencies of the diffusion coefficient and film resistance on temperatures are depicted in Figure 45. The markers are the corresponding parameters. The blue line and the green line are the fitted results of the diffusion coefficient and the film resistance, respectively.

The diffusion coefficient increases while the film resistance decreases with the elevated temperature.

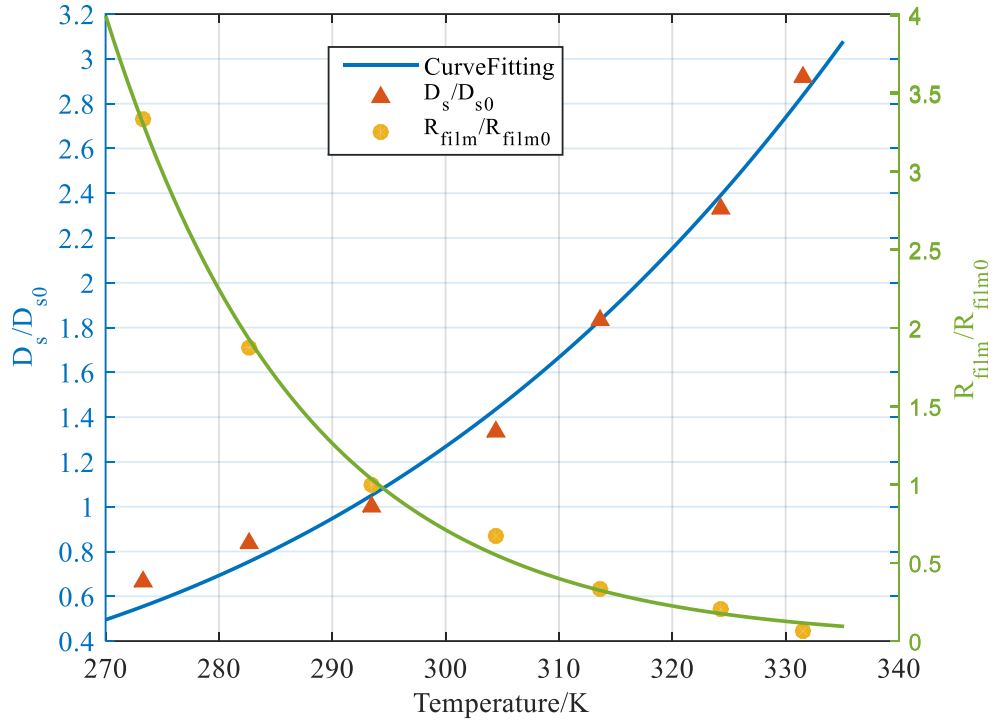


Figure 45: Curve fitting of the diffusion coefficient and film resistance at various temperatures.

Since the SEI layer has high conductivity for lithium ions, but has very low permeability for the EC molecules, the rate of side reaction is predominantly determined by the availability of EC as reactants rather than the abundantly available lithium ions. Therefore, the diffusivity of the EC in the SEI layer that is also dependent upon temperature is particularly crucial for the rate of side reaction. The correlation of the diffusivity and temperature is expressed using the Arrhenius equation (39):

(39)

$$D_{EC} = A_{EC} \cdot \exp\left(-\frac{E_{a,EC}}{RT}\right)$$

where A_{EC} and $E_{a,EC}$ are the pre-factor and the activation energy.

The values of the two coefficients in the equation are determined based on self-discharge characteristics obtained from experimental data. The terminal voltage measured over time at 0°C, 25°C and 40°C, along with the fitting results of the EC diffusivity with respect to temperature are plotted in Figure 46. With elevated temperature, the EC molecules are expected to have higher mobility in the SEI layer. Then the self-discharge that is caused by the internal side reaction without external current input will be more aggressive at a high temperature range, which leads to more voltage drop at a given time. The correlation between the self-discharge voltage change and the EC molecule diffusivity is reflected in Figure 46. It is shown that with the temperature increases, the diffusion coefficient increases as expected.

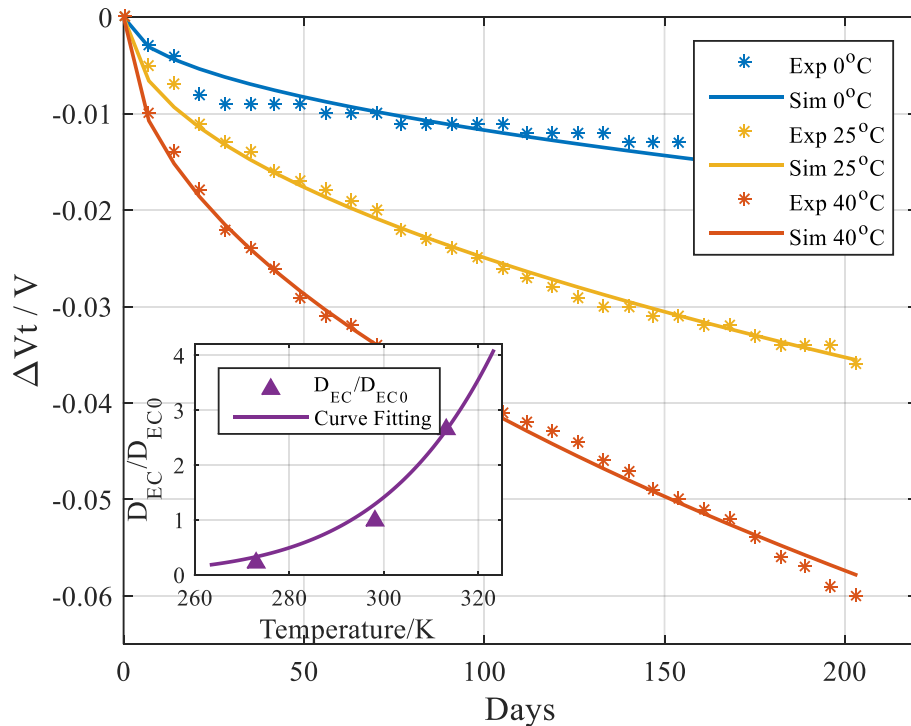


Figure 46: Self-discharge data and fitted EC diffusivity over time.

Chapter 4 Aging model

4.1 Literature review

4.1.1 Review of aging mechanism

Degradation of the performance of batteries is primarily induced by operating conditions and results in the production of byproducts, morphology changes of electrodes and ion diffusivity of the electrolyte.

The major causes and effects of degradation are summarized in Table 5.

Table 5: Summary of degradation mechanisms

Components	Major causes	Effects and consequences	Enhanced by
Graphite particle anode	<ul style="list-style-type: none"> • Side reaction (electrolyte solvent decomposition) • Low temperature operation • Overcharge 	<ul style="list-style-type: none"> • SEI formation <ul style="list-style-type: none"> ○ Loss of lithium ion ○ Loss of active material ○ Increase of impedance • Gas generation and particle cracking • Corrosion of current collector • Self-discharge • Lithium plating <ul style="list-style-type: none"> ○ Loss of lithium ion ○ Loss of electrolyte 	<ul style="list-style-type: none"> • High temperature • High SOC range • Low temperature • High charge rate
Separator (electrolyte)	<ul style="list-style-type: none"> • Side reaction 	<ul style="list-style-type: none"> • SEI formation <ul style="list-style-type: none"> ○ Loss of electrolyte 	<ul style="list-style-type: none"> • High temperature • High SOC range
Metal oxide	<ul style="list-style-type: none"> • Mechanical 	<ul style="list-style-type: none"> • Phase transition and structural 	<ul style="list-style-type: none"> • High temperature

cathode	stress and strain	changes
---------	-------------------	---------

•Cracking and fracture

Among the aging causes, the side reaction taking place at the anode graphite particle surfaces is the most predominant cause of the battery degradation. The main reaction is the process that lithium ions intercalate and de-intercalate on the surface of the electrode particles when cycling. In contrast, the side reaction refers to the electrolyte decomposition reaction that is sustained slowly but constantly throughout the battery life. It is particularly severe during charging process when the anode is polarized and its potential becomes low, which is then stimulated by elevated temperature and high SOC range [31].

The side reaction consumes lithium ions as well as solvents of electrolyte, and produces deposits that form thin unsolvable layers that adhere to the surface of the anode graphite particles. A schematic diagram depicted below in Figure 47 shows the main and side reaction that takes place concurrently at the anode graphite particle surface and the formation of the solid electrolyte interphase (SEI).

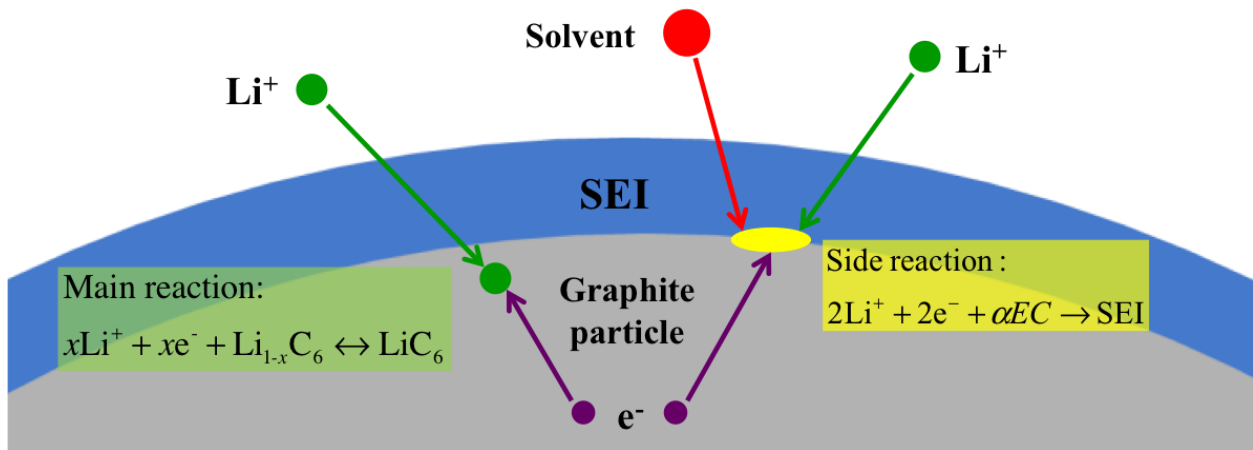


Figure 47: Schematic diagram of the main and side reaction on graphite particles.

Several possible reaction mechanisms and products dependent upon various electrolyte solvent mixtures are reported in the literatures. Since ethylene carbonate (EC) is the organic solvent used for the electrolyte of the investigated batteries, only two predominant side reactions as shown below are considered [31]:



It is shown that the first reaction requires one mole of EC while the second reaction requires two moles to produce one mole of deposit. Accordingly, the major composition of SEI for the EC based lithium ion batteries is a combination of lithium carbonate (Li_2CO_3) and lithium ethylene dicarbonate ($(CH_2OCO_2Li)_2$). The ratio of both compounds is dependent on the concentration of EC in electrolyte [32].

In fact, the SEI layer is ion conductive with low solvent permeability, but nonconductive to electrons. Therefore, the initial formation of SEI serves as a crucial passivation layer that protects the charged negative electrode from corrosion and prevents the electrolyte from further reduction. The initially formed SEI can be regarded as the “good SEI”.

However, the pores present in the SEI layer allow for the electrolyte solvent molecules to diffuse through the existing SEI layer with a small but persistent rate. Finally, the molecules react with lithium ions at the interface between the existing SEI layer and the graphite particle, which leads to the formation of a new deposit that continuously grows, as depicted in Figure 47. The continuously grown SEI layer can be regarded as the “bad SEI”.

Volume changes of the electrode particles during lithium ion intercalation/de-intercalation processes induce cracks in SEI and potentially fractures. Another new SEI layer can be formed at the cracks of the existing SEI [33]. However, this effect is not considered in this paper.

As the deposits caused by side reaction are accumulated with prolonged cycles, the thickness of SEI grows gradually. As a result, the ionic resistance of the SEI increases, which results in power fade. The previous study has shown that a large amount of deposits are particularly produced at the interface between the composite anode and the separator [34], because the side reaction rate near the separator is larger than that inside of the electrode particles. This thick deposit in this area forms a “deposit layer” that has the same composition as those in the SEI layer. The deposits can clog the pores of the particles that decrease the accessible surface of the active material for charges. At the extreme case, some of the particles that fully covered by the deposits become electrically isolated from other particles, so participation in chemical reaction is not possible.

Lithium ions that have been trapped in the isolated particles, along with those consumed in the side reaction, attribute to total ion loss and consequently the capacity fade. Additionally, the irreversible side reaction also consumes electrolyte solvent, which results in the decrease of the electrolyte volume fraction and consequently the ion conductivity in the electrolyte.

The effects of the side reaction are summarized with respect to the reactants versus the products as follows:

Table 6: Summary of side reaction effects

By reactants	By products
--------------	-------------

-
- Loss of lithium ion
 - Loss of electrolyte
 - Decrease of electrolyte volume fraction
 - Decrease of lithium ion diffusivity in electrolyte
 - Growth of SEI thickness and deposit layer
 - Increase of SEI resistance
 - Decrease of ionic conductivity
 - Loss of active material in anode
 - Decrease of electrode volume fraction due to blocking pores
 - Loss of electronic contact due to isolated graphite particles
-

4.1.2 Review of aging modeling

There have been numerous attempts to model degradation phenomenon and predict the lifetime of a battery. The models can be categorized into two groups based on either empirical equation or physical equation. The models in the first group extract the empirical relationship between the aging parameters and the cycling or storage time based on the experimental data. The coefficients of the empirical equations are determined by fitting the simulation curves obtained by a physics-based model that is embedded with the empirical equations to the experimental data. For the first time, a relationship between the consumption of lithium ions and the growth of SEI was proposed under the assumption that loss of lithium ions is proportional to the SEI conductivity [35], which results in a square root function between the SEI thickness and time. This function was further extended to describe the relationship between the capacity and the film resistance with respect to time [36]. Moreover, the active surface area of electrodes, as well as the initial SOC was considered by the curve fittings [37]. Diffusion coefficients were also

added into the group of parameters affected by battery aging [38]. Additionally, control techniques were employed to improve the prediction performance [39].

The models based on empirical equation are straightforward but heavily rely on experiments that are limited in reality. Therefore, these empirical models cannot fully cover all range of operations until the end of life of batteries. Consequently, this approach is time consuming and costly and its performance is relatively vulnerable to changed operating conditions.

Models in the second group are constructed considering the side reaction. The side reaction is described by modified Butler-Volmer (BV) equation that quantifies the reaction rate and facilitates analysis of the aging processes and prediction of the aging parameters. The modified BV equation for the side reaction was firstly introduced to describe the solvent reduction reaction [40]. A proportional relationship between the increasing rate of the SEI thickness and the side reaction rate was proposed. Then, the concentration gradient of EC along the SEI thickness direction is corrected by embedding the mass balance equation of the electrolyte solvent in the SEI layer [41]. Additionally, the correlation between the side reaction rate and the electrode active material volume fraction was derived and used to update the values of the active surface area and the diffusion coefficients [42]. Subsequently, the solvent diffusion model with corrected boundary conditions and BV equation were incorporated into a single particle model [43]. Furthermore, the expression of the EC concentration is simplified and extended to the porous electrode model [44]. Effects of the deposit layer on the ionic conductivity and the change of electrolyte porosity are also considered [45]. Studies have shown that models based on the BV equations are complex but accurate for explicitly describing the side reaction processes with solid physical principles. However, the mass balance of the electrolyte solvent, as well as the relationship between the exchange current density and the solvent concentration, has never been

applied in the porous electrode model. In addition, integration and experimental validation of the degradation phenomenon in a ROM have never been conducted in the literature. Therefore, the aging phenomena and their modeling can be further improved by considering following aspects;

- 1) Integration of the mass balance of electrolyte solvent into the porous electrode model with side reaction rate as the source term in the boundary conditions.
- 2) The exchange current density as a function of lithium ion concentration and the EC concentration on the electrode particle surfaces.
- 3) The diffusion coefficients dependent upon temperature.
- 4) Extensive validations of the aging model against experimental data under various operating conditions.

4.2 Development of aging model

For development of a degradation model, several assumptions have been made:

- The side reaction is irreversible and no overcharge is considered.
- Only the solvent decomposition that takes place at the anode is considered as the source of degradation.
- Electrode volume changes, structure deformations, and graphite particle cracks caused by internal mechanical stress are neglected.
- The composition of SEI is a mixture of Li_2CO_3 and $(\text{CH}_2\text{OCO}_2\text{Li})_2$, which are the products of the side reaction (40) and (41) with the same reaction rate [44].

4.2.1 Modeling of the main reaction and the side reaction

For the previously developed FOM or ROM, the BV equation only describes the charge transfer processes for the main reaction on the electrode graphite particle surfaces. When considering the aging processes, the total reaction rate is a sum of the main and the side reaction, and the overall BV kinetic expression for the anode becomes as follows,

$$j^{Li} = j_{main}^{Li} + j_{side}^{Li} \quad (42)$$

where j^{Li} , j_{main}^{Li} , j_{side}^{Li} denote the total reaction rate, the main reaction rate, and the side reaction rate, respectively.

The main reaction rate is the current density caused by the chemical reaction that takes place at the interface between the electrode graphite particle surfaces and the SEI layer. The corresponding BV equation composed of oxidation and reduction process is expressed as follows:

$$j_{main}^{Li} = a_s i_{0,main} \left(\exp\left(\frac{\alpha_{a,main} \cdot F}{RT} \eta_{main}\right) - \exp\left(-\frac{\alpha_{c,main} \cdot F}{RT} \eta_{main}\right) \right) \quad (43)$$

where a_s is the specific reaction area and $i_{0,main}$ is the exchange current density. $\alpha_{a,main}$ and $\alpha_{c,main}$ are the anodic and cathodic charge transfer coefficient of the main reaction, which is assumed to be a values of 0.5.

Equation (43) can be simplified to a linearized form as we described in 2.3.4 and shown in equation (44):

$$j_{main}^{Li} = a_s i_{0,main} \frac{(\alpha_{a,main} + \alpha_{c,main}) \cdot F}{RT} \eta_{main} \quad (44)$$

By considering the SEI resistance, the activation overpotential of the main reaction η_{main} becomes the following equation (45):

$$h_{main} = j_s - j_e - U_{equi,main} - \frac{R_{SEI}}{a_s} j^{Li} \quad (45)$$

where ϕ_s and ϕ_e are the electrical potential of the solid electrodes and electrolyte, respectively.

R_{SEI} is the ionic resistance of the SEI layer of particles on the anode side. $U_{equi,main}$ is the equilibrium potential of the main reaction, which is a function of the stoichiometry number.

The equilibrium potential of the anode, U_- , is approximated by an empirical equation [45] while the equilibrium potential of the cathode, U_+ , is the sum of U_- and the open circuit voltage (OCV) measured experimentally.

Since the side reaction is irreversible because of high reaction rate of the electrolyte solvent reduction compared to that of the oxidation process, the BV equation for the side reaction can be simplified by only containing the reduction part as shown in equation (46):

$$j_{side}^{Li} = -a_s i_{0,side} \exp\left(-\frac{\alpha_{c,side} n_{side} F}{RT} \eta_{side}\right) \quad (46)$$

where n_{side} is the number of electrons involved in the side reaction and that is equal to two as seen in equation (40) and (41).

The activation overpotential of the side reaction, η_{side} , can be calculated using equation (47):

$$h_{side} = j_s - j_e - U_{equi,side} - \frac{R_{SEI}}{a_s} j^{Li} \quad (47)$$

where $U_{equi,side}$ is the equilibrium potential of the side reaction. The potential varies dependent upon the composition of the electrolyte. References recommend different values such as 2V, 1.7V or 1V, but 0.4V [40][41][42][43] and 0.8V [44][47][48][49] are the most widely used practical values. In this work, the value of $U_{equi,side}$ is iteratively fitted using the terminal voltage obtained by the experimental data.

The exchange current density, $i_{0,side}$, is correlated to the concentrations of two reactants of the side reaction, lithium ions, and EC molecules. Compared to the exchange current density of the main reaction in [49], the side reaction exchange current density, $i_{0,side}$, is expressed as follows:

$$i_{0,side} = k_{side} \sqrt{c_{s,surf} \cdot c_{EC,R_s}} \quad (48)$$

where k_{side} is a kinetic rate constant for the side reaction. $c_{s,surf}$ and c_{EC,R_s} are the concentrations of the lithium ions and the EC molecules at the graphite particle surfaces, respectively.

4.2.2 Modeling of solvent diffusion

The exchange current density of the side reaction is a function of the concentrations of lithium ions and EC molecules on the graphite particle surface. The lithium ion concentration can be calculated from the ROM. In order to obtain the concentration gradient of the EC molecules along the SEI thickness direction, an additional diffusion equation governed by the Fick's law is used. Since the thickness of the SEI is very thin compared to that of the graphite particle radius, the first derivative term of the Fick's equation can be neglected, so the partial differential equation can be simplified as follows (49):

$$\frac{\partial c_{EC}}{\partial t} = D_{EC} \frac{\partial^2 c_{EC}}{\partial r^2} \quad (49)$$

where D_{EC} is the diffusivity of the EC in the SEI layer. r is the coordinate in the particle radial direction.

This equation describes the EC concentration in the SEI from the surface of the graphite particles to the electrolyte bulk. The outer boundary given by $r = R_s + \delta_{SEI}$ is a variable that includes the growth rate of the SEI thickness. The boundary conditions for equation (49) are given as follows:

$$-D_{EC} \left. \frac{\partial c_{EC}}{\partial r} \right|_{r=R_s} = \frac{j_{side}^{Li}}{a_s F} \quad (50)$$

$$c_{EC} \Big|_{r=R_s+\delta_{SEI}} = c_{EC,bulk}$$

where R_s is the radius of the graphite particles. δ_{SEI} is the thickness of the SEI layer. $c_{EC,bulk}$ is the EC concentration in the electrolyte bulk.

The equation (49) that describe the solvent diffusion in the SEI layer is a partial differential equation (PDE), which can be solved numerically by finite difference method in both time and space domain. The corresponding boundary condition shown in equation (50) is a function of both time and space. As the SEI layer grows, the boundary is moving as well, which presents Stefan's problem that is solved by the spatial coordinate transformation method [50].

Since the thickness of the SEI layer is much thinner than the radius of the electrode particles, the spherical coordinate of the SEI layer can be replaced with the Cartesian coordinate. Therefore, the radial direction r is transformed to the thickness direction x and the EC

concentration $c_{EC}(r,t)$ in the radial direction is transformed to $c_{EC}(x,t)$ in the thickness direction as follows.

$$\frac{\partial c_{EC}}{\partial t} = D_{EC} \frac{\partial^2 c_{EC}}{\partial x^2} \quad (51)$$

Since the newly formed SEI is growing between the existing SEI and the graphite particle surface, the origin of the x -axis should be located at the interface of the electrolyte and the SEI layer. The effective range of the EC diffusion equation is transformed from $R_s < r < R_s + d_{SEI}(t)$ to $0 < x < \delta_{SEI}(t)$ and the corresponding boundary conditions are shown in equation (52).

$$-D_{EC} \frac{\partial c_{EC}}{\partial x} \Big|_{x=\delta_{SEI}} = \frac{j_{side}^{Li}}{a_s F} \quad (52)$$

$$c_{EC} \Big|_{x=0} = c_{EC,bulk}$$

The spatial coordinate transformation method is used to modify the space grid. The variable of the spatial coordinate, y is constructed by dividing the original coordinate, x by the SEI thickness δ_{SEI} that is a function of time. EC concentration, $c_{EC}(x,t)$, is transformed equivalently to $\tilde{c}_{EC}(y,t)$ as shown in equation (53).

$$y = \frac{x}{\delta_{SEI}(t)}, \quad \tilde{c}_{EC}(y,t) = c_{EC}(x,t) \quad (53)$$

By substituting equation (53) into equation (51) and (52), the original EC diffusion equation and the corresponding moving boundary conditions are reformulated as follows.

$$\frac{\partial \tilde{c}_{EC}}{\partial t} = \frac{D_{EC}}{\delta_{SEI}^2} \frac{\partial^2 \tilde{c}_{EC}}{\partial y^2} \quad (54)$$

$$-\frac{D_{EC}}{\delta_{SEI}} \frac{\partial \tilde{c}_{EC}}{\partial y} \Big|_{y=1} = \frac{j_{side}^{Li}}{a_s F} \quad (55)$$

$$\tilde{c}_{EC} \Big|_{y=0} = c_{EC,bulk}$$

As a result, the effective range is finally transformed to $0 < y < 1$ and the moving boundary problem is transformed to a fixed boundary problem. The resulting PDE can be solved by Crank-Nicholson implicit method that leads to high accuracy and stability.

Simulation results of the EC concentration gradient along the SEI thickness direction are plotted in Figure 48. The x -axis indicates the radial direction of the anode graphite particles or the thickness direction of the SEI layer. The EC concentration at the outer boundary of the SEI layer is equal to that in the electrolyte bulk, which is assumed to be constant. When the EC molecules slowly diffuse from the electrolyte to the graphite particle surface, the EC concentration in the SEI layer gradually decreases from the electrolyte-SEI interface to the SEI-particle interface. Initially, the EC concentration at the graphite particle surface is nearly zero. With time increased, the EC concentration at that place gradually increases and the thickness of the SEI grows as well.

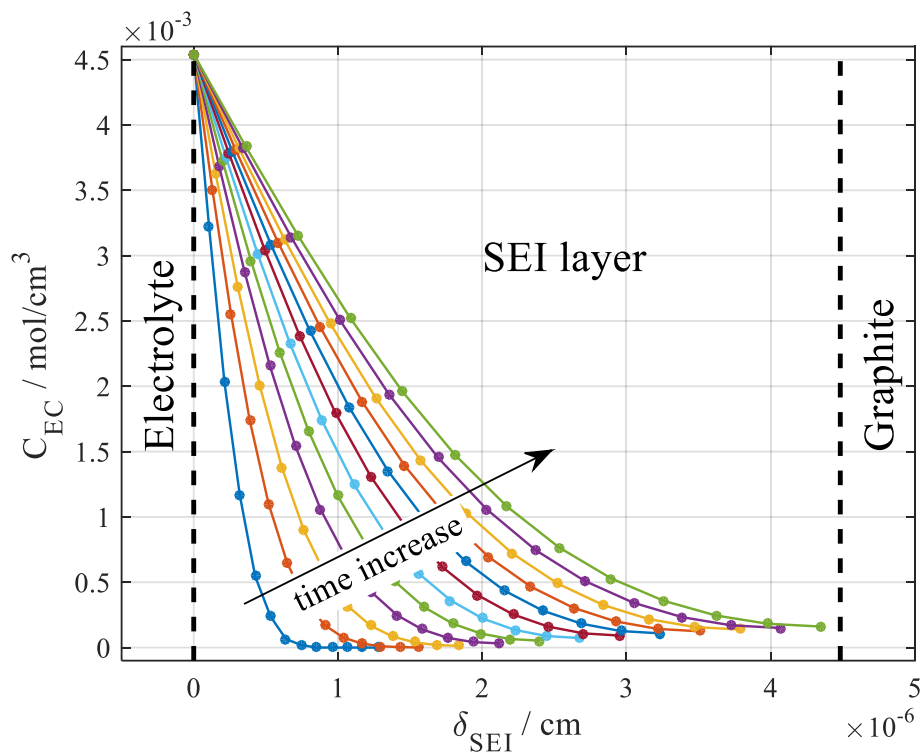


Figure 48: Concentration of EC molecule in the SEI layer.

The EC concentration at the anode graphite particle surface with respect to the SEI thickness is plotted in Figure 49. It is shown that the EC concentration increases with the growth of the SEI thickness when the diffusion time prolonged. However, the slope of the curve decreases over time, which indicates that the EC concentration at the graphite surface tends to be balanced after a certain growth of SEI layer.

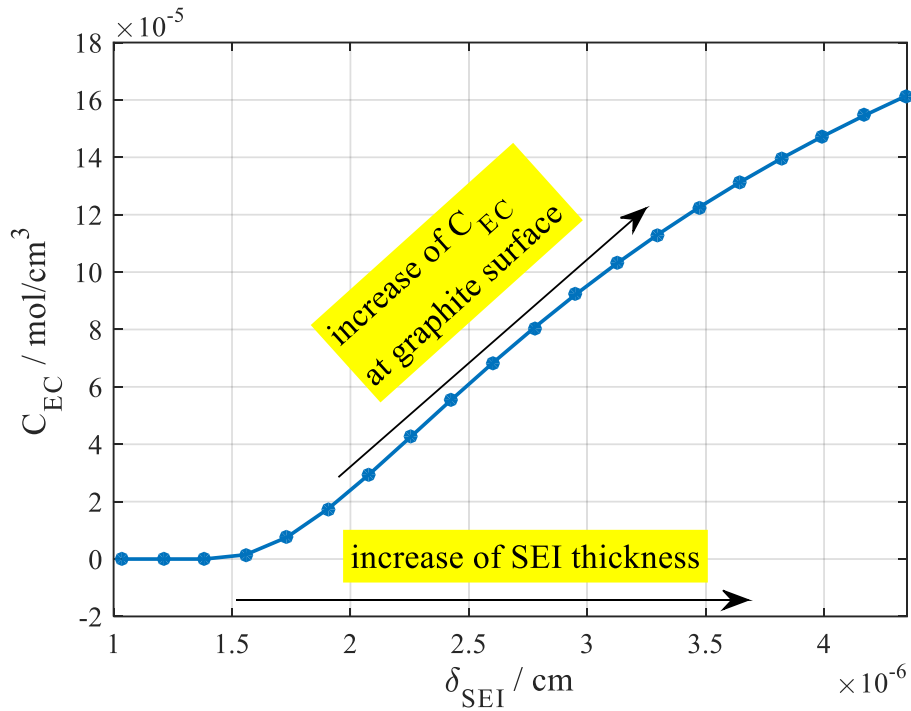


Figure 49: EC concentration at the anode graphite particle surface.

4.2.3 Modeling of side reaction effects

As discussed in the previous sections, the continuous occurrence of the side reaction through the prolonged cycles produces deposits that are accumulated as the ‘bad SEI’. A schematic diagram of the SEI formation in a fresh and aged cell is depicted in Figure 50 using the sandwich microcell model.

The yellow color areas indicate the deposits produced by the side reaction. In the fresh cell, the electrode particles in the composite anode are covered by a thin layer, which represents the "good SEI" that formed at the beginning of battery life. In the aged cell, the yellow area is thicker, which represents the "bad SEI" that accumulated during battery cycling. The one around

the particles are the SEI layer and the one in between the composite anode and the separator is the deposit layer. Some particles are partially or fully covered by the deposits. The partially covered particles still have contact with others, so electrons can flow. Circles marked with “X” represent the fully coated SEI, so particles are fully isolated from the electronic conduction. The other deposit is the layer formed between the composite anode and the separator.

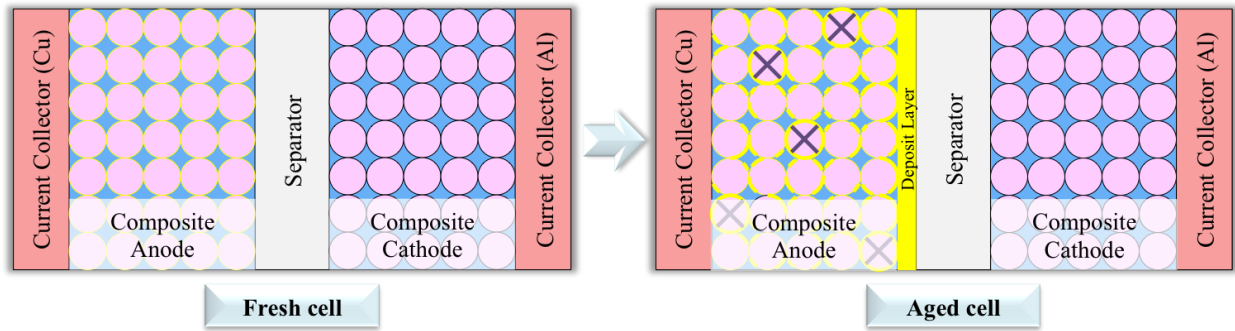


Figure 50: Schematic diagram of the SEI formation in a microcell.

Effects of the side reaction can be analyzed with respect to the reactants and the products. For reactants, the reaction consumes ions and electrolytes. The total amount of consumed ions is obtained by integration of reaction rate over the volume of the composite anode and time, which can be given in equation (56):

$$q_{side}^{Li}(t) = \int_{x=0}^{\delta_-} \left(\int_{\tau=0}^t j_{side}^{Li}(x, \tau) d\tau \right) A dx \quad (56)$$

$q_{side}^{Li}(t)$ is the consumed lithium ions, δ_- is the thickness of the composite anode and A is the cross section area of the battery, respectively.

The decreasing rate of the volume fraction of electrolyte can be obtained by the ratio between volume fractions that is proportional to the integration of the side reaction rate over the thickness of the composite anode as follows:

$$\frac{\partial \varepsilon_e}{\partial t} = -\frac{\alpha \tilde{V}_e}{\delta_- F} \int_{x=0}^{\delta_-} j_{side}^{Li} dx \quad (57)$$

where \tilde{V}_e is the molar volume of the electrolyte. α is the reaction coefficient of the EC that implies the molar ratio of EC over lithium ions in the side reaction.

Since the component of the SEI is a mixture of Li_2CO_3 and $(\text{CH}_2\text{OCO}_2\text{Li})_2$ expressed in equation (40) and (41), α is the coefficient indicating how many moles of electrolyte are consumed when one mole of lithium ion is consumed, which is set to 0.5 for the side reaction in equation (40) and 1 for the side reaction in equation (41). Under the assumption that both side reactions have the same reaction rate, an averaged value of 0.75 is used.

Correspondingly, the effective diffusivity of the lithium ions in the electrolyte can be expressed by considering the change of electrolyte porosity.

$$D_e^{\text{eff}} = D_e \cdot \varepsilon_e \quad (58)$$

On the other hand, the products of the side reaction increase the thickness of the SEI layer and form a new deposit layer close to the separator on the anode composite electrode, whose rates can be described as in equation (59) and (60):

$$\frac{\partial \delta_{SEI}}{\partial t} = -\frac{\tilde{V}_{SEI}}{2\alpha_s F} j_{side}^{Li} \quad (59)$$

$$\frac{\partial \delta_{DL}}{\partial t} = -\frac{R_s \tilde{V}_{DL}}{2F} j_{side, x=\delta_-}^{Li} \quad (60)$$

where \tilde{V}_{SEI} and \tilde{V}_{DL} are the molar volumes of the SEI layer and the deposit layer respectively.

As results, the increasing rate of SEI and deposit layer resistance can be expressed as in equation (61) and (62):

$$\Delta R_{SEI} = \delta_{SEI} / \kappa_{SEI} \quad (61)$$

$$\Delta R_{DL} = \delta_{DL} / \kappa_{DL} \quad (62)$$

where κ_{SEI} and κ_{DL} are the ionic conductivity of the SEI and the deposit layer, respectively.

When the deposits clog the pores of the graphite particles, active material volume fraction decreases as follows:

$$\Delta \varepsilon_s = -k_s a_s \delta_{SEI} \quad (63)$$

where k_s is a dimensionless coefficient.

The effects of the side reaction are summarized in Table 7:

Table 7: Effects of the side reaction.

Side reaction	Effects on reactants and products	Effects on model parameters
Side reaction rate: $ j_{side}^{Li} \uparrow$	Loss of lithium ion: $q_{side}^{Li}(t) \uparrow$	Capacity: $Q_{max} \downarrow$
	Loss of electrolyte: $\varepsilon_e \downarrow$	Electrolyte volume fraction: $\varepsilon_e \downarrow$
		Effective diffusivity: $D_e^{eff} \downarrow$
	SEI thickness: $\delta_{SEI} \uparrow$	SEI resistance and volume fraction: $R_{SEI} \uparrow$ and $\varepsilon_{SEI} \uparrow$
		Active material volume fraction: $\varepsilon_s \downarrow$
	Deposit layer thickness: $\delta_{DL} \uparrow$	Ionic conductivity: $R_{DL} \uparrow$

4.3 Simulation analysis at 25°C

4.3.1 Analysis of side reaction rate

In order to analyze the changes of the aging related parameters inside of the battery over time, simulation results of the side reaction rate and the corresponding parameters are presented at 25°C. The rate of side reaction at each grid points along the anode thickness direction and how the value changes with the increased cycle number are plotted in Figure 51. The x -axis is the non-dimensional thickness of the anode. The interface between the current collector and the anode is located at $x=0$ while the interface between the anode and the separator is located at $x=1$. By examining each line along the x -direction, it turns out that the side reaction rate is larger near the separator side, which accelerates the formation of the deposit layer in that area. With the cycle number increased, the side reaction is accumulated in the composite anode as the arrow indicating direction in the figure.

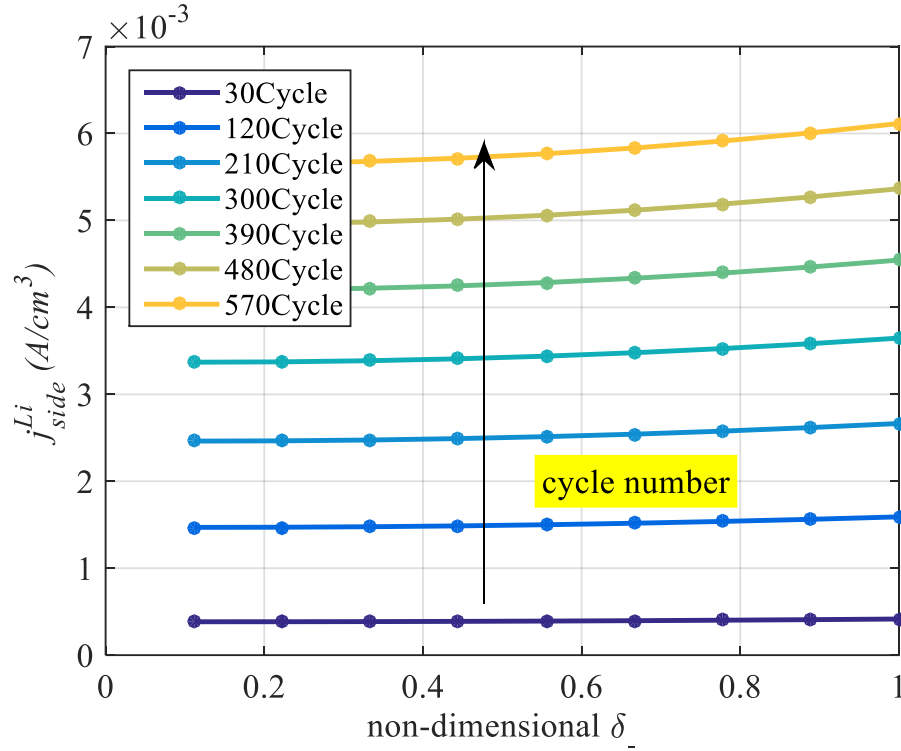


Figure 51: Accumulated side reaction rate along the anode thickness direction.

4.3.2 Analysis of aging parameters

Correspondingly, the variation of the physical parameters discussed in the previous section 4.2.3 are presented in Figure 52 and Figure 53, where the change of electrode volume fraction and SEI resistance at different grid points in anode and the change of electrolyte volume fraction and deposit layer resistance over different cycle numbers are plotted in Figure 52 and Figure 53, respectively. With the cycle number increased, the products of the side reaction is accumulated on the graphite particle surface, particularly near the separator because of higher side reaction rate caused by high ion concentration. Consequently, the SEI resistance, R_{SEI} , as well as the deposit layer resistance, R_{DL} , increases over time. Accordingly, the electrode volume fraction,

ϵ_s , becomes less because of the isolation of the active material caused by the grown SEI layers, which is described by equation (63). Similarly, the electrolyte volume fraction, ϵ_E , becomes less because of the side reaction that consumes the electrolyte.

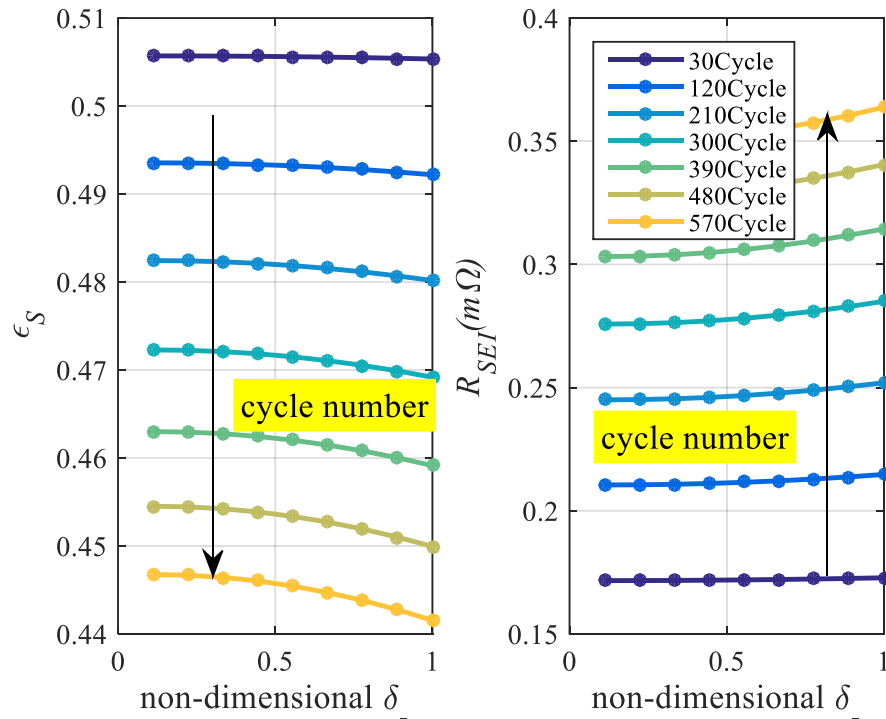


Figure 52: Change of electrode volume fraction and SEI resistance along the anode thickness direction.

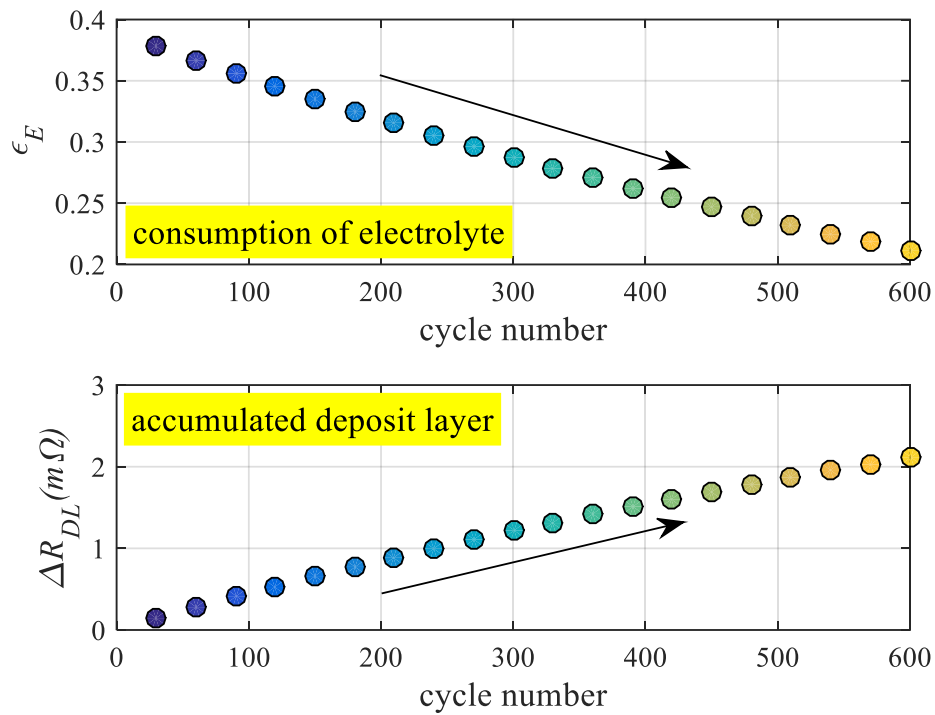


Figure 53: Change of electrolyte volume fraction and deposit layer resistance with increasing cycle number.

4.4 Experimental validation at different temperatures

The effects of SOC range and charging C-rate on degradation have been discussed in [44]. The degradation is accelerated at high SOC range and charging C-rate has no clear effect on degradation. However, temperature has the predominant effects on accelerating the cell degradation process. Therefore, the behavior of the aged cells at different temperatures is investigated in more details.

4.4.1 Validation of SEI resistance

The experimental data includes SEI resistances extracted from EIS, and 0.2C discharge characteristics and cell capacity at different cycle numbers are compared with the simulated data. The changes of SEI resistance with the increase of cycle number at 0°C, 25°C and 40°C are plotted in Figure 54. The experimental data collected by EIS and the simulation results from the aging model are plotted separately in the lower two subplots while the comparison that integrated both the experimental data and the simulation results is shown in the upper subplot. The black markers connected by dash lines are simulation results, which tends to follow the experimental data with some deviations. Generally, the SEI resistance increases with the growth of cycle numbers, especially at high temperature. Increasing of SEI resistance induced by the accumulated side reaction products cause power fade of the batteries.

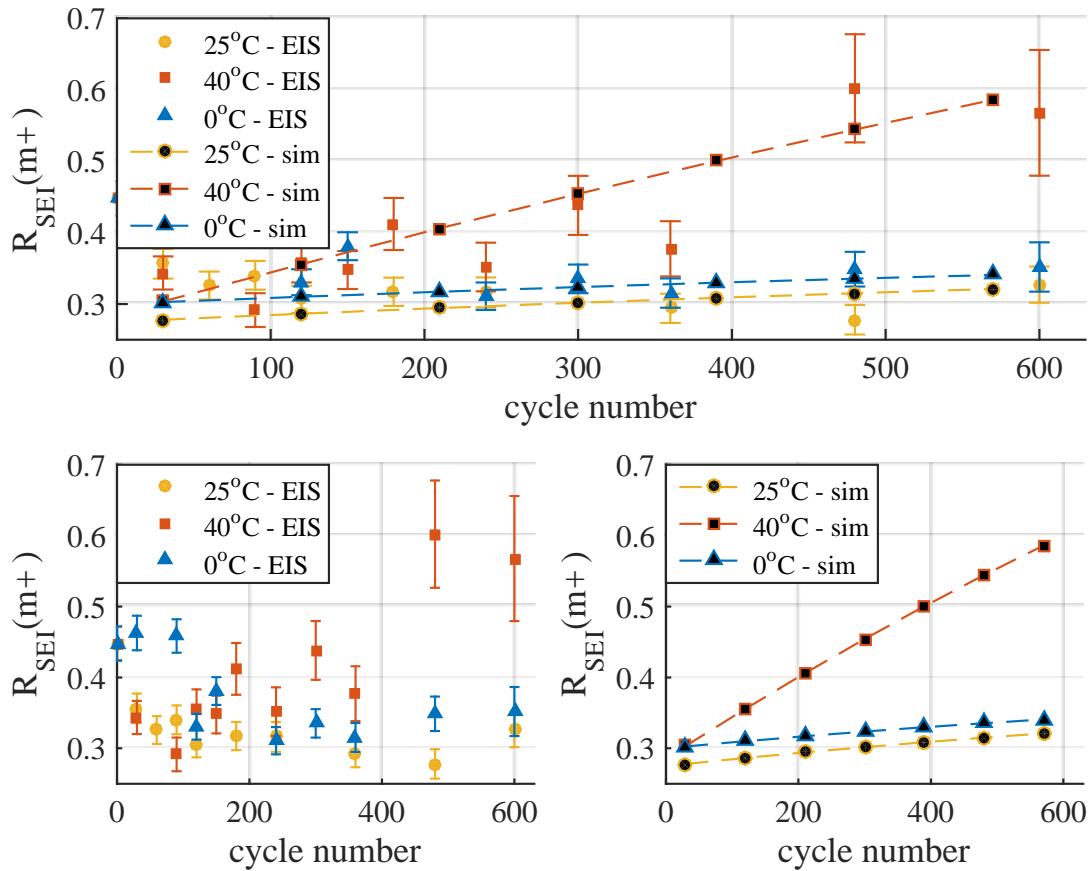


Figure 54: Change of SEI resistance with increasing cycle number.

4.4.2 Validation of discharge characteristics

The discharge characteristics of the degraded cells with 0.2C discharge current at 0°C, 25°C and 40°C are shown in Figure 55 and Figure 56. The solid thin lines are the experimental data at 30, 300 and 600 cycles and the thick lines with markers are the simulation results for up to 1500 cycles. As the number of cycles increases, the terminal voltage decreases and the discharge time becomes shorter due to capacity fade. The simulated terminal voltage tends to follow the experimental data for the beginning and middle of the cycling at 25°C and 40°C while the

discrepancy occurs at 0°C, which is caused by large ohmic overpotential at low temperature. At the end of the cycling, the simulated voltage matches pretty well with the experimental data for 30, 300 cycles. However, there are some deviations at 600 cycles that are caused by inaccurate estimation of capacity.

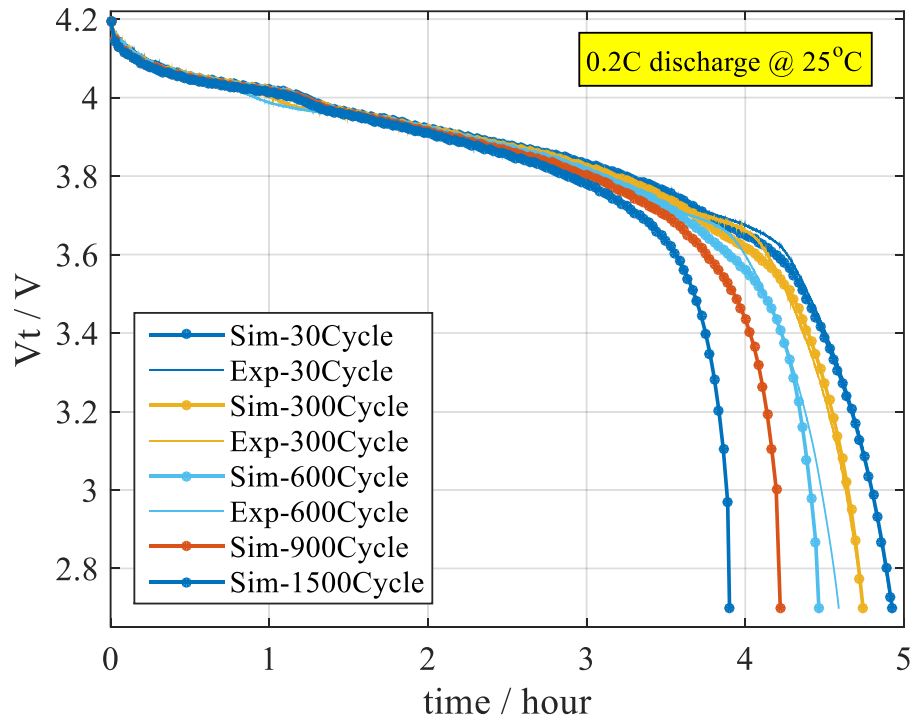


Figure 55: Discharge characteristics of the degraded cell at different number of cycles at 25°C.

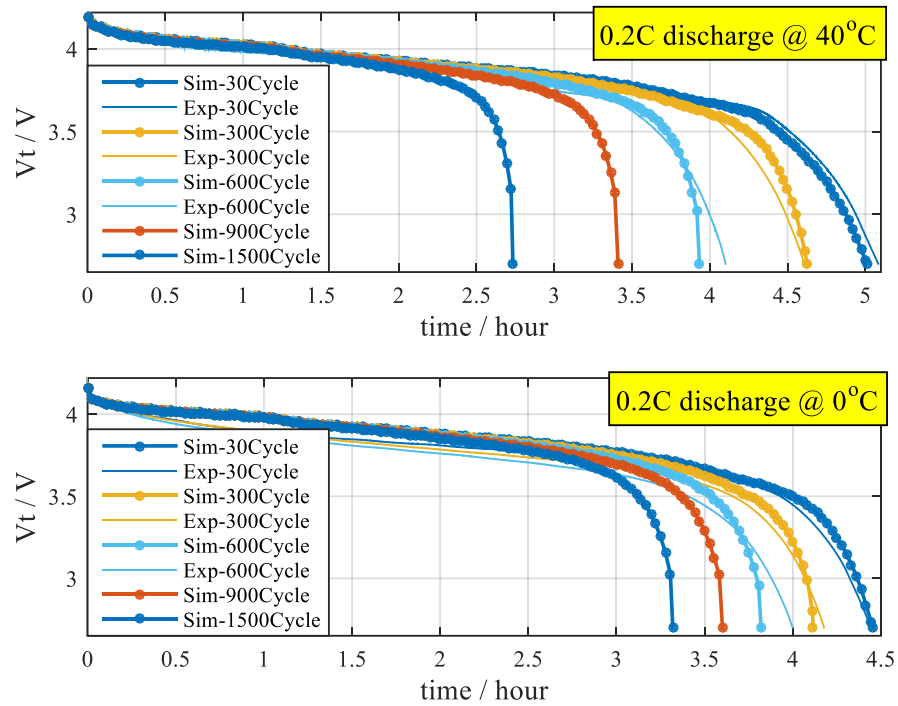


Figure 56: Discharge characteristics of the degraded cell at different number of cycles at 40°C and 0°C.

4.4.3 Validation of capacity

In order to compare the performance of the model with respect to capacity fade, the capacity is measured at discharging with 0.2C rate for every 30 cycles at 0°C, 25°C, and 40°C. For better analysis, a relative capacity is introduced and defined as the percentage of the aged cell capacity over the fresh cell capacity. The relative capacity between the simulated and experimental data is compared up to 600 cycles in Figure 57 and then predicted up to 1500 cycles at different temperatures.

More severe degradation is observed and estimated at higher and lower ambient temperatures compared to the room temperature operation, which is shown as the capacity of the cell at 0°C and 40°C decreases faster than the cell at 25°C. At higher temperature range, EC molecules and lithium ions have better mobility, which results in intense chemical reaction and diffusion not only for the main reaction but also for the side reaction. Hence, the degradation that caused by the side reaction is more aggressive at elevated temperature range. At lower temperature range, the battery internal ohmic resistance is larger than that at high temperature. Consequently, more heat is generated inside of the battery during cycling though the ambient temperature is low, which also leads to more degradation. The simulation results tend to follow the experimental data as shown in Figure 57, where the capacity fade at 900 and 1500 cycles are predicted. The error percentage of the relative capacity estimation is calculated by equation (64) and depicted in Figure 58, which shows that the deviation of the simulation results from the experimental data is less than 5%.

$$error = \frac{Q_{rel,sim} - Q_{rel,exp}}{Q_{rel,exp}} \cdot 100\% \quad (64)$$

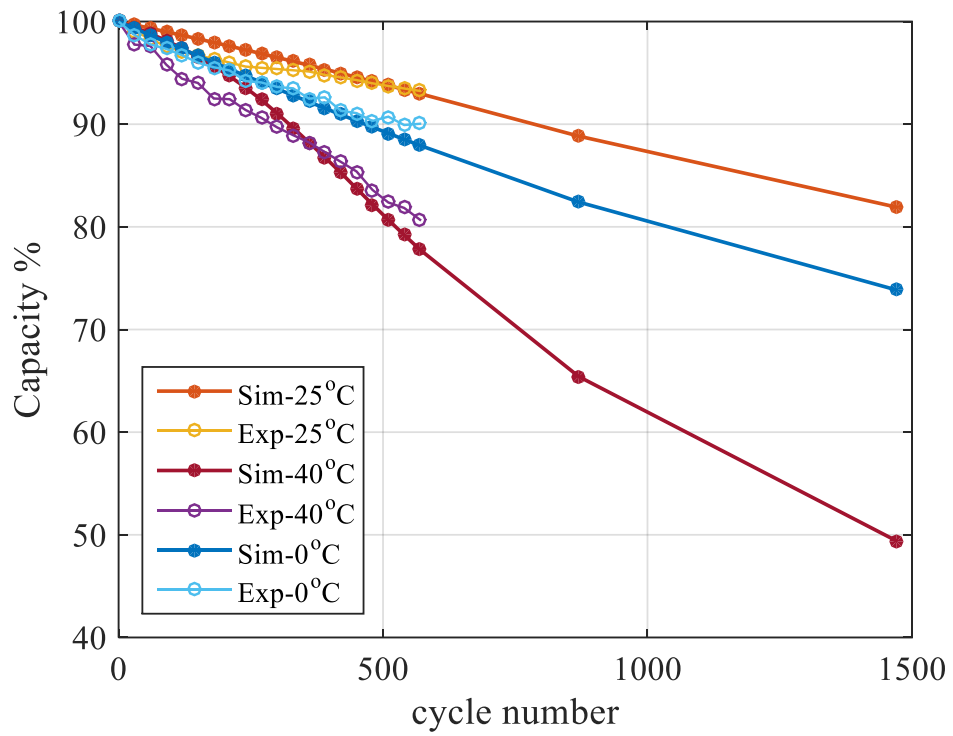


Figure 57: Relative capacity at different temperatures.

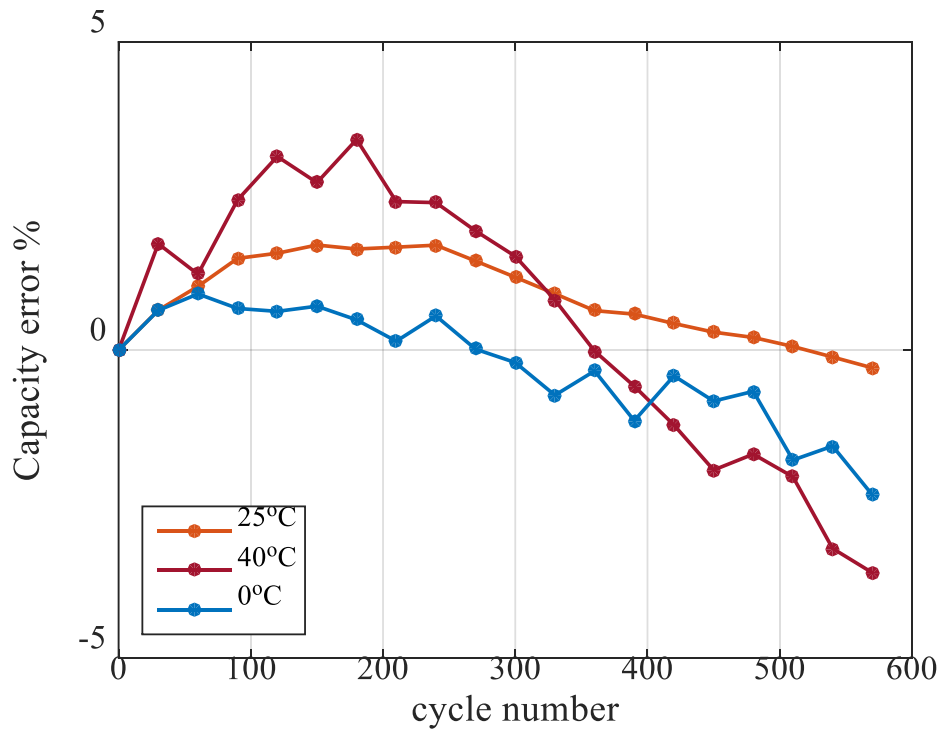


Figure 58: Error of the relative capacity estimation at different temperatures.

4.5 Summary of aging model

Review of papers and experimental studies have revealed that the side reaction is the main cause for performance degradation of the lithium ion battery. The side reaction is mathematically described by modifying the Butler-Volmer equation and the corresponding degradation processes are modeled based on physical principles. The degradation model is incorporated into the previously developed ROM. The integrated model is then validated against experimental data obtained from a large format pouch type of Li[MnNiCo]O₂/Graphite cells.

Main accomplishments and findings are summarized as follows:

- Improvement of the porous electrode model by adding the mass balance of electrolyte solvent,
- Modification of the exchange current density as a function of lithium ion concentration and the EC concentration on the electrode particle surfaces,
- Temperature dependence of the diffusion coefficients of the lithium ion in electrode particles and the EC molecules in electrolyte,
- Analysis of parameter sensitivities at 25°C
- Incorporation the aging model in the ROM and its experimental validation at different temperatures that include SEI resistance from EIS measurements, discharge characteristics and relative capacity from the cycling data,

- Cycling at elevated temperature and low temperature has significantly accelerated the degradation process. More severe capacity fade is found in high temperature range,
- The error of prediction of capacity fade is less than 5 % up to 600 cycles.

Chapter 5 Conclusion

This work has focused on the development of a highly efficient reduced order model considering aging effects for a high power pouch type cell based on electrochemical thermal principles. I began the research by the development of a ROM based on a previously developed full order electrochemical model. Three different model order reduction techniques are introduced to simplify the computational complexity of the individual part of the FOM. The responses of the sub-models are analyzed by comparing the simulation results to the FDM results. Then the sub-models are integrated to a complete ROM that is validated against experimental data at various operating conditions. In addition, the effects of different sampling rates on computational time and accuracy are analyzed. The performance of the ROM has shown promising results with respect to static and dynamic responses of the terminal voltage at the tests conveyed over a single cycle and multiple cycles.

In order to develop a physic based aging model, intensive experimental investigations have been conducted at various operating conditions to better understand aging mechanisms. Fresh cells are continuously cycled with a constant current of 4 C rate, followed by 0.2C to measure the capacity for every 30 cycles at 0°C to 60°C. Impedance characteristics are measured by EIS and its parameters for EIS-ECM are obtained by curve fitting procedure at 25°C. The cycling data and EIS analysis have shown that the elevated temperature has the major factor on accelerating the degradation process. Then, two temperature dependent parameters are extracted from experimental data and fitted to a function of temperature.

Based on the knowledge of aging processes, a physics based aging model is developed and integrated into the ROM developed before. Since the side reaction at the anode side, which is also denoted as the electrolyte solvent reduction reaction, is the predominant factor causing cell degradation, the Butler-Volmer equation is separated to a main reaction and a side reaction part. Due to the low permeability of the SEI for the EC molecules that is one of the reactants of the side reaction, the concentration of EC molecules has a large impact on cell degradation process. Therefore, the EC diffusion in SEI is modeled by Fick's law and the side reaction exchange current density is formulated as a function of EC concentration. The integrated model is then validated against experimental data collected at different C rates and temperatures.

The key findings of this work are summarized below:

- Development of a reduced order model
 - Comparative analysis of the performances of the individual reduced sub-models in time and frequency domain.
 - Selection of sampling time based on errors.
 - Performance of the developed ROM
 - Reduction of computational time to one-tenth of the previous ROM while the accuracy remains the same or better than the previous ROM regardless of the sampling time.
 - The order is adjustable dependent upon input profiles or accuracy requirements.

- Experimental investigation of aging mechanisms

- Operating temperature has a great impact on cell degradation. Reactants of the side reaction have better mobility in high temperature, which leads to excessive accumulation of side reaction products and consumption of lithium ions and electrolyte. Cell internal resistance is larger at low temperature, which results in more power fade.
 - Cycling at high SOC accelerates degradation process but the effect is minor compared to high temperature.
- Development of an aging model
 - Improvement of the porous electrode model by adding the mass balance of electrolyte solvent,
 - Modification of the exchange current density as a function of lithium ion concentration and the EC concentration on the electrode particle surfaces,
 - Temperature dependence of the diffusion coefficients of the lithium ion in electrode particles and the EC molecules in electrolyte,
 - Analysis of parameter sensitivities at 25°C
 - Incorporation the aging model in the ROM and its experimental validation at different temperatures that include SEI resistance from EIS measurements, discharge characteristics and relative capacity from the cycling data,
 - Cycling at elevated temperature and low temperature has significantly accelerated the degradation process. More severe capacity fade is found in high temperature range,
 - The error of prediction of capacity fade is less than 5 % up to 600 cycles.

In order to accurately and quickly represent behavior of a battery using electrochemical thermal model, parameter values of physical properties such as particle sizes, electrochemical reaction rate constants, diffusivity, conductivity, are required to be predicted accurately not only in the battery beginning of life (BOL) but also in the middle and end of life (EOL). However, most of the electrochemical parameters are hard to characterize using simple experimental methods. As one of the most important issues for practical applications, this barrier can be potentially overcome by applying parameter identification with further model order reductions. Unknown entire or partial parameters for a model can be estimated using the BOL model and then continuously updated by fitting to the experimental data. A nonlinear least squares regression technique such as the Newton's method and the genetic algorithm can be applied to minimize the estimation errors. Therefore, future work should include the development of identification algorithm for the full set model parameters through the entire life, which can be accomplished by further simplification of ROM, experimental preparation for model validation and development of the mathematical algorithm.

Appendix

Table 8: Parameters of the ROM [45].

Category	Parameter	Negative electrode	Separator	Positive electrode	unit
Geometry and volume fractions	Thickness, δ	52×10^{-4}	30×10^{-4}	62×10^{-4}	cm
	Particle radius, R_s	0.85×10^{-4}		0.85×10^{-4}	cm
	Active material volume fraction, ε_s	0.51		0.51	
	Polymer phase volume fraction, ε_p	0.048	0.5	0.11	
	Conductive filler volume fraction, ε_f	0.04		0.06	
	Porosity, ε_e	0.39	0.5	0.39	
Li^+ concentrations	Stoichiometry at 0% SOC: $x_{0\%}, y_{0\%}$	0.2004		0.996	
	Stoichiometry at 100% SOC: $x_{100\%}, y_{100\%}$	0.8885		0.3115	
	Average electrolyte concentration, c_e	1.2×10^{-3}	1.2×10^{-3}	1.2×10^{-3}	mol cm^{-3}
	Exchange current density coefficient, k_{i0}	13.2		6.79	A cm^{-2}
Kinetic and	Charge-transfer coefficient, α_a, α_c	0.5, 0.5		0.5, 0.5	

transport properties	Solid phase diffusion coefficient, D_s	0.67×10^{-12}	7.4×10^{-12}	$\text{cm}^2 \text{ s}^{-1}$	
	Solid phase conductivity, σ	1	0.01	S cm^{-1}	
	Electrolyte phase Li^+ diffusion coefficient, D_e	3×10^{-6}	3×10^{-6}	3×10^{-6}	$\text{cm}^2 \text{ s}^{-1}$
	Bruggeman's porosity exponent, p	1.5	1.5	1.5	
	Electrolyte phase ionic conductivity, κ	$15.8c_e$	$15.8c_e$	$15.8c_e$	S cm^{-1}
		$\exp(-13472c_e^{1.4})$	$\exp(-13472c_e^{1.4})$		
	Li^+ transference number, t_+^0	0.363	0.363	0.363	

Table 9: Parameters of the degradation model.

Parameter	Value	Source
EC diffusion coefficient D_{EC} ($\text{cm}^2 \text{ s}^{-1}$)	1.5×10^{-21} at 0°C 6.8×10^{-21} at 25°C 18×10^{-21} at 40°C	Optimized by comparing simulation to the self-discharge data
equilibrium potential of side reactions, $U_{\text{eq, side}}$ (V)	0.4	Optimized by comparing simulation to the experimental data
molar volume of SEI, \tilde{V}_{SEI} (cm^3/mol)	2	Obtained by assuming the initial thickness of SEI is 2 nm

ionic conductivity of SEI, κ_{SEI} (S cm ⁻¹)	2.5×10^{-8}	Optimized by comparing simulation to the SEI resistance obtained from EIS
isolation rate of active anode materials due to SEI, k_{iso}	45.7	Optimized by comparing simulation to measured capacity fade
molar volume of DL, \tilde{V}_{DL} (cm ³ /mol)	7560	Obtained from literature [44]
ionic conductivity of DL, κ_{DL} (S cm ⁻¹)	1×10^{-3}	Optimized by comparing simulation to the terminal voltage under cycling
molar volume of electrolyte, \tilde{V}_e (cm ³ /mol)	252	Optimized by comparing simulation to the terminal voltage under cycling

References

- [1] M. Rosa Palacin, *Chemical Society Reviews*, 38.9 (2009), pp. 2565-2575.
- [2] J. Ying, C. Jiang, C. Wan, *J. Power Sources*, 129 (2004), pp. 264-269.
- [3] R. Marom, et al., *J. Mater. Chem.*, 21 (2011), pp.9938-9954.
- [4] J.Y. Song, Y.Y. Wang, C.C. Wan, *J. Power Sources*, 77(1999), pp183-197.
- [5] L. Gao, S. Liu, RA. Dougal, *IEEE Trans. Components Packaging. Technol.*, 25(3) (2002), pp. 495-505.
- [6] M. Doyle, T. Fuller, J. Newman, *J. Electrochemical Soc.*, 140 (1993), pp. 1526-1533.T.
- [7] Fuller, M. Doyle, J. Newman, *J. Electrochemical Soc.*, 141 (1994), pp. 1-10.
- [8] M. Doyle, T. Fuller, J. Newman, *Electrochimica Acta*, 39 (1994), pp. 2073-2081.S.
- [9] Stewart, J. Newman, *J. Electrochemical Soc.*, 155 (2008), pp. A458-A463.
- [10] S. Steward, J. Newman, *J. Electrochemical Soc.*, 155 (2008), pp. F13-F16.
- [11] G. Nagarajan, J. Zee, *J. Electrochemical Soc.*, 145 (1998), pp. 771-779.
- [12] KA. Smith, CD. Rahn, CY. Wang, *Energy Conversion & Management*, 48(9) (2007), pp. 2565-2578.
- [13] M. Xiao, S.Y. Choe, *J. Power Sources*, 218 (2012), pp. 357-367.
- [14] KA. Smith, CD. Rahn, CY. Wang, *J. Dyn. Sys., Meas., Control* 130(1) (2008), pp. 011012-1-8.
- [15] L. Cai, RE. White, *J. Electrochemical Soc.*, 156(3) (2009), pp. A154-A161.
- [16] S. Santhanagopalan, R.E. White, *J Power Sources*, 161 (2006), pp. 1346-1355.

- [17] CY. Wang, WB. Gu, BY. Liaw, J. Electrochemical Soc., 145(10) (1998), pp. 3407-3417.
- [18] VR. Subramanian, VD. Diwakar, D Tapriyal, J. Electrochemical Soc., 152(10) (2005), pp. A2002-A2008.
- [19] S. Liu, Solid State Ionics, 177(1) (2006), pp. 53-58.
- [20] V. Ramadesigan, V. Boovaragavan, J.C. Pirkle Jr., V.R. Subramanian, J. Electrochemical Soc., 157(7) (2010), pp. A854-A860.
- [21] TS. Dao, CP. Vyasarayani, J. McPhee, J. Power Sources, 198 (2012), pp. 329-337.
- [22] T. Jacobsen, K. West, Electrochimica Acta, 40(2) (1995), pp. 255-262.
- [23] JC. Forman, S. Bashash, JL. Stein, HK. Fathy, J. Electrochemical Soc., 158(2) (2011), pp. A93-A101.
- [24] X. Li, M. Xiao, S.Y. Choe, Electrochimica Acta, 97 (2013), pp. 66-78.
- [25] R. Bouchet, S. Lascaud, M. Rosso, J. Electrochemical Soc., 150 (2003), pp. A1385-A1389.
- [26] P. Moss, G. Au, E. Plichta, J. Zheng, J. Electrochemical Soc., 157 (2010), pp. A1-A7.
- [27] G. Ning, B. Haran, B. Popov, J. Power Sources 117 (2003), pp. 160-169.
- [28] B. Ratnakumar, M. Smart, S. Surampudi, Battery Conference on Applications and Advances, The Seventeenth Annual, (2002), pp. 53-58.
- [29] S.S. Zhang, K. Xu, T.R. Jow, Electrochimica Acta, 51 (2006), pp. 1636-1640
- [30] Y. Zhao, S.Y. Choe, SAE Technical Paper, 2014-01-1835, (2014).

- [31] J. Vetter, P. Novak, M. Wagner, C. Veit, K. Moller, J. Besenhard, M. Winter, M. Wohlfahrt-Mehrens, C. Vogler, A. Hammouche, *J. Power Sources* 147 (2005), pp. 269-281.
- [32] D. Aurbach, M. Levi, E. Levi, A. Schechter, *J. Phys. Chem. B*, 101 (1997), pp. 2195-2206.
- [33] D. Aurbach, *J. Power Sources* 89 (2000), pp. 206-218.
- [34] R. Fu, S. Y. Choe, V. Agubra, J. Fergus, *J. Power Sources* 261 (2014), pp. 120-135.
- [35] M. Broussely, S. Herreyre, P. Biensan, P. Kasaztejna, K. Nechev, R. Staniewicz, *J. Power Sources* 97-98 (2001), pp. 13-21.
- [36] P. Ramadass, B. Haran, R. White, B. Popov, *J. Power Sources* 123 (2003), pp. 230-240.
- [37] S. Santhanagopalan, Q. Zhang, K. Kumaresan, R. White, *J. Electrochemical Soc.*, 155 (2008), pp. A345-A353.
- [38] V. Ramadesigan, K. Chen, N. Burns, V. Boovaragavan, R. Braatz, V. Subramanian, *J. Electrochemical Soc.*, 158 (2011), pp. A1048-A1054.
- [39] G. Prasad, C. Rahn, *J. Power Sources* 232 (2013), pp. 79-85.
- [40] P. Ramadass, B. Haran, P. Gomadam, R. White, B. Popov, *J. Electrochemical Soc.*, 151 (2004), pp. A196-A203.
- [41] H. Ploehn, P. Ramadass, R. White, *J. Electrochemical Soc.*, 151 (2004), pp. A456-A462.
- [42] G. Sikha, B. Popov, R. White, *J. Electrochemical Soc.*, 151 (2004), pp. A1104-A1114.

- [43] M. Safari, M. Morcrette, A. Teyssot, C. Delacourt, *J. Electrochemical Soc.*, 156(2009), pp. A145-A153.
- [44] M. Pinson, M. Bazant, *J. Electrochemical Soc.*, 160 (2013), pp. A243-A250.
- [45] R. Fu, S. Y. Choe, V. Agubra, J. Fergus, *J. Power Sources* 278 (2015), pp. 506-521.
- [46] Y. Zhao, S. Y. Choe, *J. Electrochimica Acta*, 164(2015), pp. 97-107.
- [47] K. Edströma, M. Herstedt, D. Abraham, *J. Power Sources* 153 (2006), pp. 380-384.
- [48] H. Bryngelsson, M. Stjerndahl, T. Gustafsson, K. Edström, *J. Power Sources* 174 (2007), pp. 970-975.
- [49] P. Verma, P. Maire, P. Novák, *J. Electrochimica Acta*, 55 (2010), pp. 6332-6341.
- [50] M. Doyle, T. Fuller, J. Newman, *J. Electrochemical Soc.*, 140 (1993), pp. 1526-1533.
- [51] J. Yao, W. Liu, Z. Chen, *Mathematical Problem in Engineering*, 2013.